

# Drivers of marine heatwaves in the East China Sea and the South Yellow Sea in three consecutive summers during 2016-2018

Guan-dong Gao<sup>1</sup>, Maxime Marin<sup>2</sup>, Ming Feng<sup>3</sup>, Bao-shu Yin<sup>1</sup>, Dezhou Yang<sup>1</sup>, Xingru Feng<sup>1</sup>, Yang Ding<sup>4</sup>, and Dehai Song<sup>5</sup>

<sup>1</sup>Institute of Oceanology, Chinese Academy of Sciences

<sup>2</sup>CSIRO

<sup>3</sup>CSIRO Oceans and Atmosphere

<sup>4</sup>Physical Oceanography Laboratory/CIMST, Ocean University of China and Qingdao National Laboratory for Marine Science and Technology

<sup>5</sup>Key Laboratory of Physical Oceanography, Ministry of Education, China

November 24, 2022

## Abstract

In three consecutive years from 2016 to 2018, extreme ocean warming events, or marine heatwaves (MHW), occurred during boreal summers in the East China Sea (ECS) and South Yellow Sea (SYS), which is unprecedented in the past four decades based on the satellite record. In this study, we used a high-resolution hydrodynamic model based on FVCOM (Finite Volume Community Ocean Model) to simulate the evolution of these warming events. An upper ocean temperature budget (0-20m) analysis based on the model results shows that the shortwave radiation and the ocean advection anomalies jointly contributed to the anomalous warming in the three successive summers (June-August) in the SYS and the north part of the ECS. In addition, the reduction of surface wind speeds during the 2016 and 2017 summers further weakened the vertical mixing, thereby enhancing the anomalous warming in the north part of the ECS adjacent to the SYS. During the three summers, the increases of shortwave radiation were closely related to the East Asian Summer Monsoon (EASM) variability, which reduced the cloud cover in the ECS and SYS, whereas the advection anomalies were mostly associated with regional wind anomalies. In summer 2018, upper ocean heat was transported into the central trough of the South Yellow Sea, accumulated in an anticyclonic eddy generated by the anomalous wind stress curls. Therefore, despite the primary driver of the MHWs is the EASM variation, regional processes are critical to driving the spatial pattern of the MHW intensity in the ECS and SYS.

1 **Drivers of marine heatwaves in the East China Sea and the South Yellow Sea in**  
2 **three consecutive summers during 2016-2018**

3 Guandong Gao<sup>1,2,3</sup>, Maxime Marin<sup>4,5</sup>, Ming Feng<sup>4\*</sup>, Baoshu Yin<sup>1,2,3,6\*</sup>, Dezhou  
4 Yang<sup>1,2,3</sup>, Xingru Feng<sup>1,2,3</sup>, Yang Ding<sup>7,2</sup>, Dehai Song<sup>7,2</sup>

5 <sup>1</sup> Key Laboratory of Ocean Circulation and Waves, Institute of Oceanology Chinese  
6 Academy of Sciences, Qingdao 266071, China

7 <sup>2</sup> Qingdao National Laboratory for Marine Science and Technology, Qingdao 266000,  
8 China

9 <sup>3</sup> Center for Mega Science, Chinese Academy of Science, 7 Nanhai Road, Qingdao,  
10 266071, P. R. China

11 <sup>4</sup> CSIRO Oceans and Atmosphere, Crawley, Western Australia, Australia,

12 <sup>5</sup> Institute for Marine and Antarctic Studies, University of Tasmania, Hobart,  
13 Tasmania, Australia,

14 <sup>6</sup> University of Chinese Academy of Sciences, Beijing 100049, China.

15 <sup>7</sup> Key Laboratory of Physical Oceanography, Ministry of Education, at Ocean  
16 University of China, Qingdao 266100, China

17

18

19

20

21

22

23

24 \*Corresponding author: Ming Feng

25 E-mail address: [ming.feng@csiro.au](mailto:ming.feng@csiro.au)

26 \*Corresponding author: Baoshu Yin

27 E-mail address: [bsyin@qdio.ac.cn](mailto:bsyin@qdio.ac.cn)

28 **Abstract**

29 In three consecutive years from 2016 to 2018, extreme ocean warming events, or  
30 marine heatwaves (MHW), occurred during boreal summers in the East China Sea  
31 (ECS) and South Yellow Sea (SYS), which is unprecedented in the past four decades  
32 based on the satellite record. In this study, we used a high-resolution hydrodynamic  
33 model based on FVCOM (Finite Volume Community Ocean Model) to simulate the  
34 evolution of these warming events. An upper ocean temperature budget (0-20m)  
35 analysis based on the model results shows that the shortwave radiation and the ocean  
36 advection anomalies jointly contributed to the anomalous warming in the three  
37 successive summers (June-August) in the SYS and the north part of the ECS. In  
38 addition, the reduction of surface wind speeds during the 2016 and 2017 summers  
39 further weakened the vertical mixing, thereby enhancing the anomalous warming in  
40 the north part of the ECS adjacent to the SYS. During the three summers, the  
41 increases of shortwave radiation were closely related to the East Asian Summer  
42 Monsoon (EASM) variability, which reduced the cloud cover in the ECS and SYS,  
43 whereas the advection anomalies were mostly associated with regional wind  
44 anomalies. In summer 2018, upper ocean heat was transported into the central trough  
45 of the South Yellow Sea, accumulated in an anticyclonic eddy generated by the  
46 anomalous wind stress curls. Therefore, despite the primary driver of the MHWs is  
47 the EASM variation, regional processes are critical to driving the spatial pattern of the  
48 MHW intensity in the ECS and SYS.

49

50 **Plain language Summary**

51 Marine heatwaves, known as periods of extreme warming at the sea surface, can last  
52 for days to months and cause damages to the marine environment and marine life. In  
53 the East China Sea and the South Yellow Sea, the frequent occurrences of harmful  
54 algae blooms are often associated with marine heatwaves. Satellite data reveals that

55 marine heatwaves occurred in the East China Sea and the South Yellow Sea during  
56 the three boreal summers from 2016 to 2018, which is unprecedented in the past four  
57 decades. Using a numerical model of the ocean, we examined the marine heatwaves  
58 during these three successive summers. We show that the increased solar radiation,  
59 ocean current anomalies, and reduced vertical mixing were three critical factors for  
60 the warming events in the three summers. This study helps the fisheries and  
61 aquaculture industries in the East China Sea and the South Yellow Sea to better  
62 manage the environmental risks under a warming climate by predictions of marine  
63 heatwaves.

64

#### 65 **Key points**

- 66 ● Marine heatwaves in the ECS and SYS during 2016-2018 summers were caused  
67 by shortwave radiation, current and vertical mixing anomalies
- 68 ● Shortwave radiation increases in summers were due to reductions of the cloud  
69 cover, closely related to the East Asian Summer Monsoon variability
- 70 ● An anticyclonic eddy in SYS in summer 2018, driven by regional wind anomalies,  
71 played a significant role in trapping anomalous heat

72

73 **1. Introduction**

74 The occurrences of extreme warming events in the world oceans, the marine  
75 heatwaves (MHW; Hobday et al., 2016), are becoming more frequent in the recent  
76 decade. There have been record MHW events in coastal waters off Australia (Feng et  
77 al. 2013; Benthuisen et al., 2014; Oliver et al., 2017; Benthuisen et al., 2018), the  
78 northern Mediterranean Sea (Sparnocchia et al., 2006; Olita et al., 2006), the  
79 northwest Atlantic (Chen et al., 2014), the northeast Pacific (Bond et al., 2015; Di  
80 Lorenzo and Mantua, 2016), and coastal waters off South African (Schlegel et al.,  
81 2017). MHW events have drawn great attentions due to their extraordinary influences  
82 on the regional biodiversity and mortality of commercial fisheries (Mills et al., 2012;  
83 Caputi et al., 2016; Oliver et al., 2017).

84 There have also been observations of extreme MHW events occurring in the East  
85 China Sea (ECS; Tan and Cai et al., 2018), and the Yellow Sea in recent years. As a  
86 marginal sea of the Pacific Ocean, the ECS is connected to the South Yellow Sea  
87 (SYS) to the north (along a section from the mouth of the Changjiang River, China to  
88 Jeju Island, Korea), and is separated from the South China Sea and the Philippine Sea  
89 by the Taiwan Strait and the Ryukyu Islands (Figure 1). The ECS and the SYS are  
90 known as one of the most developed continental shelf areas globally (Yanagi and  
91 Takahashi, 1993), and they are referred to as the ECS system (ECSs) in this study.

92 In the ECSs, the frequent occurrences of harmful algae blooms are associated to  
93 anomalous warm conditions, or MHWs (Cai et al., 2016). The anomalous warming  
94 would enhance stratification and restrict phytoplankton in the top of water column  
95 where more light is available for them to thrive. In addition, anomalous warming in  
96 late spring and early summer greatly reduces the abundance of warm-water species of  
97 zooplankton like *C.sinicus*, which in turn reduces grazing pressure on phytoplankton  
98 and stimulates phytoplankton or harmful algae blooms (Cai et al., 2016). Such blooms  
99 significantly lower the oxygen levels and consequently result in the spreading of  
100 coastal hypoxic zone, endangering coastal and marine ecosystems (Cai et al., 2016).

101 Hence, it is crucial to investigate the characteristics and controlling mechanisms of  
102 marine heatwaves in the ECSs.

103 The ECSs has experienced steady warming trends during the recent four decades (Yeh  
104 and Kim 2010; Oey et al., 2013; Cai et al., 2017). Both Yeh and Kim (2010) and Oey  
105 et al. (2013) studied the decadal warming and its drivers during winter, whereas Cai et  
106 al. (2017) investigated the inter-decadal warming during both winter and summer.  
107 Nevertheless, event specific studies about MHWs in ECSs are rare. In August 2016,  
108 record-breaking monthly mean sea surface temperature (SST) emerged in the ECS, as  
109 indicated in the NOAA OISST (National Oceanic and Atmospheric Administration's  
110 Optimum Interpolation Sea Surface Temperature) data (Tan and Cai, 2018).  
111 Strikingly, the NOAA OISST data show that SST anomalies in August 2017 were  
112 even stronger and covered wider areas in the ECSs, followed with another warm  
113 summer in 2018. Three successive warm summers, including two record-breaking  
114 ones, are unprecedented in the past four decades, which motivates us to examine the  
115 anomalous atmospheric and oceanic conditions responsible for those MHWs.

116 The summer circulation system in the ECSs mainly consists of cyclonic  
117 (anticlockwise) circulation over the SYS (Beardsley et al., 1992; Yanagi and  
118 Takahashi, 1993; Xia et al., 2006), and the Taiwan–Tsushima warm currents (Isobe,  
119 2004 and 2008) and the Kuroshio Current (Wang and Oey, 2014; Yang et al., 2018) in  
120 the ECS. There are also the northward Chinese coastal currents (Naimie et al., 2001).  
121 NCEP (National Center for Environmental Prediction) or ECMWF (European Centre  
122 for Medium-Range Weather Forecasts) reanalysis data set are useful in exploring the  
123 warming trend of ECSs on long time scales (Yeh and Kim, 2010; Oey et al., 2013;  
124 Park et al., 2015; Cai et al., 2017), but they lack spatial resolution to capture the  
125 complicated current system in the ECSs. What is more, tides, which are important to  
126 the hydrodynamics in the ECSs (e.g. Naimie et al., 2001; Xia et al., 2006; Lozovatsky  
127 et al., 2007a, b), are not considered in the NCEP and ECWMF products. Therefore,  
128 ocean processes with respect to the warm summers during 2016-2018 may not be well

129 quantified by these reanalysis products (Tan and Cai, 2018). A well-validated regional  
130 model with high spatial resolution would be crucial to reproduce the anomalous  
131 warming patterns, thereby quantifying the contribution of responsible processes with  
132 better accuracy (Frölicher et al., 2018).

133 Major processes controlling summer surface temperature variations in the ECSs  
134 include heat advection by the ocean currents (Tan and Cai, 2018), air-sea heat flux,  
135 mainly controlled by the East Asian Summer Monsoon (Oey et al., 2013; Cai et al.,  
136 2017) and the Western Pacific Subtropical High (Matsumura et al., 2015; Tan and Cai,  
137 2018), and local vertical mixing (Xie et al., 2002). Different MHW events may  
138 involve different combinations of the processes. The aim of this study is to examine  
139 the processes responsible for three successive warm summers (June, July and August;  
140 JJA hereafter) in the ECSs by analyzing regional ocean model results.

141 The rest of the paper is organized as follows. The data, numerical modelling, and  
142 analysis method are introduced in section 2. Section 3 presents the details of  
143 temperature budget analysis and the major drivers. Section 4 summarizes the main  
144 findings.

## 145 **2. Data and Methods**

### 146 **2.1 SST data**

147 The SST data used for the validation of numerical model results in this study are  
148 NOAA OISST version 2 (Reynolds et al., 2007), which is a daily and  $0.25^\circ \times 0.25^\circ$   
149 gridded product of Advanced Very High Resolution Radiometer (AVHRR) satellite  
150 data provided by the NOAA/OAR/ESRL PSD, Boulder, Colorado, USA, accessed  
151 from their website at <https://www.esrl.noaa.gov/psd/>. Satellite bias was corrected with  
152 respect to in-situ data from ships and buoys (Reynolds et al., 2007). Data are available  
153 from September 1, 1981 to present.

### 154 **2.2 Atmospheric data**

155 To investigate the role and contribution of atmospheric and radiative forcing to the  
156 three consecutive warm summers, we used data from the NCEP Climate Forecast  
157 System Reanalysis version 2 product (CFSRv2: Saha et al., 2013). CFSRv2 is the  
158 reanalysis product of the fully coupled atmosphere-ocean-land model Climate  
159 Forecast System version 2 (CFSv2) implemented in March 2011. It uses the NCEP  
160 Global Forecast System (GFS) as its atmospheric model and the Modular Ocean  
161 Model, version 3 (MOM3), from the Geophysical Fluid Dynamics Laboratory  
162 (GFDL). CFSv2 includes two data assimilation systems namely the  
163 NCEP-Department of Energy (DOE) Global Reanalysis 2 (Kanamitsu et al., 2002)  
164 and the Global Ocean Data Assimilation System (GODAS; Behringer, 2007). Data  
165 used in this study includes hourly 10m winds, surface air temperature, air pressure  
166 and relative humidity, downward longwave and shortwave radiations at the surface,  
167 and precipitation rates and geopotential height at 850 hPa and 500 hPa on a  $0.2 \times 0.2$   
168 degrees spatial grid. Monthly outputs of the first version of CFSR (Saha et al., 2010a,  
169 b) at a resolution of  $0.312 \times 0.312$  degrees were used to compare recent atmospheric  
170 conditions with the long-term climatology.

## 171 **2.3 Numerical modelling**

### 172 **2.3.1 Model setup**

173 The Unstructured-grid Finite Volume Community Ocean Model (FVCOM; Chen et  
174 al., 2003) is used. The model mesh and configuration used in study are the same as  
175 those in Ding et al. (2018) and Ding et al. (2019), which investigated coastally  
176 trapped waves and ocean current fluctuations under storms in the ECSs. In this study,  
177 the model is named as FVCOM-ECSs.

178 The FVCOM-ECSs mesh consists of 70,479 nodes and 136,612 elements, covering  
179 the Bohai Sea (BS), the North Yellow Sea (NYS), the SYS and the ECS (Figure 1b).  
180 The horizontal resolution increases gradually from 20 km near the open boundary  
181 toward around 1 km in the coastal regions. In the vertical direction, 30 sigma layers  
182 are evenly distributed in the terrain-following coordinate. The bathymetry data used in

183 this model are primarily obtained from DBDB5 (U.S. Naval Oceanographic Office  
184 1983), combined with topography data from the China coastal sea chart database to  
185 gain higher resolutions along the Chinese coast. The wet and dry treatment is  
186 embedded in the model. The vertical eddy viscosity is calculated using Mellor and  
187 Yamada (1982) turbulent closure model and the horizontal diffusion coefficient is  
188 determined by Smagorinsky eddy parameterization method (Smagorinsky 1963).

189 In the FVCOM-ECSs, the open boundary forcing such as sub-tidal sea surface heights,  
190 currents, temperature and salinity on daily time scales were derived from the global  
191 model of Estimating the Circulation and Climate of the Ocean Phase II (ECCO2,  
192 Menemenlis et al. 2008). Hourly tidal levels and barotropic tidal currents were  
193 obtained from TPXO 7.2 based on nine tidal constituents ( $M_2$ ,  $S_2$ ,  $N_2$ ,  $K_1$ ,  $O_1$ ,  $Q_1$ ,  $M_4$ ,  
194  $MS_4$ ,  $MN_4$ ). The global ECCO2 model outputs were also used for the initial  
195 temperature and salinity fields of the FVCOM-ECSs. The ECCO2 data can be derived  
196 from the Asia–Pacific Data-Research Center of the IPRC (APDRC,  
197 <http://apdrc.soest.hawaii.edu/index.php>). Surface forcing data acquired from CFSRv2  
198 were hourly 10m winds, surface air temperature and relative humidity, downward  
199 longwave and shortwave radiations at the surface, and precipitation rates. Latent heat  
200 flux and sensible heat flux were calculated using bulk formulation (Fairall et al., 1996;  
201 Subroutine COARE26Z in FVCOM 3.2.2). Two major rivers (Changjiang River and  
202 Yellow River) were considered: the temperature was specified referring to daily  
203 Multi-sensor Ultra-high Resolution (MUR) SST; the salinity was set to be constant at  
204 5 psu; monthly-averaged freshwater discharge data were provided by the Information  
205 Center of Water Resources, Bureau of Hydrology, Ministry of Water Resources of P.  
206 R. China.

207 The external and internal time steps are 5 s and 50 s, respectively. The model run was  
208 carried out from January 01, 2012 to August 31, 2018. The first year was regarded as  
209 spin up and model outputs from January 01, 2013 were analyzed.

### 210 **2.3.2 Model validation**

211 The FVCOM-ECSs has been extensively validated in terms of barotropic tides,  
212 sub-tidal sea levels and currents, temperature, salinity, and surface waves (Ding et al.,  
213 2011; Ding et al., 2018; Gao et al., 2018; Ding et al., 2019). Here we focus on the  
214 validation of the model SST variability by comparing with the NOAA OISST.

215 Compared with satellite observations, the FVCOM-ECSs SST has a mean bias around  
216  $0.2^{\circ}\text{C}$ , with RMSE smaller than  $0.8^{\circ}\text{C}$  in most parts of the study area (Figure 3a, b).  
217 The correlation coefficients between the satellite and FVCOM-ECSs SST are above  
218 0.95 in most of the ECSs (Figure 3c). Thus, the FVCOM-ECSs has reproduced the  
219 observed SST variability (Figure 4).

220 Three-year (2013 to 2015) averaged model results were used as the normal-year  
221 average or baseline reference in this study. The 2013 to 2015 averaged SST is quite  
222 similar to the long-term (1982 to 2016) averaged SST (support information Figure S1),  
223 so it is reasonable to use the 3-year average as the baseline reference. Figure 4 shows  
224 that the FVCOM-ECSs successfully captured the position and strength of SST  
225 anomalies (relative to the normal-year average) from 2013 to 2018: one warm  
226 summer in 2013, two neutral summers in 2014 (slightly cold) and 2015, and three  
227 consecutive warm summers from 2016 to 2018. Anomalous warm SSTs were  
228 primarily located in the SYS and the north part of the ECS. In July 2017, positive SST  
229 anomalies were the highest and covered the largest area.

230 During summers (JJA) from 2013 to 2018 (Figure 5), the FVCOM-ECSs could  
231 reproduce daily SST variations in most parts of the study domain, except in the near  
232 shore areas and in the KC region. Two boxes (Boxes SYS and NECS), with strong  
233 SST anomalies and good model performances (Figures 3-5), are used for heat balance  
234 analysis. Box SYS covers the China shelf and the center trough of the SYS  
235 ( $121\text{-}125.9^{\circ}\text{E}$ ,  $33.65\text{-}37.4^{\circ}\text{N}$ ) and Box NECS is the central shelf of the ECS, located  
236 in the north part of ECS adjacent to the SYS ( $123\text{-}126^{\circ}\text{E}$ ,  $30\text{-}33.65^{\circ}\text{N}$ ). The model  
237 accurately reproduced the observed normal-year average (2013 to 2015 mean) SST  
238 evolution in Boxes SYS and NECS, as shown in a 11-day running mean (Figures 6a,

239 b). The SST anomalies relative to normal-year average are also compared well with  
240 observations for both Boxes in 2016, 2017 and 2018 (Figures 6c, d). For Box SYS,  
241 the modelled SST anomalies generally agreed well with satellite data during JJA in  
242 2016 and 2018, whereas the peak SST anomalies in July 2017 were underestimated by  
243 the model. For Box NECS, in 2017 and 2018, the model simulated the increases of  
244 SST anomalies from June 1<sup>st</sup> to the peak values, however, it underestimated the decay  
245 of the SST anomalies after the peak; SST anomalies in 2016 experienced two peaks  
246 and the model slightly underestimated the first peak but well captured the second peak.  
247 The direct comparison of daily SST in JJA during 2016-2018 between the model  
248 results and satellite data is provided in the support information (Figure S2). Overall,  
249 the model was able to reproduce the normal-year averaged SST and increasing trends  
250 of SST anomalies from the beginning of June to the MHW peaks for both Boxes SYS  
251 and NECS in 2016-2018.

#### 252 **2.4 Marine Heatwave Definition and Metrics**

253 The Hobday et al. (2016) definition was used to characterize the MHW events in  
254 summers during 2016-2018, that is, a MHW is defined as an anomalously warm,  
255 discrete, and prolonged event, which can be quantitatively described as periods of  
256 time when daily temperatures are above a particular threshold for at least five days.  
257 The threshold is calculated as the 90<sup>th</sup> percentile of daily temperature variability  
258 across a >30-year period, within an 11-day window centered on a specific day of the  
259 year. This seasonally varying threshold allows for events to occur at any time of the  
260 year. Threshold and climatological values were derived using the NOAA OISST.  
261 Here, we chose a fixed baseline climatological period following Hobday et al. (2016).  
262 Due to the limited length of observation time series, it was not possible to adopt a  
263 moving baseline, as advocated for climate change studies (Jacox, 2019).

264 Three MHW metrics are used in the study: the duration (days between the start and  
265 end dates), the maximum intensity (maximum SST anomalies during a single event)  
266 and the cumulated intensity (sum of daily intensity anomalies measured in °C days).

## 267 2.5 Upper ocean temperature budget

268 The upper ocean temperature budget is calculated with the volume-averaged  
 269 temperature tendency equation from sea surface to a fixed depth  $h$ , and within a  
 270 surface area  $A$  (Feng et al., 2008; Jessica et al., 2014 and Oliver et al., 2017).

$$271 \quad \frac{\partial \langle T \rangle}{\partial t} = \underbrace{-\langle u_H \cdot \nabla T \rangle}_{Adv_H} - \underbrace{\left\langle w \frac{\partial T}{\partial z} \right\rangle}_{Adv_V} + \underbrace{\frac{1}{\rho c_p A} \int^A \frac{Q}{h} dA}_{Q_v} - \underbrace{\frac{1}{Ah} \int^A \left( \kappa_v \frac{\partial T}{\partial z} \right)_{-h} dA}_{Dif_V} - \underbrace{\langle \nabla \cdot (\kappa_h \nabla T) \rangle}_{Dif_H} \quad (1)$$

272 Where  $T$  is the temperature;  $t$  is the time;  $\langle \rangle = \frac{1}{hA} \int_{-h}^0 dz dA$  represents volume  
 273 average;  $u_H$  is the horizontal current vector;  $\nabla$  is the horizontal gradient operator;  $w$  is  
 274 the vertical current;  $Q = Q_{sw}(0) - Q_{sw}(h) + Q_{lw} + Q_{lh} + Q_{sh}$  is the net heat flux which is the  
 275 summation of shortwave radiation absorbed in the top layer  $Q_{sw}(0) - Q_{sw}(h)$ , longwave  
 276 radiation  $Q_{lw}$ , latent heat flux  $Q_{lh}$ , and sensible heat flux  $Q_{sh}$ .  $Q_{sw}(z)$  is the shortwave  
 277 radiation penetrated at depth  $z$  (see details in Paulson and Simpson, 1977).  $\kappa_v$  and  $\kappa_h$   
 278 are the horizontal and vertical eddy diffusivities. The temporal change rate of  
 279 volume-averaged temperature  $RATE_V$  is decomposed into following terms: horizontal  
 280 advection  $Adv_H$ , vertical advection  $Adv_V$ , net heat flux  $Q_v$ , vertical diffusion  $Dif_V$  and  
 281 horizontal diffusion  $Dif_H$ . The model integrated the terms for the volume-averaged  
 282 temperature tendency equation over every external time step (5s) and recorded the  
 283 output at daily interval.

284 The total advection ( $Adv_H + Adv_V$ ) were diagnostic output from the model, however,  
 285 the directions were only distinguished into inward or outward the “tracer volume  
 286 element” (see the finite volume method in Chen et al., 2013). Therefore, the advection  
 287 contributions from the five boundaries of Boxes SYS and NECS were calculated  
 288 based on daily-averaged temperature and current outputs from the model using a  
 289 decomposition method (Lee et al., 2004; Feng et al., 2008; Zhang et al., 2018):

$$290 \quad Adv_H + Adv_V =$$

$$291 \quad \underbrace{\frac{1}{V} \iint_{Sb} v_{South} (T_{South} - \langle T_{Box} \rangle) dx dz}_{South} - \underbrace{\frac{1}{V} \iint_{Nb} v_{North} (T_{North} - \langle T_{Box} \rangle) dx dz}_{North} + \underbrace{\frac{1}{V} \iint_{Wb} u_{West} (T_{West} - \langle T_{Box} \rangle) dy dz}_{West}$$

$$292 \quad - \underbrace{\frac{1}{V} \iint_{Eb} u_{East} (T_{East} - \langle T_{Box} \rangle) dy dz}_{East} + \underbrace{\frac{1}{V} \iint_A w_{-h} (T_{-h} - \langle T_{Box} \rangle) dx dy}_{Vertical} + Adv_{res} \quad (2)$$

293  $S_b$  (*South*),  $N_b$  (*North*),  $W_b$  (*West*),  $E_b$  (*East*) and *Vertical* represent the south, north,  
 294 west, east and vertical boundaries of a box respectively.  $T_{South}$ ,  $T_{North}$ ,  $T_{West}$ ,  $T_{East}$  and  
 295  $T_h$  are daily-averaged temperature at south, north, west, east and vertical boundaries.  
 296  $T_{box}$  is the daily-averaged temperature in a box and  $V$  is the volume of a box.  $v_{South}$  and  
 297  $v_{North}$  are daily-averaged meridional currents at south and north boundaries  
 298 respectively, while  $u_{West}$  and  $u_{East}$  are daily-averaged zonal currents at west and east  
 299 boundaries respectively. The residuals ( $Adv_{res}$ ) in Eq (2) may come from the  
 300 interpolation errors from unstructured grids into the regular boundaries. The advection  
 301 decomposition has been widely used in heat budget analysis on different time scales  
 302 (Lee et al., 2004; Feng et al., 2008; Bond et al., 2015; Fathrio et al., 2017; Zhang et al.,  
 303 2018; Asbjørnsen et al., 2019; Hristova et al., 2019).

304 Advection-induced temperature anomalies are associated to the anomalies of currents  
 305 and temperature. Following Lee et al. (2004), contributions of advection at any  
 306 boundary can be further decomposed into (Using the south boundary as an example):

$$\begin{aligned}
 307 \quad & \frac{1}{V} \underbrace{\iint_{S_b} v_{South} (T_{South} - \langle T_{Box} \rangle) dx dz}_{South} = \\
 308 \quad & \frac{1}{V} \underbrace{\iint_{S_b} \bar{v}_{South} (\bar{T}_{South} - \langle \bar{T}_{Box} \rangle) dx dz}_{Normal-year\ average} + \frac{1}{V} \underbrace{\iint_{S_b} v'_{South} (\bar{T}_{South} - \langle \bar{T}_{Box} \rangle) dx dz}_{Current\ anomaly} + \\
 309 \quad & \frac{1}{V} \underbrace{\iint_{S_b} \bar{v}_{South} (T'_{South} - \langle T'_{Box} \rangle) dx dz}_{Temperature\ anomaly} + \frac{1}{V} \underbrace{\iint_{S_b} v'_{South} (T'_{South} - \langle T'_{Box} \rangle) dx dz}_{Current\ and\ temperature\ anomaly} \quad (3)
 \end{aligned}$$

310 Over bar represents the normal-year (2013-2015) average and prime represents the  
 311 anomaly in an individual year from 2016-2018. The four terms in the right hand side  
 312 of Equation (3) represent, respectively, the advection of mean temperature difference  
 313 by mean flow (*Normal-year average*), the advection of mean temperature difference  
 314 by anomalous flow (*Current anomaly*), the advection of anomalous temperature  
 315 difference by mean flow (*Temperature anomaly*), and the advection of anomalous  
 316 temperature difference by anomalous flow (*Current and temperature anomaly*) (Lee  
 317 et al., 2004).

### 318 **3. Results**

### 319 **3.1 Characteristics of three successive warm summers from 2016 to 2018**

320 Figure 6 summarizes the MHW characteristics for the ECSs, derived from the OISST.  
321 In the large ECSs Box, both 2016 and 2017 summers had well-defined, unprecedented  
322 MHW events (Figures 2b-d), in terms of maximum intensity ( $3^{\circ}\text{C}$ ) in 2016 and in  
323 terms of duration and cumulated intensity (44 days and  $85.5^{\circ}\text{C}$  days) in 2017. There  
324 was a strong summer MHW in 1994, nearing maximum values of duration, intensity  
325 and cumulated intensity, which might be associated with the Asian heatwave during  
326 that summer (Park, and Schubert, 1994). MHWs during the 2018 summer were  
327 weaker than the two previous years, despite occurring at several short periods. Despite  
328 high values of MHW maximum intensity ( $2^{\circ}\text{C}$ ), 2018 summer events lasted less than  
329 10 days, resulting in a weak cumulative intensity (Figures 2b-d). Overall, more  
330 frequent summer MHW events occurred after 1997 (Figures 2b-d). The decadal  
331 increase in MHW frequency is likely due to the long-term warming trend observed  
332 since the beginning of the 20th century (Oliver, 2019; Oliver et al., 2018), although  
333 there appears to be a halt in the warming trend in the ECSs box since the late 1990s  
334 (Figure 2a).

335 In both the SYS and the NECS boxes, the main 2016 summer MHW started in early  
336 August, with maximum SST anomalies peaked in the middle of the month, a few days  
337 earlier in the SYS than in the NECS, both reaching  $\sim 4^{\circ}\text{C}$ . While temperatures were  
338 above the climatological average in the SYS at the start of the 2016 summer, there  
339 was a progressive warming of SSTs in the NECS, from a relatively cool state at the  
340 start of summer (Figures 6e and 6h). In 2017, SSTs were above the MHW threshold at  
341 the start of the summer for both boxes and remained above the threshold during most  
342 of the summer (Figures 6f and 6i). The main event occurred in early June and late  
343 June for the SYS and NECS and lasted until mid-August. In the 2018 summer,  
344 temperatures in the NECS only briefly crossed the MHW threshold, not persistent  
345 enough to be classified as a MHW (Figure 6j). However, a strong MHW occurred in

346 the SYS, starting late July and lasting for about 20 days (Figure 6g), with a maximum  
347 intensity of about 3°C.

### 348 **3.2 Temperature budget**

349 SST anomalies during 2016-2018 generally emerged in June and peaked in July or  
350 August, so that we focused the upper ocean temperature budget analysis during the  
351 JJA period. In both Boxes SYS and NECS (Figures S3, S4), anomalous warmings  
352 were most significant in the top 20 m in the summers of 2016 to 2018. In 2018, the  
353 anomalous warming in Box SYS extended to the subsurface layer toward the end of  
354 summer. Subsurface warming was also present in Box NECS during the first half of  
355 summer 2017. In this study, we used 20 m as the control volume depth as: 1) the  
356 anomalous warmings were most significant in the top 20 m for both boxes; 2) 20 m  
357 reflects the summer mixed layer depth; and 3) the model SST agreed well with  
358 satellite data. In areas where water depth is shallower than 20 m, the integration is  
359 between sea surface and sea floor. It is noted that water depths are deeper than 20 m  
360 in most areas in Boxes SYS and NECS.

#### 361 **Box SYS**

362 During a normal year, the top 20 m temperature in the SYS box warmed up from  
363 about 16°C on June 1<sup>st</sup> to about 23°C toward the end of summer, with a 15°C warming  
364 contribution from the net air-sea heat flux, countered by a ~7°C cooling from vertical  
365 mixing (Figure 7a).

366 Positive temperature anomalies in the SYS during summer 2016-2018 were mainly  
367 caused by the net air-sea heat flux and advection anomalies (Figures 7b-d): In 2016,  
368 the anomalous net heat flux dominated the temperature variability; in 2017, net heat  
369 flux dominated in June and July, but the contribution of advection anomalies became  
370 important during the first half of August; in 2018, both the net heat flux and advection  
371 anomalies drove the rise of the temperature anomalies, with the advection effect more

372 important in the second half of August. The initial temperature anomaly of 0.5°C on 1  
373 June 2017 also contributed to the warm event during that summer.

374 In the air-sea heat flux, shortwave radiation dominated not only the temperature  
375 variation during a normal year but also the temperature anomalies during the three  
376 anomalous summers (Figures 8a-d). Anomalous shortwave radiations warmed the  
377 SST during the whole JJA in 2017 and during the latter half of JJA in 2016 and 2018,  
378 whereas the other heat flux anomaly terms had weak warming or slightly cooling  
379 effects.

380 Anomalous heat advection across the south, west and vertical (bottom) boundaries  
381 contributed to the summer warming in Box SYS in 2016 and 2017 (Figures 8f, g).  
382 The effects of advection were much more prominent in 2018: vertical advection  
383 anomalies and horizontal advection anomalies at the south boundary caused  
384 significant anomalous warmings in the second half of the 2018 summer (Figure 8h).

385 We further examined the causes of the peak temperature anomalies in Box SYS for  
386 the three summers (Table S1). The shortwave radiation was the most important factor,  
387 with contributions of 1.51°C, 0.8°C and 1.67°C during the summers in 2016, 2017  
388 and 2018, respectively. In 2018, the contribution of advection to the peak temperature  
389 anomaly reached 1.55 °C, with 1.04 °C and 0.72 °C contributed across the vertical  
390 and south boundaries, respectively. Regression analysis shows that daily anomalous  
391 temperature changes were significantly correlated to both advection and shortwave  
392 radiation anomalies during JJA in Box SYS (Figure S5).

### 393 **Box NECS**

394 Whereas net air-sea heat flux and advection anomalies played critical roles in  
395 anomalous temperature changes in Box NECS, the role of vertical mixing also  
396 became important (Figures 9b-d). Shortwave radiation anomalies still played a  
397 leading role among all the air-sea heat flux terms to warm the upper ocean (Figures  
398 10b-d). In 2016, shortwave radiation anomalies became significant from mid-August

399 while the reduction of latent heat loss provided additional warming effects (Figure  
400 10b), as a result of reduced wind speeds compared to normal-year averages (support  
401 information Figure S6). In 2017, wind speeds were reduced but the specific humidity  
402 were also reduced (support information Figure S7), thus latent heat flux showed an  
403 overall cooling effect. The shortwave radiation anomalies were most significant in  
404 2018, dominating over the other flux terms (Figure 10d).

405 Advection was important during summers in 2017 and 2018 (Figures 10g, h),  
406 contributing 0.84 °C and 1.36°C to the peak temperature anomalies respectively  
407 (Table S2). In 2016, temperature anomalies induced by advection were generally  
408 negative (Figure 10f). Whereas effects of advection at various boundaries were quite  
409 different among three summers, anomalous horizontal advection across the south  
410 boundary consistently contributed to warming events (Figures 10f-h).

411 The reduction of vertical mixing was crucial to the summer warming in Box NECS in  
412 2016 and 2017 (Figures 9b, c). Vertical mixing contributed to 0.87 °C and 1.12 °C of  
413 the maximum surface temperature anomalies in 2016 and 2017, respectively, and the  
414 anomalies of daily temperature changes had significant correlations with that caused  
415 by vertical mixing variability (Figure S8).

416 In the next three subsections, we discuss the drivers of the anomalous increase of  
417 shortwave radiation, the ocean current anomalies, and the reduction of upper ocean  
418 vertical mixing in Box NECS.

### 419 **3.3 Shortwave radiation**

420 Positive anomalies of shortwave radiations occurred during all three summers in  
421 2016-2018, relative to 2013-2015 average, in a zonal band between 30-35°N  
422 extending from eastern China to Japan (Figures 11a-c). The magnitude and pattern of  
423 the positive anomalies of shortwave radiation remained the same when using a  
424 longer-term climatology (Figure S9). The main weather system controlling cloud  
425 formation and rainfall in the ECS during summer is the East Asian Summer Monsoon

426 (EASM; Ding and Chan (2005). The onset of the EASM expresses itself as enhanced  
427 rainfalls in the South Asia region at the end of May, extending abruptly to the  
428 Yangtze River basin in eastern China in early June. Monsoonal rain then moves  
429 northeastward towards the ECSs and the Korean Peninsula, expressed as a frontal  
430 cloud zone called the Meiyu-Baiu front/rainband (Ninomiya, 2004).

431 The mechanisms of the EASM variability are still not fully understood due to the  
432 complexity of the system. The primary external forcing for the onset of the EASM are  
433 believed to be the Pacific and Indian Ocean SST variations, as well as the snow cover  
434 on the Tibetan Plateau (Ding and Chan, 2005; Zhou et al., 2009). However, internal  
435 variability of the regional atmospheric circulation determines the position and  
436 intensity of the cloud front. Pressure and wind anomalies at 850hPa showed a  
437 westward shift of the Western Pacific Subtropical High (WPSH) in 2016 and 2017  
438 and a northward displacement of the WPSH in 2018 (Figures 11g-i), as compared  
439 with climatology (Figure S10). The intensity and location of the WPSH are well  
440 correlated with the Meiyu-Baiu front activity and can represent leading EOF modes of  
441 the EASM (Huang et al., 2018; Oppenheim et al., 1999; Wang et al., 2013). The  
442 associated changes in low level circulation likely modified the EASM intensity via a  
443 decrease of moisture transport and/or horizontal thermal gradient (Lee et al., 2013;  
444 Ding and Chan, 2005), or shifted the location of the Meiyu-Baiu front (Gao et al.,  
445 2016).

446 The mid-level East Asian Westerly Jet (EAWJ) was also found to have a profound  
447 impact on the EASM. Several studies showed that the position of the EAWJ impacted  
448 the amount of precipitation in the Yangtze River basin (Du et al., 2009; Xuan et al.,  
449 2011). Recently, the EAWJ intensity was found to be positively correlated with  
450 precipitation in the Yangtze River basin (Wang and Zuo, 2016). Anomalies of winds  
451 at 500hPa showed that the EAWJ was weaker in 2017 and shifted northward in 2016  
452 and 2018 (Figures 11d-f), helping to weaken the frontal system and increase  
453 shortwave radiation irradiance.

454 Despite the roles that both the WPSH and the EAWJ likely played in increasing  
455 shortwave irradiance during the summer of 2016-2018, our understanding of the  
456 complex EASM system remains limited. Further research is needed to explain the  
457 recent increases of summer shortwave radiations over the ECSs.

### 458 **3.4 Ocean currents**

459 Since the contribution of advection to the anomalous warming is determined by the  
460 variability of ocean currents and temperature. The effects of current anomalies played  
461 a more important role than those due to temperature anomalies for both Boxes  
462 (Figures S12, S13). Thus, in this section, we further examine the effects of current  
463 anomalies during the three warm summers.

464 As shown in Figure S11a (support information), the FVCOM-ECSs has successfully  
465 reproduced the cyclonic circulation (jet like southward currents in the west portion  
466 and northward currents in the east portion of the central trough) in the SYS (Beardsley  
467 et al., 1992; Yanagi and Takahashi, 1993; Xia et al., 2006), northward currents along  
468 the Chinese coast (Naimie et al., 2001), and the Taiwan–Tsushima warm current  
469 system (Isobe, 2004 and 2008). Current anomalies averaged during JJA were much  
470 prominent in 2018 than those in 2016 and 2017.

471 For a better illustration, current anomalies during the periods from June 1<sup>st</sup> to the day  
472 when peak temperature anomalies occurred during JJA in each year (2016 to 2018)  
473 are plotted in Figures 12a-c (Box SYS) and 13a-c (Box NECS). The anomalies of  
474 wind stress and stress curls averaged during corresponding periods are shown in  
475 Figures 12g-i (Box SYS) and 13g-i (Box NECS). Normal-year averages (2013-2015)  
476 and anomalies (2016-2018) of wind stress and wind stress curls averaged during JJA  
477 can be seen in Figure S14. To investigate the local wind effects on the current system,  
478 we conducted a model run (Experiment 1) in which we replaced the wind forcing in  
479 JJA 2016 to 2018 with the normal-year averaged wind forcing (2013 to 2015 average)  
480 and then analyzed the current anomalies averaged during the corresponding periods  
481 (Figures 12d-f and 13d-f).

482 **Box SYS**

483 In 2017, anomalous downwelling covered more than half of Box SYS and northward  
484 current anomalies were found in the west part of south boundary (Figure 12b), where  
485 temperatures were higher than the box average, both contributing to the maximum  
486 temperature anomalies of Box SYS. In 2018, anticyclonic current anomalies and  
487 downwelling dominated the whole Box SYS (Figure 12c). Northward current  
488 anomalies were significant at the south boundary as well. Therefore, advection in the  
489 south and vertical boundaries contributed to more than half of the maximum  
490 temperature anomalies of Box SYS in 2018. The current anomalies were absent in  
491 experiment 1 (Figures 12d-f), confirming that current anomalies in Box SYS were due  
492 to the regional wind anomalies.

493 **Box NECS**

494 Northward currents along the Chinese coast (31 to 35°N; west to 124°E) were  
495 strengthened (Figures 13b, c) by the anomalous northward winds (Figures 13h, i) in  
496 both 2017 and 2018, which transported more heat into Box NECS from the south or  
497 west boundary. The anomalous wind stress curl also drove downwelling anomalies in  
498 2018 (Figure 13c), contributing to the anomalous warming.

499 In 2017, strengthened northeastward currents were found between 125 and 127°E in  
500 the east part of Box NECS, which transported more heat out of Box NECS at the east  
501 boundary (Figure 13b). However, current anomalies were southwestward between  
502 125 and 127°E in 2018 (Figure 13c), and were not sensitive to the local wind  
503 anomalies. Thus, currents anomalies between 125 and 127°E were likely due to  
504 inter-annual variations of the Tsushima Warm Currents (TsWC). The TsWC on the  
505 shelf of the ECS originates from Taiwan Warm Current (TWC) and intrusions from  
506 the Kuroshio Current (KC) (Fan, 1982; Guan and Fang, 2006; Guo et al., 2006; Ma et  
507 al., 2010). The TsWC variability is primarily forced by the open ocean processes  
508 through the KC rather than TWC (Yang, 2007; Zheng et al., 2009; Ma et al., 2010).

509

### 510 **3.5 Vertical mixing**

511 Figures 14a, b shows that anomalies of daily temperature changes in Box NECS  
512 during three warm summers were remarkably well correlated with vertical diffusion  
513 anomalies, other than vertical temperature gradient anomalies. From the model,  
514 vertical diffusion at 20 m depth averaged during JJA was reduced in 2016 and 2017  
515 and enhanced in 2018 (Figure 14c), thus, the vertical mixing anomalies contributed to  
516 the anomalous warming in 2016 and 2017 but not in 2018. Surface winds play a major  
517 role in driving the vertical mixing in the upper layer of the ECSs (Park and Chu 2007;  
518 Xuan et al., 2012). Note the magnitudes of wind speeds in Box NECS were reduced in  
519 2016 and 2017 but increased in 2018 (Figures S6d-g). Temperature anomalies in Box  
520 NECS had a sharp decrease near the end of August in 2018 (Figure 9d), which was  
521 probably related to the enhanced vertical mixing associated with the passage of  
522 Typhoon Soulik.

523 When the model was driven by the normal-year averaged wind speeds (experiment 1),  
524 the vertical diffusion had negligible differences among three warm summers (Figure  
525 14d). This further confirms the role of wind speed anomalies on the anomalous  
526 vertical mixing. Note that magnitudes of winds speeds in experiment 1 were smaller  
527 than the normal year (Figures S15), thus the vertical eddy diffusions (2016 to 2018) in  
528 experiment 1 were weaker than the normal year averages (Figure 14d).

### 529 **4. Summary and conclusion**

530 The ECSs (East China Sea and the South Yellow Sea) experienced unprecedented  
531 MHW events during three consecutive summers from 2016 to 2018. Using the outputs  
532 from a well-validated hydrodynamics model with high spatial resolutions, we  
533 investigated the roles of oceanic processes and air-sea heat flux in controlling the  
534 anomalous upper ocean warming in two regions in the ECSs. Temperature budgets for  
535 the top 20 m in Boxes SYS and NECS illustrate that these warm summers were

536 associated with variations of shortwave radiation, advection and vertical mixing.  
537 Positive shortwave radiation anomalies during JJA from 2016 to 2018 were associated  
538 with the reduction of cloud covers in the Meiyu-Baiu front/rain region, and both the  
539 intensity and position of the WPSH and EAWJ likely contributed to the weakening  
540 and/or northward shift of Meiyu-Baiu front/rainband associated with the EASM.  
541 Northward current anomalies transported more heat into Boxes SYS and NECS from  
542 the south boundary during the three summers. Downwelling anomalies dominated  
543 Box SYS in 2018, which significantly enhanced the warming of the surface layer.  
544 Over whole Box SYS and west part of Box NECS, currents anomalies in both  
545 horizontal and vertical directions were forced by the anomalous wind stress and stress  
546 curls. In addition, reductions in the magnitudes of wind speeds over Box NECS  
547 weakened the local vertical mixing and significantly intensified the anomalous  
548 warming in 2016 and 2017. These wind anomalies are also likely associated with the  
549 monsoon variations. This research highlights that a high-resolution ocean modelling is  
550 important to understand the local and remote processes in the driving the MHWs in  
551 the coastal regions. The identification of roles of the East Asian Monsoon system in  
552 the MHW development in the ECSs may help understand MHW dynamics in other  
553 coastal regions at middle latitudes where the monsoon system is dominant during the  
554 summer season.

## 555 **Acknowledgement**

556 This work was supported by the National Natural Science Foundation of Shandong  
557 Province (No. 41406097) and CAS-CSIRO funding. This study was also supported by  
558 the Major Research Grant from Both the National Natural Science Foundation of  
559 China (NSFC) and the Provincial Natural Science Foundation of Shandong (NSFSD)  
560 (Ref No: U1806227). Dezhou Yang was supported by the National Natural Science  
561 Foundation of China (NSFC) (41576023, 41876019). Yang Ding was supported by  
562 the National Natural Science Foundation of China (No. 41430963). The  
563 FVCOM-ECSs model data is available from the Marine Science Data Center of

564 Institute of Oceanology, Chinese Academy of Sciences  
565 (<http://159.226.158.89:38817/thredds/catalog/Ggd/catalog.html>). We thank the  
566 anonymous reviewers for commenting on the early draft of the paper.

## 567 **Reference**

568 Asbjørnsen, H., Årthun, M., Skagseth, Ø., and T. Eldevik (2019), Mechanisms of  
569 ocean heat anomalies in the Norwegian Sea, *Journal of Geophysical Research: Oceans*,  
570 124, 2908–2923, doi.org/10.1029/2018JC014649.

571 Beardsley, R. C., R. Limeburner, K. Kim, and J. Candela (1992), Lagrangian flow  
572 observations in the East China, Yellow and Japan Seas, *La Mer*, 30, 297–314.

573 Behringer, D. (2007), The Global Ocean Data Assimilation System (GODAS) at  
574 NCEP, 87th AMS Annual Meeting.

575 Benthuisen, J., M. Feng, and L. Zhong (2014), Spatial patterns of warming off  
576 Western Australia during the 2011 Ningaloo Niño: quantifying impacts of remote  
577 and local forcing, *Continental Shelf Research*, 91, 232–246.

578 Benthuisen, J. A., E. C. J. Oliver, M. Feng, and A. G. Marshall (2018), Extreme  
579 marine warming across tropical Australia during austral summer 2015-16, *Journal of*  
580 *Geophysical Research: Oceans*, 123, 1301–1326.

581 Bond, N. A., M. F. Cronin, H. Freeland, and N. Mantua (2015), Causes and impacts  
582 of the 2014 warm anomaly in the NE Pacific, *Geophysical Research Letters*, 42,  
583 3414–3420.

584 Cai, R., H. Tan, and Q. Qi (2016), Impacts of and adaptation to inter-decadal marine  
585 climate change in coastal China seas, *International Journal of Climatology*, 36(11),  
586 3770–3780.

587 Cai, R., H. Tan, and H. Kontoyiannis (2017), Robust surface warming in offshore  
588 China seas and its relationship to the east Asian monsoon wind field and ocean  
589 forcing on interdecadal time scales, *Journal of Climate*, 30(22), 8987–9005.

590 Cai W. J., X. Hu, W. J. Huang, M. C. Murrell, J. C. Lehrter, S. E. Lohrenz, W. C.  
591 Chou, W. D. Zhai, J. T. Hollibaugh, Y. C. Wang, P. Z. Zhao, X. Guo, K. Gundersen  
592 K, M. H. Dai, and G. C. Gong (2011), Acidification of subsurface coastal waters  
593 enhanced by eutrophication, *Nature Geoscience*, 4(11), 766–770.

594 Caputi, N., M. Kangas, A. Denham, M. Feng, A. Pearce, Y. Hetzel, and A.  
595 Chandrapavan (2016), Management adaptation of invertebrate fisheries to an extreme  
596 marine heatwave event at a global warming hot spot, *Ecology and Evolution*, 6, 3583–  
597 3593.

598 Chen, C., H. Liu, and R. C. Beardsley (2003), An unstructured grid, finite volume,  
599 three-dimensional, primitive equations ocean model: Application to coastal ocean and  
600 estuaries, *Journal of Atmospheric & Oceanic Technology*, 20, 159–186,  
601 [doi.org/10.1175/1520-0426\(2003\)020,0159:AUGFVT.2.0.CO;2](https://doi.org/10.1175/1520-0426(2003)020<0159:AUGFVT.2.0.CO;2).

602 Chen C., R.C. Beardsley , G. Cowles, J. Qi, Z. Lai, G. Gao, D. Stuebe, Q. Xu, P. Xue,  
603 J. Ge, S. Hu, R. Ji, R. Tian, H. Huang, L. Wu,H. Lin, Y. Sun and L. Zhao (2013), An  
604 Unstructured Grid, Finite-Volume Community Ocean Model FVCOM User Manual,  
605 SMAST/UMASSD-13-0701.

606 Chen, K., G. G. Gawarkiewicz, S. J. Lentz, and J. M. Bane (2014), Diagnosing the  
607 warming of the Northeastern US Coastal Ocean in 2012: a linkage between the  
608 atmospheric jet stream variability and ocean response, *Journal of Geophysical*  
609 *Research: Oceans*, 119, 218–227.

610 Di Lorenzo, E. and N. Mantua (2016), Multi-year persistence of the 2014/15 North  
611 Pacific marine heatwave, *Nature Climate Change*, 6, 1042–1047.

612 Ding, Y. and J. C. L. Chan (2005), The East Asian summer monsoon: and overview,  
613 *Meteorology & Atmospheric physics*, 89:117-142.

614 Ding, Y., H. M. Yu, X. W. Bao, L. Kuang, C. X. Wang, and W. J. Wang (2011),  
615 Numerical study of the barotropic responses to a rapidly moving typhoon in the East  
616 China Sea, *Ocean Dynamics*, 61, 1237~1259, [doi:10.1007/s10236-011-0436-1](https://doi.org/10.1007/s10236-011-0436-1).

617 Ding, Y., X. Bao, Z. Yao, D. Song, J. Song, J. Gao, and J. Li (2018), Effect of  
618 coastal-trapped waves on the synoptic variations of the Yellow Sea Warm Current  
619 during winter, *Continental Shelf Research*, 167, 14-31.

620 Ding, Y., X. Bao, Z. Yao, C. Bi, K. Wan, M. Bao, Z. J., J. Song, and J. Gao (2019),  
621 Observational and model studies of synoptic current fluctuations in the Bohai Strait  
622 on the Chinese continental shelf, *Ocean Dynamics*, doi:10.1007/s10236-019-01247-5.

623 Du, Y., Y. Zhang, and Z. Xie (2009), Impacts of the Zonal Position of the East Asian  
624 Westerly Jet Core on Precipitation Distribution During Meiyu of China, *Acta*  
625 *Meteorologica Sinica*.

626 Fairall, C. W., E. F. Bradley, D. P. Rogers, J. B. Edson, and G. S. Young (1996), Bulk  
627 parameterization of air-sea fluxes for Tropical ocean-global atmosphere coupled–  
628 ocean atmosphere response experiment, *Journal of Geophysical Research*, 101(C2),  
629 3747–3764, doi:10.1029/95JC03205.

630 Fan, K. L. (1982): A study of water masses in Taiwan Strait. *Acta Oceanographica*  
631 *Taiwanica*, 13, 140–153.

632 Fathrio, I., S. Iizuka, A. Manda, Y.-M. Kodama, S. Ishida, Q. Moteki, H. Yamada,  
633 and Y. Tachibana (2017), Assessment of western Indian Ocean SST bias of CMIP5  
634 models, *Journal of Geophysical Research: Oceans*, 122, 3123–3140,  
635 doi:10.1002/2016JC012443.

636 Feng, M., Biastoch, A., Böning, C., Caputi, N., and G. Meyers, G (2008), Seasonal  
637 and interannual variations of upper ocean heat balance off the west coast of Australia,  
638 *Journal of Geophysical Research: Oceans*, 113, C12025, doi.org/10.1029/  
639 2008JC004908.

640 Feng, M., McPhaden, M. J., Xie, S. P., & Hafner, J. (2013). La Niña forces  
641 unprecedented Leeuwin Current warming in 2011. *Scientific reports*, 3, 1277.

642 Frölicher, T. L., E. M Fischer, and N. Gruber (2018), Marine heatwaves under global  
643 warming. *Nature* 560, 360–364, doi:10.1038/s41586-018-0383-9.

644 Gao, G. D., X. H. Wang, D. H. Song, X.W. Bao, B. S. Yin, D. Z. Yang, and Y. Ding  
645 (2018), Effects of wave-current interactions on suspended-sediment dynamics during  
646 strong wave events in JiaozhouBay, Qingdao China, *Journal of Physical*  
647 *Oceanography*, 48, 1053-1078, doi: 10.1175/JPO-D-17-0259.1.

648 Gao, Q., Y. Sun, and Q. You (2016), The northward shift of Meiyu rain belt and its  
649 possible association with rainfall intensity changes and the Pacific-Japan pattern,  
650 *Dynamics of Atmospheres and Oceans*, 76, 52–62,  
651 doi.org/10.1016/j.dynatmoce.2016.08.005.

652 Guan, B. X. and G. H. Fang (2006), Winter counter-wind currents off the southeastern  
653 China coast: A review, *Journal of Oceanography*, 62(1), 1–24.

654 Hobday, A. J., L. V. Alexander, S. E. Perkins, D. A. Smale, S. C. Straub, E. C. Oliver,  
655 E. C.,... T. Wernberg (2016), A hierarchical approach to defining marine heatwaves,  
656 *Progress in Oceanography*, 141, 227–238, doi.org/10.1016/j.pocean.2015.12.014.

657 Hristova, H. G., Ladd, C., and P. J. Stabeno (2019), Variability and Trends of the  
658 Alaska Gyre from Argo and Satellite Altimetry, *Journal of Geophysical Research:*  
659 *Oceans*, 124, 5870–5887, doi.org/10.1029/2019JC015231.

660 Hu, M. N., and C. F. Zhao (2008), Upwelling in Zhejiang coastal areas during  
661 summer detected by satellite observations, *Journal of Remote Sensing*, 12(2), 297–  
662 304.

663 Huang, Y., B. Wang, X. Li, and H. Wang (2018), Changes in the influence of the  
664 western Pacific subtropical high on Asian summer monsoon rainfall in the late 1990s,  
665 *Climate Dynamics*, 51, 443–455, doi:10.1007/s00382-017-3933-1.

666 Isobe, A. (2004), Driving mechanism of band structure of mean current over the  
667 continental shelf, *Journal of Physical Oceanography*, 34, 1839–1855.

668 Isobe, A. (2008), Recent Advances in Ocean-Circulation Research on the Yellow Sea  
669 and East China Sea Shelves, *Journal of Oceanography*, 64, 569-584.

670 Jacox, M. G. (2019), Marine heatwaves in a changing climate, *Nature*, 571, 485–  
671 487, doi: 10.1038/d41586-019-02196-1.

672 Kanamitsu, M., W. Ebisuzaki, J. Woollen, S.-K. Yang, J. J. Hnilo, M. Fiorino, and G.  
673 L. Potter (2002), NCEP–DOE AMIP-II Reanalysis (R-2), *Bulletin of the American*  
674 *Meteorological Society*, 83, 1631–1644, doi:10.1175/BAMS-83-11-1631.

675 Lee, T. I. Fukumori, and B. Tang (2004), Temperature advection: Internal versus  
676 external processes, *Journal of Physical Oceanography*, 34, 1936–1944.

677 Lee, S.-S., Y.-W. Seo, K.-J. Ha, and J.-G. Jhun (2013), Impact of the western North  
678 Pacific subtropical high on the East Asian monsoon precipitation and the Indian  
679 Ocean precipitation in the boreal summertime, *Asia-pacific Journal of Atmospheric*  
680 *Sciences*, 49, 171–182. doi:10.1007/s13143-013-0018-x.

681 Lozovatsky, I. D., Z. Liu, and H. J. S. Fernando (2007a), Tides and mixing in the  
682 northwestern East China Sea. Part I: Rotating and reversing tidal flows, *Continental*  
683 *Shelf Research*, 28(2), 318-337, doi:10.1016/j.csr.2007.08.006.

684 Lozovatsky, I. D., Z. Liu, and H. J. S. Fernando (2007b), Tides and mixing in the  
685 northwestern East China Sea, Part II: Near-bottom Turbulence, *Continental Shelf*  
686 *Research*, 28(2), 338-350, doi:10.1016/j.csr.2007.08.007.

687 Ma, C., D. X. Wu, X. Lin, J. Yang, and X. Ju (2010), An open-ocean forcing in the  
688 East China and Yellow seas, *Journal of Geophysical Research*, 115, C12056,  
689 doi:10.1029/2010JC006179.

690 Matsumura, S., S. Sugimoto, and T. Sato (2015), Recent intensification of the western  
691 Pacific subtropical high associated with the East Asian summer monsoon, *Journal of*  
692 *Climate*, 28, 2873–2883, doi:10.1175/JCLI-D-14-00569.1.

693 Mellor, G. L., and T. Yamada (1982), Development of a turbulence closure model for  
694 geophysical fluid problems, *Review of Geophysics*, 20, 851– 875.

695 Menemenlis D, Campin JM, Heimbach P, Hill C, Lee T, Nguyen A, Schodlok M,  
696 Zhang H (2008), ECCO2: high resolution global ocean and sea ice data synthesis.  
697 *Mercat. Ocean Q. News* 31:13–21.

698 Mills K. E, A. J. Pershing, C. J. Brown Curtis, Y. Chen, F.-S. Chiang, D. S., Holland  
699 Daniel, S. Lehuta, J. A. Nye, J. C. Sun, A. C., Thomas, and R. A. Wahle Richard  
700 (2012), Lessons from the 2012 ocean heatwave in the Northwest Atlantic,  
701 *Oceanography*, 26, 60–64.

702 Naimie, C. E., C. A. Blain and D. R. Lynch (2001), Seasonal mean circulation in the  
703 Yellow Sea-a model-generated climatology, *Continental Shelf Research*, 21, 667-695.

704 Ninomiya, K. (2004), Large- and mesoscale features of Meiyu-Baiu front associated  
705 with intense rainfalls. pp. 404–435. doi:10.1142/9789812701411\_0011.

706 Oey, L.-Y., M.-C. Chang, Y.-L. Chang, Y.-C. Lin, and F.-H. Xu (2013), Decadal  
707 warming of coastal China Seas and coupling with winter monsoon and currents,  
708 *Geophysical Research Letters*, 40, 6288–6292, doi:10.1002/2013GL058202.

709 Olita, A., R. Sorgente, A. Ribotti, S. Natale, and S. Gaberšek (2006), Effects of the  
710 2003 European heatwave on the Central Mediterranean Sea surface layer: a numerical  
711 simulation, *Ocean Science*, 3, 85–125.

712 Oliver, E. C. J., J. A. Benthuisen, N. L. Bindoff, A. J. Hobday, N. J. Holbrook, C. N.  
713 Munday, and S. E. Perkins-Kirkpatrick (2017), The unprecedented 2015/16 Tasman  
714 Sea marine heatwave, *Nature Communication*, 8, 16101.

715 Oliver, E. C. J., M. G. Donat, M. T. Burrows, P. J. Moore, D. A. Smale, L. V.  
716 Alexander, J. A. Benthuisen, M. Feng, A. Sen Gupta, A. J. Hobday, N. J. Holbrook, S.  
717 E. Perkins-Kirkpatrick, H. A. Scannell, S. C. Straub, and T. Wernberg (2018), Longer

718 and more frequent marine heatwaves over the past century, *Nature Communications*,  
719 9, doi:10.1038/s41467-018-03732-9.

720 Oliver, E. C. J. (2019), Mean warming not variability drives marine heatwave trends,  
721 *Climate Dynamics*, doi:10.1007/s00382-019-04707-2.

722 Oppenheim, A. V, R. W. Schafer, and J. R. Buck (1999), *Discrete-time Signal*  
723 *Processing* (2Nd Ed.). Prentice-Hall, Inc., Upper Saddle River, NJ, USA.

724 Park C., and C., S. D. Schubert (1994), On the Nature of the 1994 East Asian Summer  
725 Drought, *Journal of Climate*, 10, 1056-1070.

726 Park, S., and P. C. Chu (2007), Synoptic distributions of thermal surface mixed layer  
727 and thermocline in the southern Yellow and East China Seas, *Journal of*  
728 *Oceanography*, 63, 1021–1028.

729 Park, K.A., E. Y. Lee, E. Chang, and S. Hong (2015), Spatial and temporal variability  
730 of sea surface temperature and warming trends in the Yellow Sea, *Journal of Marine*  
731 *Systems*, 143, 24–38.

732 Paulson, C. A., and J. J. Simpson (1977), Irradiance measurements in the upper ocean,  
733 *Journal of Physical Oceanography*, 7, 952–956.

734 Reynolds, R. W., T. M. Smith, C. Liu, D. B. Chelton, K. S., Casey, and M. G. Schlax  
735 (2007), Daily high-resolution-blended analyses for sea surface temperature, *Journal of*  
736 *Climate*, 20(22), 5473–5496, doi:/10.1175/2007JCLI1824.1.

737 Saha, S., S. Moorthi, X. Wu, J. Wang, S. Nadiga, P. Tripp, D. Behringer, Y.-T. Hou,  
738 H. Chuang, M. Ek Iredell, J. Meng, R. Yang, M. P. Mendez, H. van den Dool, Q.  
739 Zhang, W. Wang, M. Chen, and E. Becker (2013), The NCEP Climate Forecast  
740 System Version 2, *Journal of Climate*, 27, 2185–2208.  
741 doi:10.1175/JCLI-D-12-00823.1

742 Saha, S., and coauthors (2010a), The NCEP Climate Forecast System Reanalysis,  
743 *Bulletin of the American Meteorological Society*, 91, 1015–1058.

744 Saha, S., and coauthors (2010b), NCEP Climate Forecast System Reanalysis (CFSR)  
745 Monthly Products, January 1979 to December 2010.

746 Schlegel R.W., E. C. J. Oliver, S. Perkins-Kirkpatrick, A. Kruger and A. J. Smit  
747 (2017), Predominant Atmospheric and Oceanic Patterns during Coastal Marine  
748 Heatwaves, *Frontier Marine Science*, 4:323, doi: 10.3389/fmars.2017.00323.

749 Smagorinsky, J. (1963), General circulation experiments with the primitive equations,  
750 I, The basic experiment, *Monthly Weather Review*, 91: 99~164.

751 Sparnocchia, S., M. E. Schiano, P. Picco, R. Bozzano, and A. Cappelletti (2006), The  
752 anomalous warming of summer 2003 in the surface layer of the Central Ligurian Sea  
753 (Western Mediterranean), *Annales Geophysicae*, 24, 443–452.

754 Tan. H., and R. Cai (2018), What caused the record-breaking warming in East China  
755 Seas during August 2016 ?, *Atmospheric Sciences Letters*, 19, e853,  
756 doi:10.1002/asl.853.

757 US Naval Oceanographic Office and the US Naval Ocean Research and Development  
758 Activity (1983) DBDB5 (Digital Bathymetric Data Base-5 Minute Grid). US N.O.O.,  
759 Bay St. Louis, p 329.

760 Xia, C., F. Qiao, Y. Yang, J. Ma, and Y. Yuan (2006), Three-dimensional structure of  
761 the summertime circulation in the Yellow Sea from a wave-tide-circulation coupled  
762 model, *Journal of Geophysical Research*, 111, C11S03, doi:10.1029/2005JC003218.

763 Xie, S., J. Hafner, Y. Tanimoto, W. T. Liu, H. Tokinaga, and H. Xu (2002),  
764 Bathymetric effect on the winter sea surface temperature and climate of the Yellow  
765 and East China Seas, *Geophysical Research Letters*, 29(24), 2228,  
766 doi:10.1029/2002GL015884, 2002.

767 Yeh S.-W. and C.-H Kim (2010), Recent warming in the Yellow/East China Sea  
768 during winter and the associated atmospheric circulation, *Continental Shelf Research*,  
769 30, 1428-1434.

770 Wang, B., B. Xiang, and J.-Y. Lee (2013), Subtropical High predictability establishes  
771 a promising way for monsoon and tropical storm predictions, *Proceedings of the*  
772 *National Academy of Sciences of the United States of America*, 110, 2718 LP-2722.  
773 doi:10.1073/pnas.1214626110

774 Wang, J., and L.-Y. Oey (2014), Inter-annual and decadal fluctuations of the Kuroshio  
775 in East China Sea and connection with surface fluxes of momentum and heat,  
776 *Geophysical Research Letters*, 41, 8538–8546, doi:10.1002/2014GL062118.

777 Wang, S., and H. Zuo (2016), Effect of the East Asian Westerly Jet’s Intensity on  
778 Summer Rainfall in the Yangtze River Valley and Its Mechanism, *Journal of Climate*,  
779 29, 2395–2406. doi:10.1175/JCLI-D-15-0259.1

780 Xuan, S., Q. Zhang, and S. Sun (2011), Anomalous midsummer rainfall in Yangtze  
781 River-Huaihe River valleys and its association with the East Asia westerly jet,  
782 *Advances in Atmospheric Science*, 28, 387–397, doi:10.1007/s00376-010-0111-3.

783 Xuan, J. L., D. J. Huang, F. Zhou, X. Zhu, and X. P. Fan (2012), The role of wind on  
784 the detachment of low salinity water in the Changjiang Estuary in summer, *Journal of*  
785 *Geophysical Research: Oceans*, 117, C10004, doi:10.1029/2012JC008121.

786 Yanagi, T. and S. Takahashi (1993): Seasonal variation of circulations in the East  
787 China Sea and the Yellow Sea. *Journal of the Oceanographic Society of Japan*, 49,  
788 491–501.

789 Yang, D. Z., R. X. Huang, B. S., Yin, X. R., H. Y. Chen, J. F. Qi, ...Benthuisen, J.-A.  
790 (2018). Topographic beta spiral and onshore intrusion of the Kuroshio Current.  
791 *Geophysical Research Letters*, 45, 287–296, doi.org/10.1002/2017GL076614.

792 Yang, J. (2007), An oceanic current against the wind: How does Taiwan Island steer  
793 warm water into the East China Sea, *Journal of Physical Oceanography*, 37, 2563–  
794 2569, doi:10.1175/JPO3134.1.

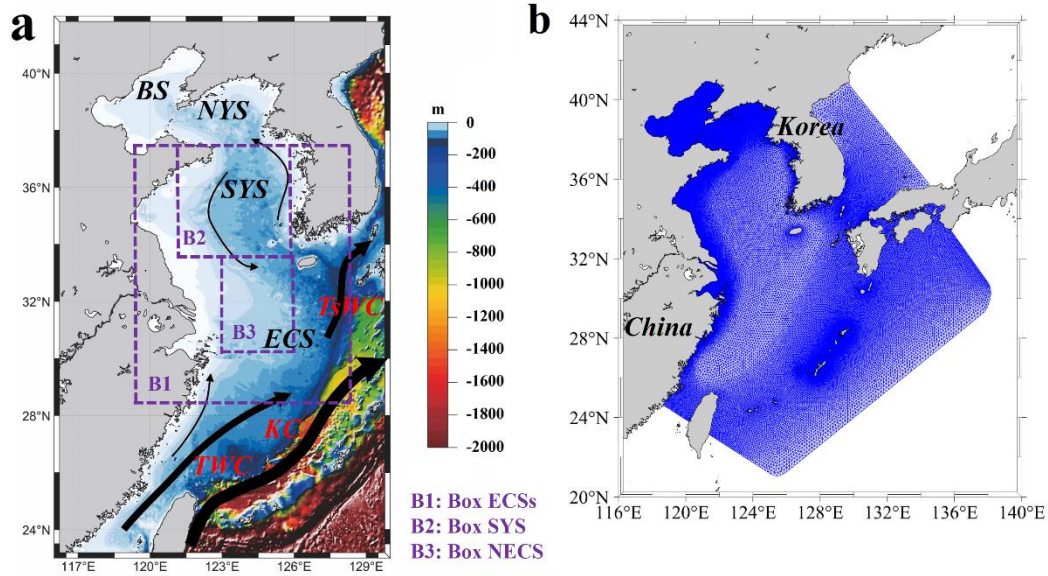
795 Zhang, Y., Feng, M., Du, Y., Phillips, H. E., Bindoff, N. L., & McPhaden, M. J.  
796 (2018), Strengthened Indonesian Throughflow drives decadal warming in the  
797 Southern Indian Ocean, *Geophysical Research Letters*, 45, 6167–6175,  
798 doi.org/10.1029/2018GL078265.

799 Zhou, T., D. Gong, J. Li, and B. Li (2009), Detecting and understanding the  
800 multi-decadal variability of the East Asian Summer Monsoon Recent progress and  
801 state of affairs, *Meteorologische Zeitschrift*, 18, 455–467,  
802 doi:10.1127/0941-2948/2009/0396.

803 Zheng P., D. Wu, and X. Lin (2009), the relationship between the Taiwan Warm  
804 Current and Tsushima Warm Current, *Journal of hydrodynamics*, 2009,21(2):212-218,  
805 doi: 10.1016/S1001-6058(08)60138-9.

806

807



808

809 **Figure 1.** (a) Map of the Bohai Sea (BS), North Yellow Sea (NYS), South Yellow  
 810 Sea (SYS) and East China Sea (ECS), with topography and main current patterns. (b)  
 811 The FVCOM-ECSs model domain and mesh grid used in this study. TsWC, TWC and  
 812 KC represent Tsushima Warm Current, Taiwan Warm Current and Kuroshio Current,  
 813 respectively. Boxes ECSs (119-126.5°E, 28.75-36.65°N), SYS (121-125.9°E,  
 814 33.65-37.4°N) and NECS (123-126°E, 30-33.65°N) are indicated in (a) with purple  
 815 dashed lines, which are the domain where the MHWs are discussed in this study.

816

817

818

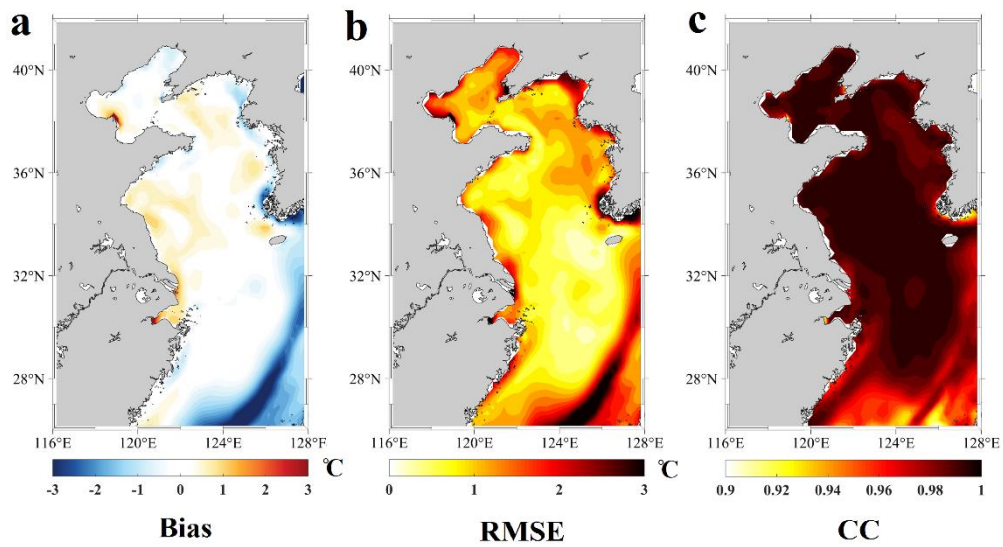
819

820

821

822

823



824

825 **Figure 2.** Statistical comparison between the FVCOM-ECSs modeled and satellite  
 826 SST on monthly time scale from January 2013 to August 2018: (a) mean bias (model  
 827 - satellite); (b) root mean square error and (c) correlation coefficient. The  
 828 FVCOM-ECSs outputs were first interpolated onto the NOAA OISST grid before the  
 829 mean bias, RMSE (Root Mean Square Error) and correlation coefficients between  
 830 satellite and the FVCOM-ECSs SST were computed. The FVCOM-ECSs SST was  
 831 taken from the temperature output from the first sigma layer.

832

833

834

835

836

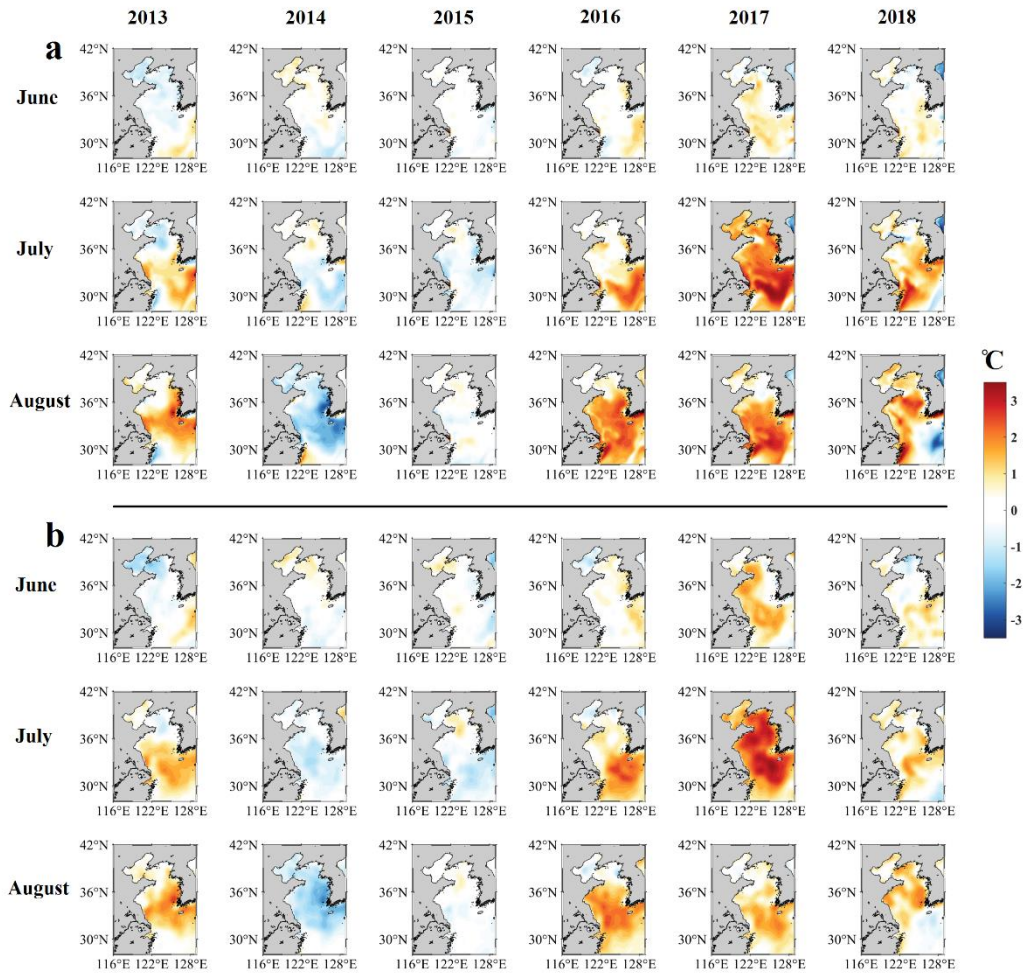
837

838

839

840

841



842

843 **Figure 3.** (a) The FVCOM-ECSs modeled and (b) satellite (monthly-mean) SST

844 anomalies in the ECSs in June, July and August during 2013-2018.

845

846

847

848

849

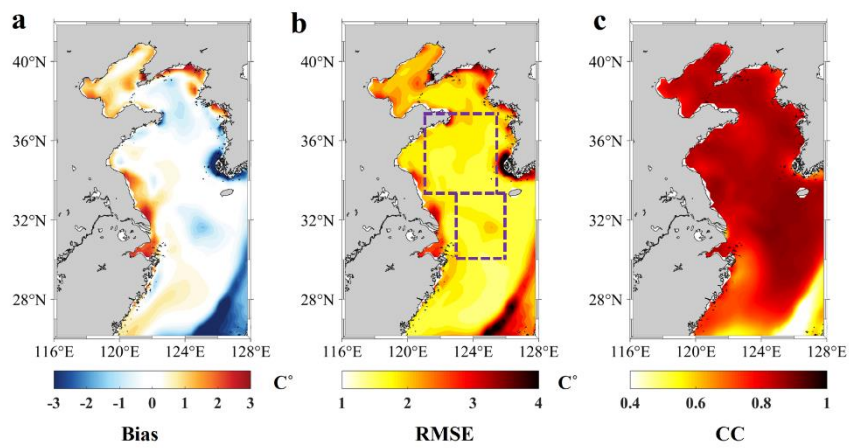
850

851

852

853

854



855

856 **Figure 4.** Statistical comparison between the FVCOM-ECSs modeled and satellite  
857 SST on daily time scale in JJA from 2013 to 2018: (a) mean bias (model - satellite);  
858 (b) root mean square error and (c) correlation coefficient.

859

860

861

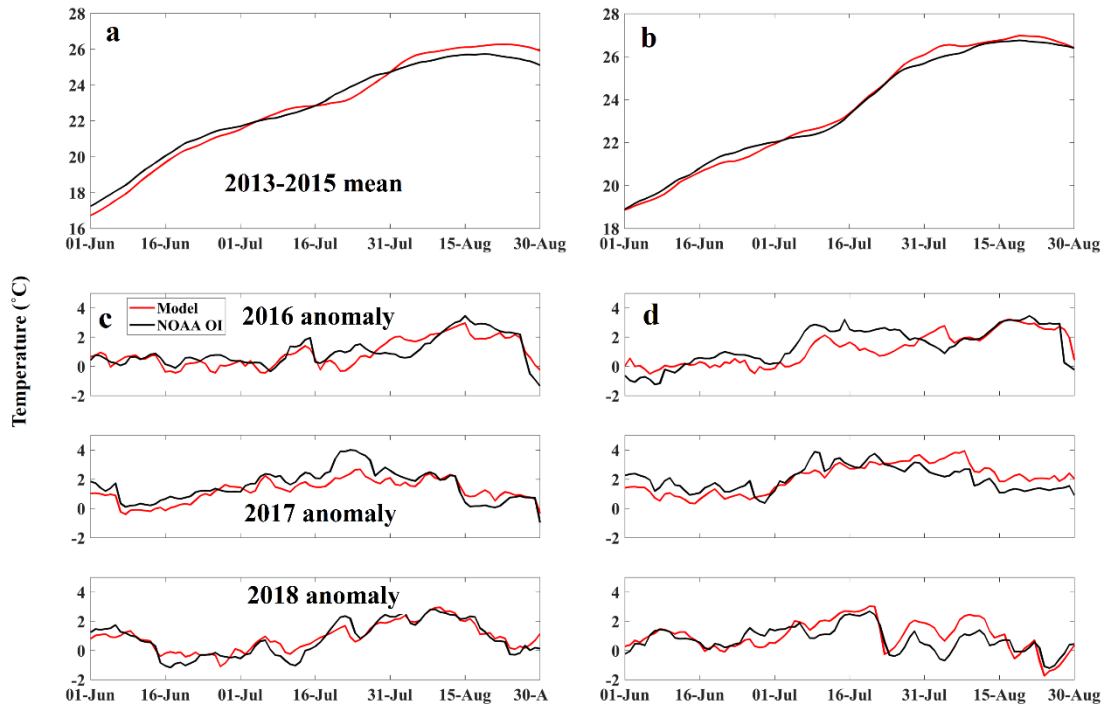
862

863

864

865

866



867

868 **Figure 5.** Comparison of normal-year (2013-2015) averaged and anomalous

869 (2016-2018) SST during JJA for Boxes SYS (a,c) and NECS (b,d).

870

871

872

873

874

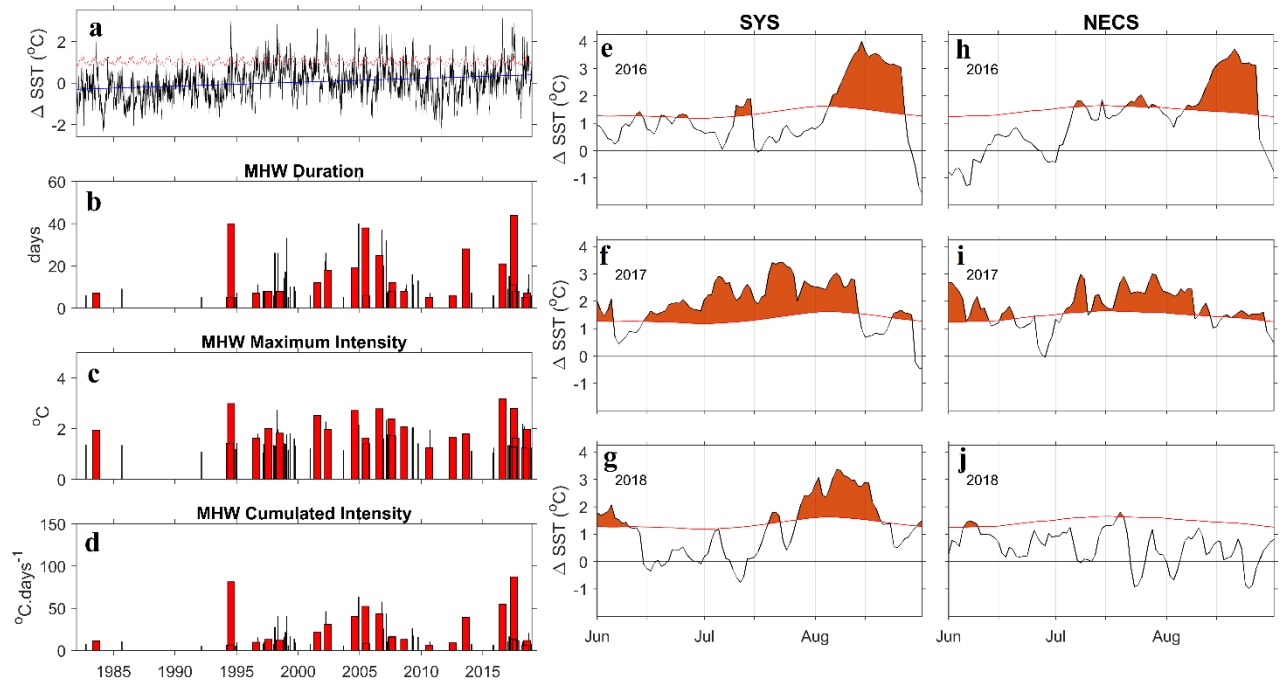
875

876

877

878

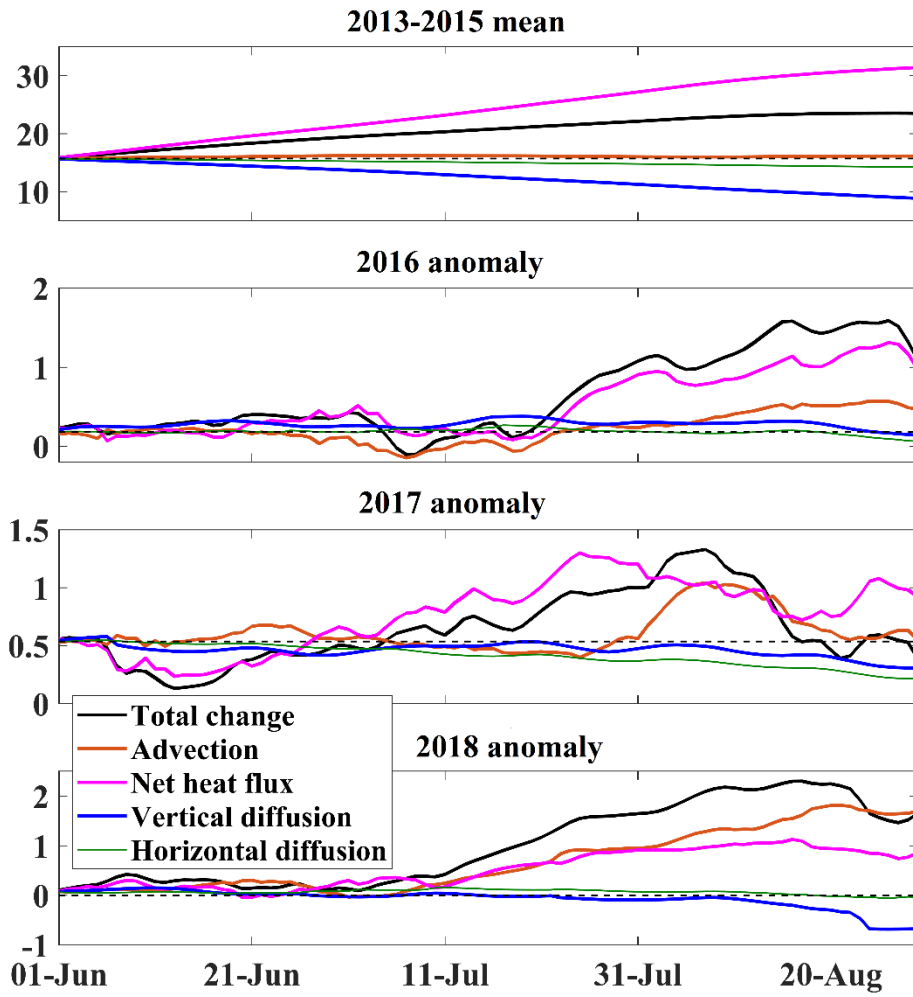
879



880

881 **Figure 6.** SST and MHW characteristics in the ECSs. (a) Time series of SST anomalies relative to the 1982-2016 climatology. The red and blue  
 882 lines denote the MHW threshold and a linear trend, respectively. (b) MHW duration (c) maximum intensity and (d) Cumulated intensity during  
 883 1982-2018. MHWs occurring in summer (June-August) were plotted in red. (e-j) Zoomed-in SST anomalies during the (top) 2016, (middle) 2017,

884 and (bottom) 2018 summer averaged in the (e-g) SYS and (h-j) NECS box, respectively (Figure 1a). MHW threshold (orange line) and SST  
885 anomalies exceeding the MHW threshold value (shading) were denoted.



886

887 **Figure 7.** (a) Normal-year averages (2013-2015) and (b-d) anomalies (2016-2018) of  
 888 temperature at the top 20 m for Box SYS in JJA caused by individual terms. Thin  
 889 dash black lines indicate the temperature in (a) or temperature anomalies in (b) on  
 890 July 1st.

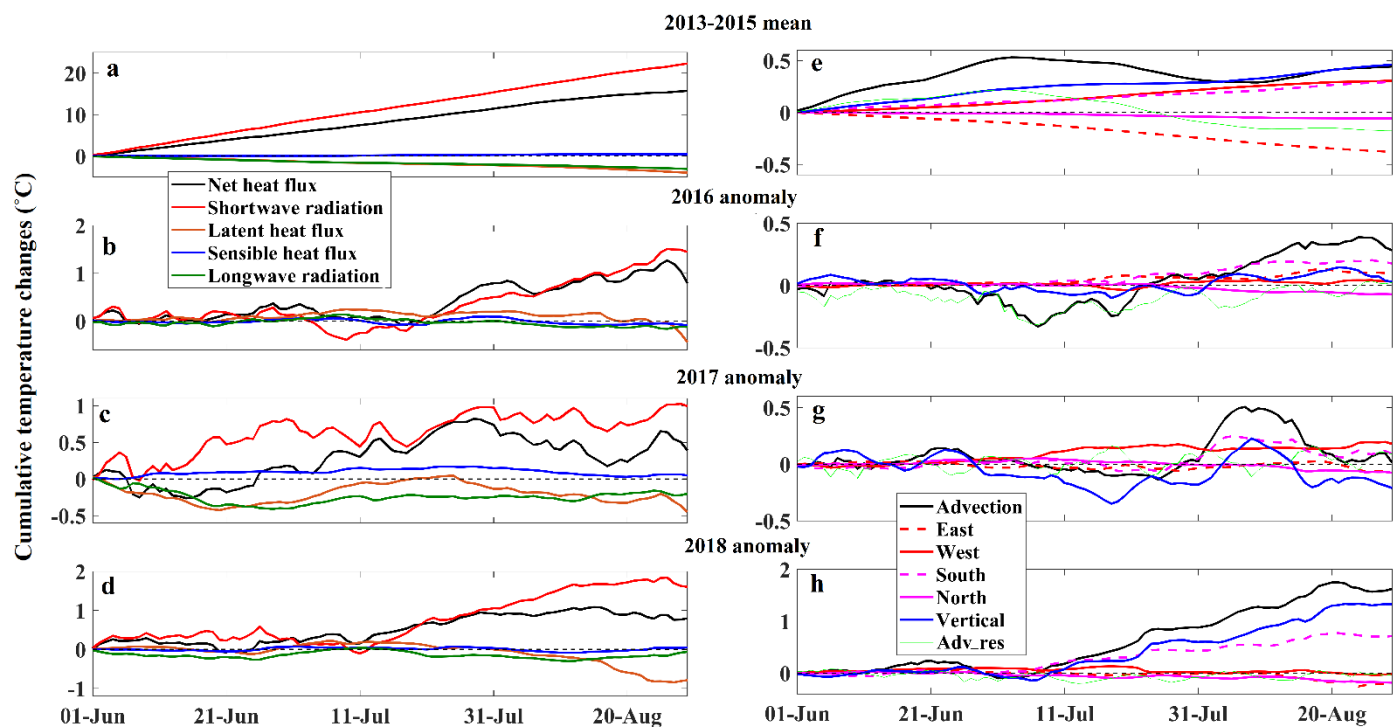
891

892

893

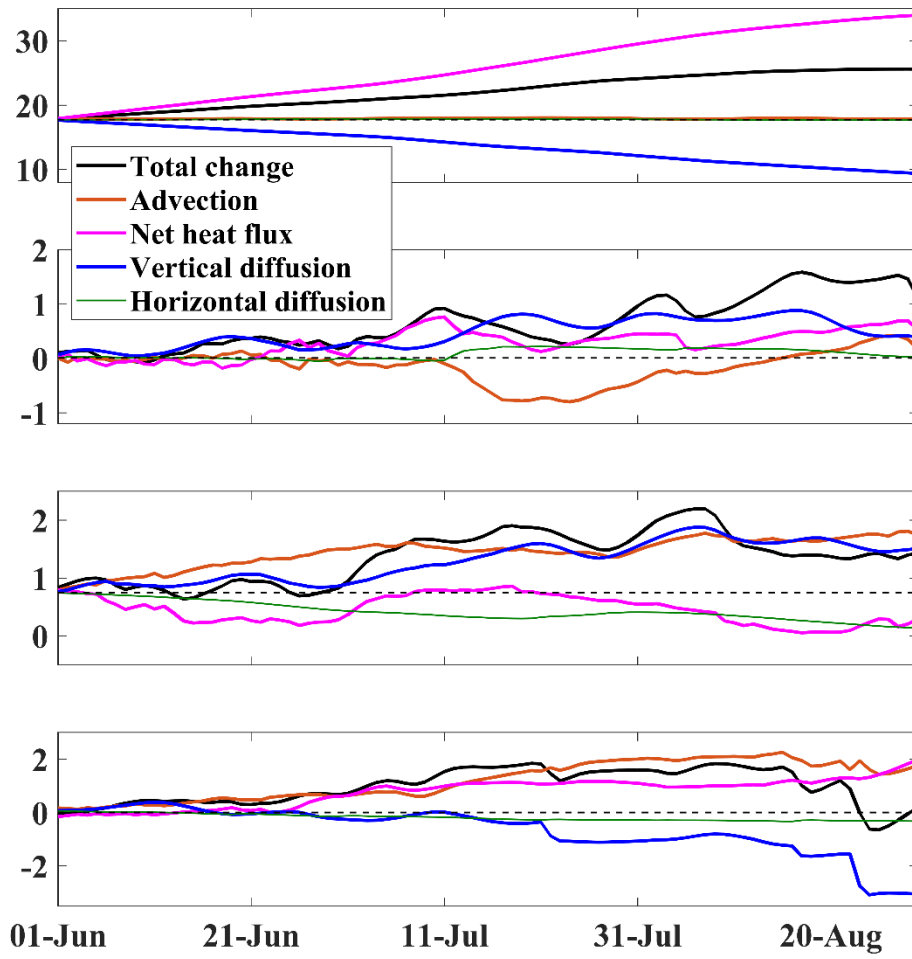
894

895



896

897 **Figure 8.** (a) Normal-year averages (2013-2015) and (b-d) anomalies (2016 -2018) of cumulative temperature changes from June 1st at the top  
 898 20 m for Box SYS in JJA caused by each heat flux terms. (e) Normal-year averages and (f-h) anomalies of cumulative temperature changes from  
 899 June 1st at the top 20 m for Box SYS caused by advection at various boundaries. Thin dash black lines indicates 0°C.



900

901 **Figure 9.** As in Figure 7 but for Box NECS.

902

903

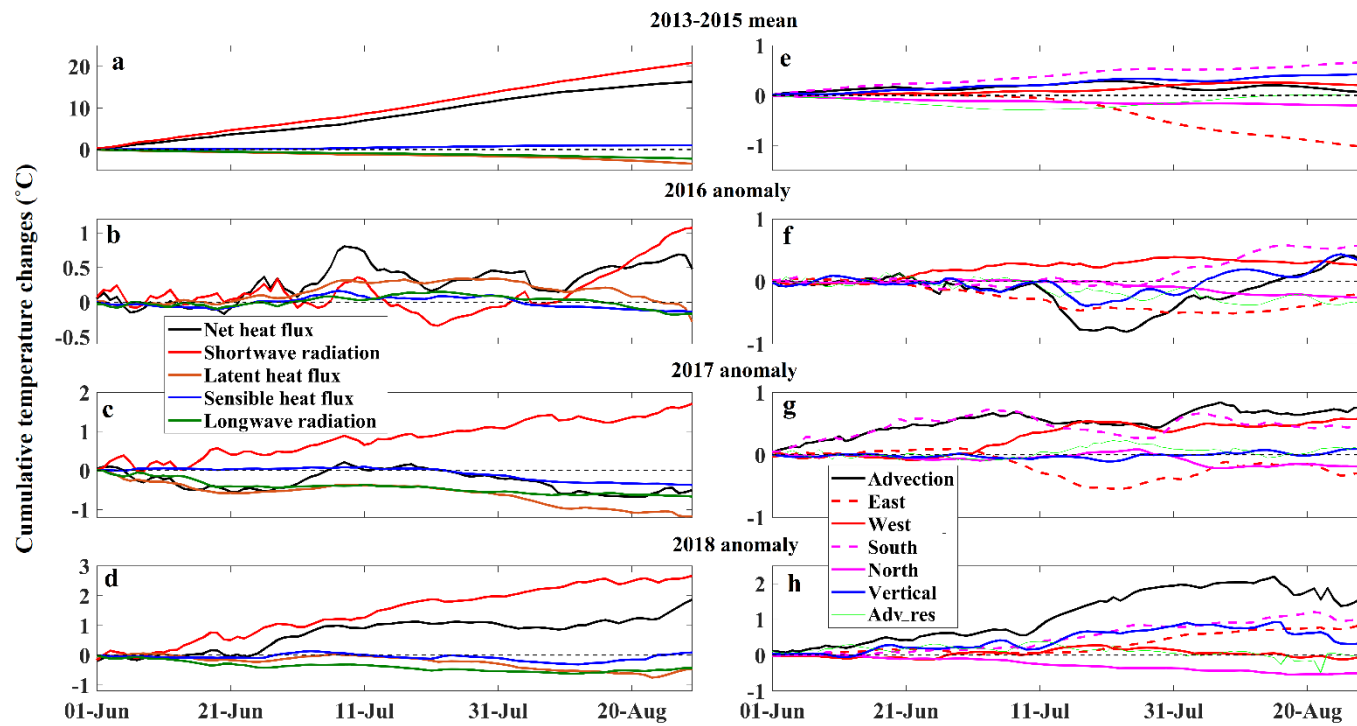
904

905

906

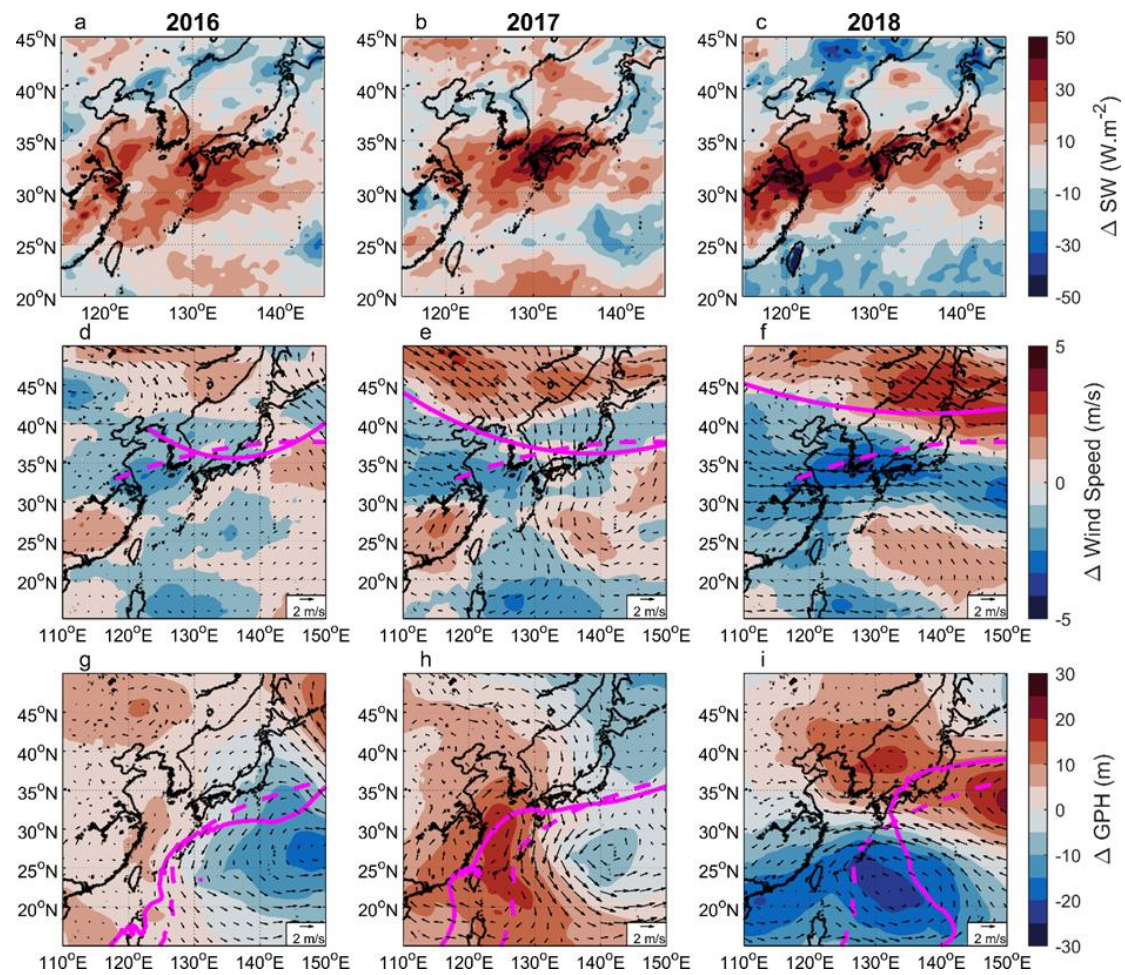
907

908



909

910 **Figure 10.** As in Figure 8 but for Box NECS.



911

912 **Figure 11.** Drivers of shortwave radiation anomalies. (a-c) Surface shortwave radiation anomalies averaged during the 2016-2018  
 913 summers (JJA). (d-f) 500hPa wind speed (shading) and wind direction (vectors) anomalies. The climatological (dashed) and  
 914 averaged (solid) position of the 500hPa Jet is plotted in magenta. (g-i) 850hPa geopotential height (shading) and wind (vectors)  
 915 anomalies. The climatological (dashed) and averaged (solid) position of the 1490 geopotential height contour is plotted in magenta.  
 916 The 2013-2015 normal years JJA averages were defined as the climatology.

917

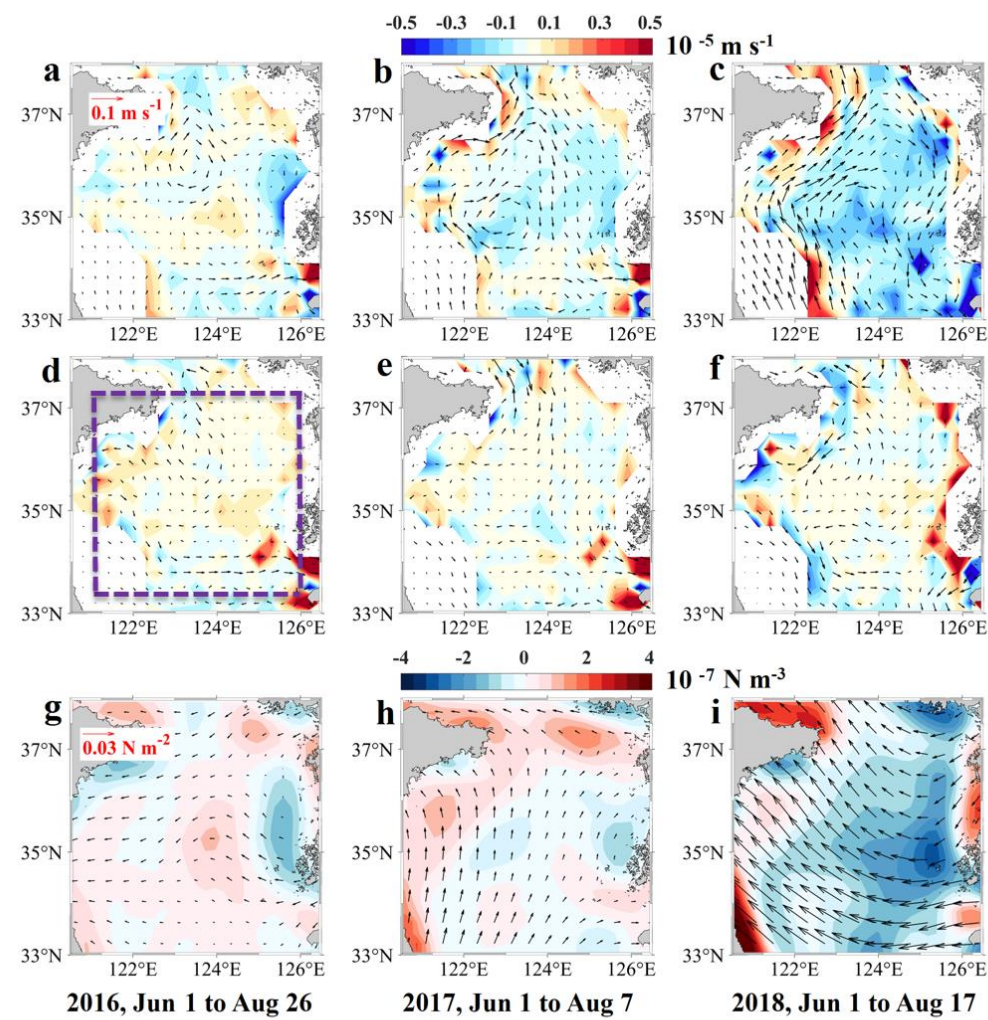
918

919

920

921

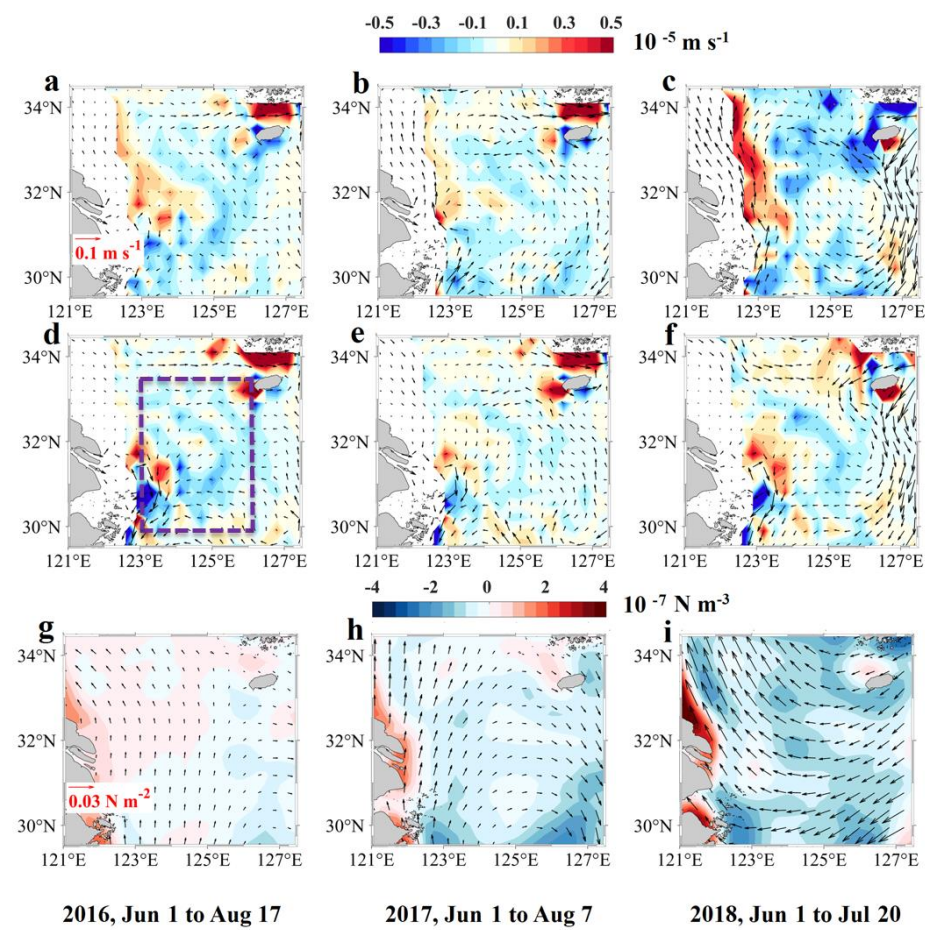
922



924

925 **Figure 12.** (a-c) Anomalies of horizontal (vectors) and vertical (contour) currents averaged during periods from June 1<sup>st</sup> to the  
 926 day of maximum temperature anomalies of JJA in each year (2016-2018) for Box SYS. (d-f) As in (a-c) but for the simulation  
 927 driven by averaged winds during normal years (2013-2015). (g-i) Anomalies of wind stress (vectors) and stress curl (contour)  
 928 averaged during corresponding periods in (a-c). The horizontal currents are averaged for the top 20 m and the vertical currents  
 929 are at 20 m.

930

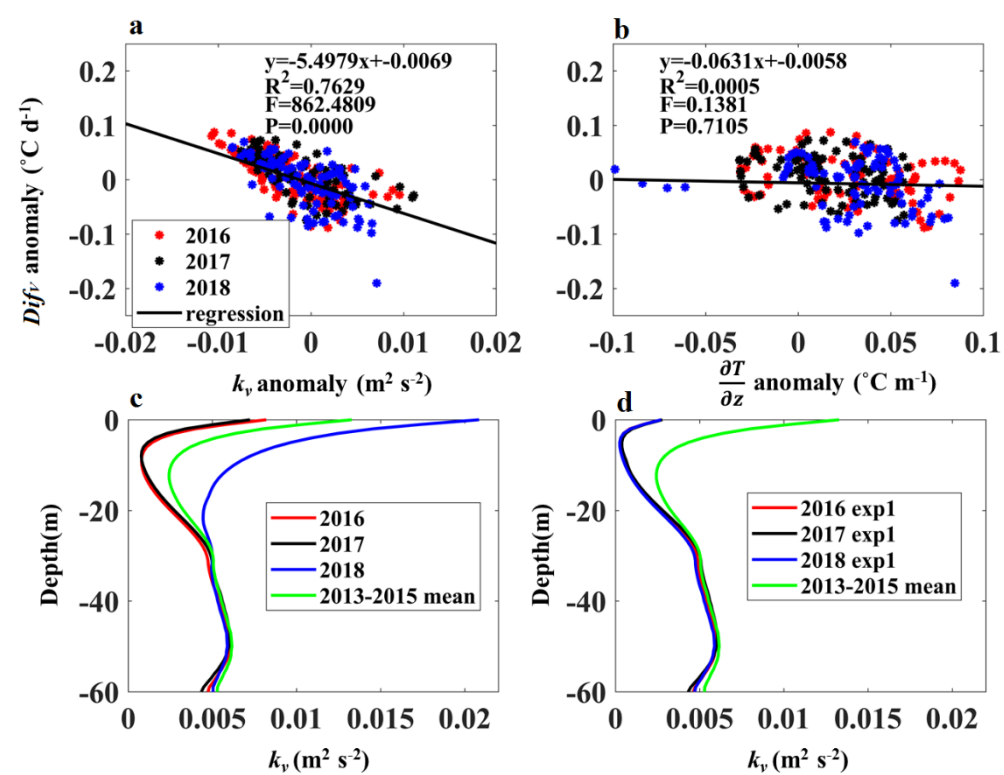


932

933 **Figure 13.** As in Figure 12 but for Box NECS

934

935



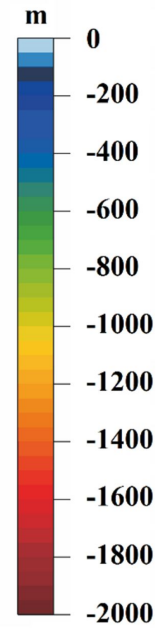
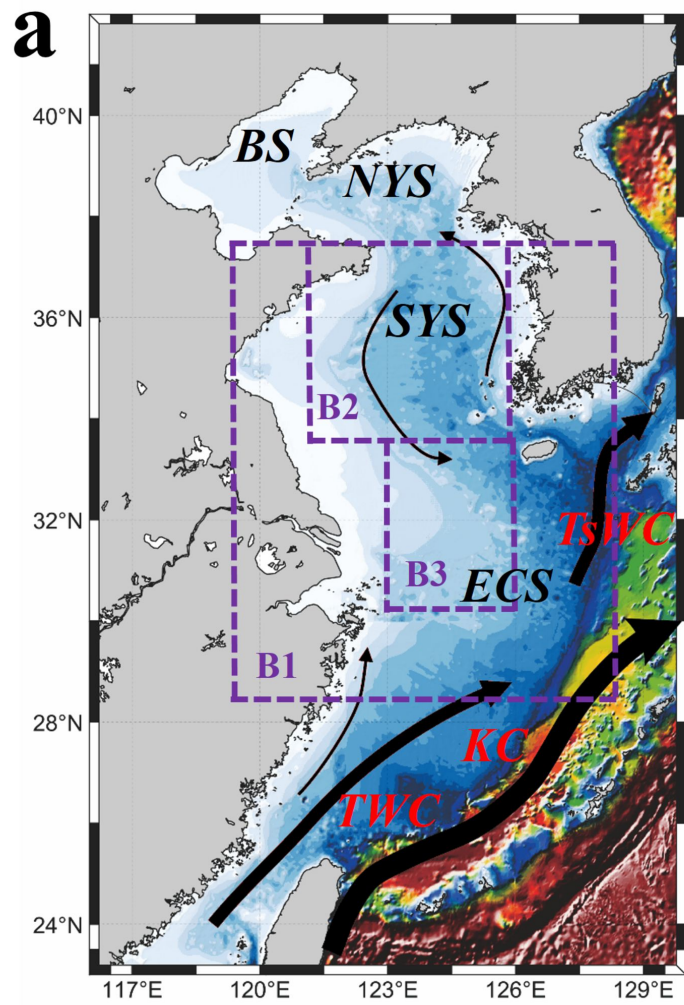
936

937 **Figure 14.** Anomalies (2016 to 2018) of daily temperature changes due to vertical mixing are plotted against the anomalies of  
 938 daily-averaged (a) vertical eddy viscosities and (b) vertical temperature gradients at 20 m in Box NECS. (c) Vertical profile of  
 939 JJA-mean vertical eddy viscosities in Box NECS. (d) As in (c) but for experiment 1. 2013-2015 mean vertical eddy viscosities in (d)  
 940 were same as that in (c). The corresponding statistical estimators are also given in (a) and (b).

941

942

Figure 1.



**B1: Box ECSs**  
**B2: Box SYS**  
**B3: Box NECS**

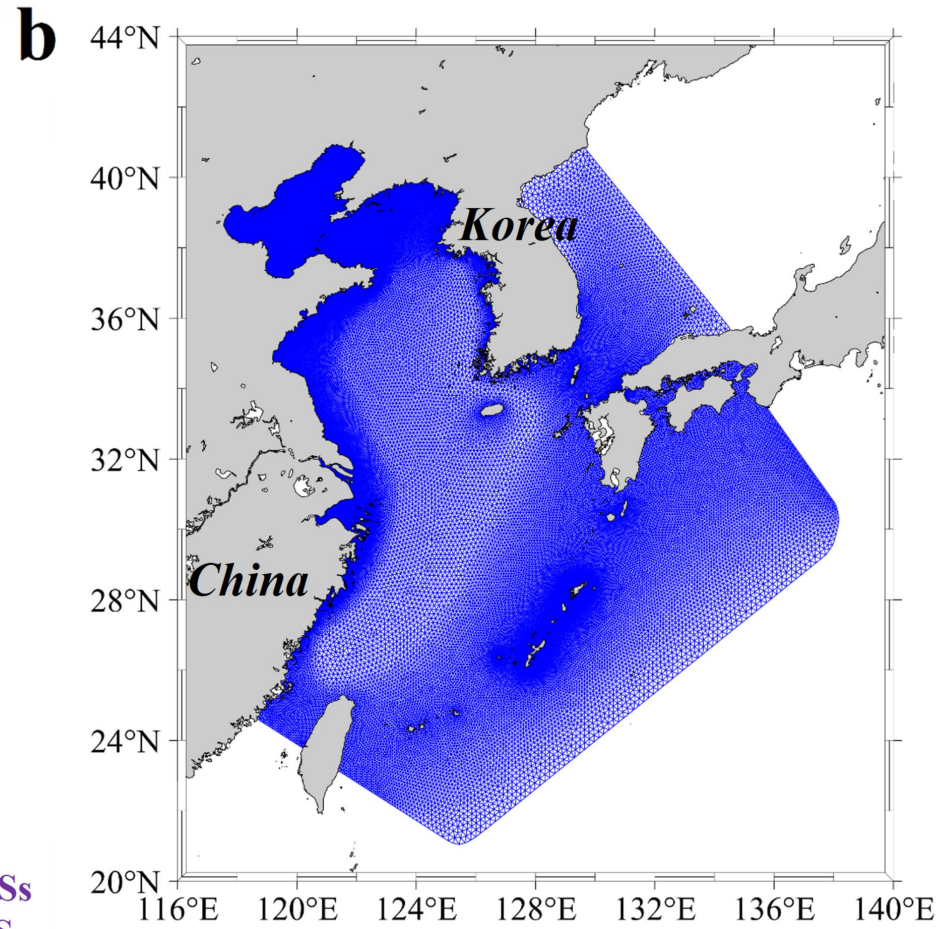
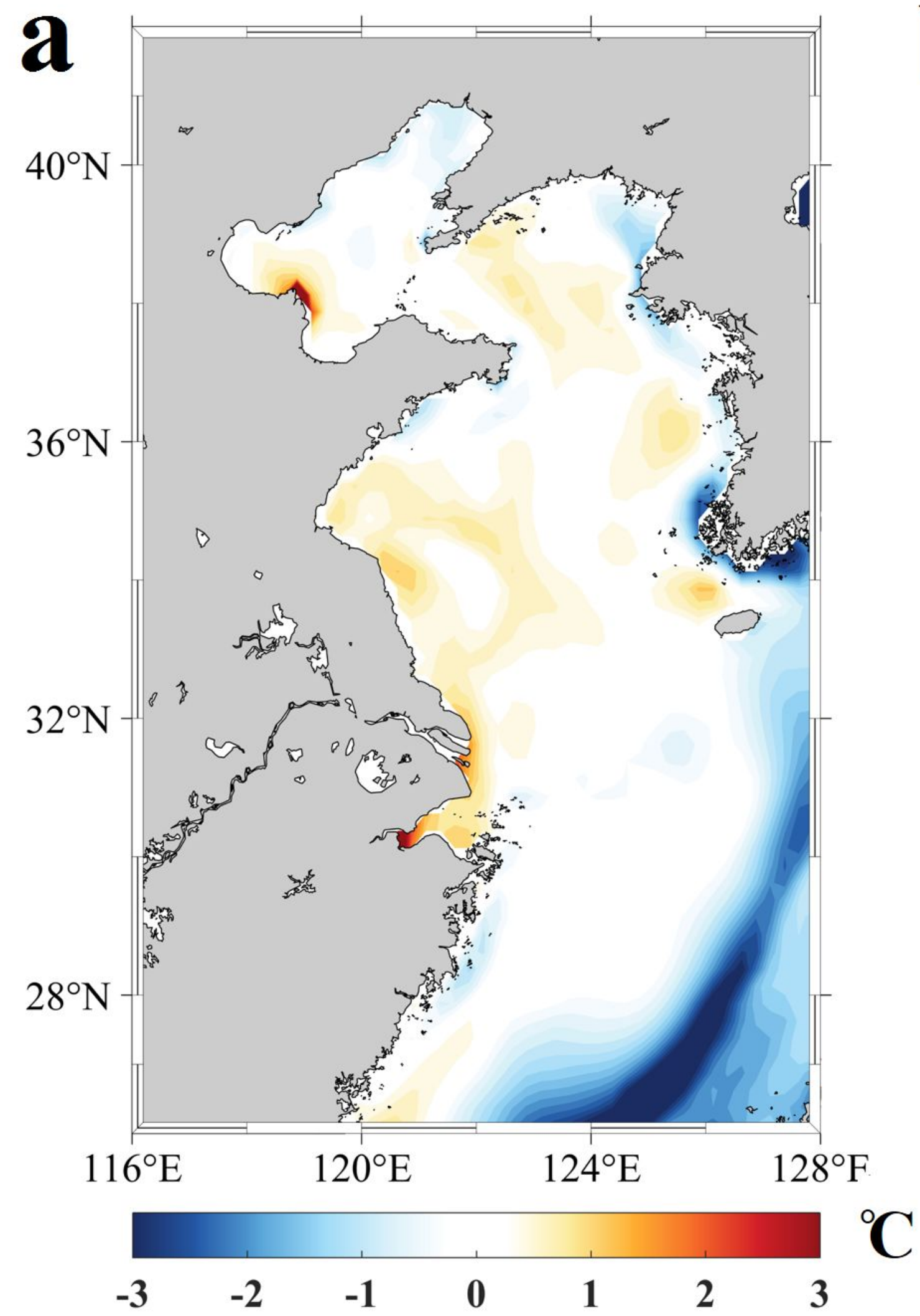
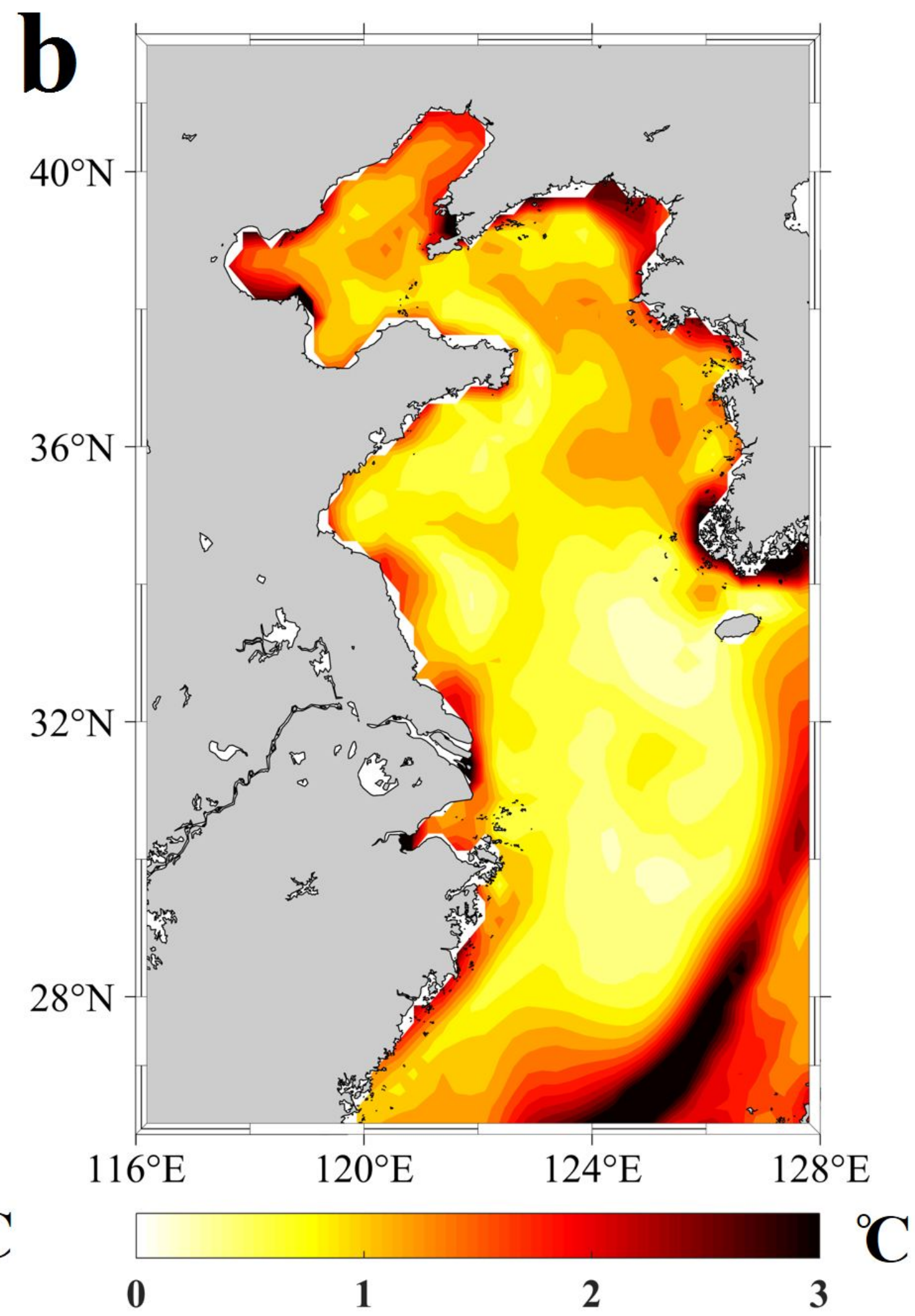


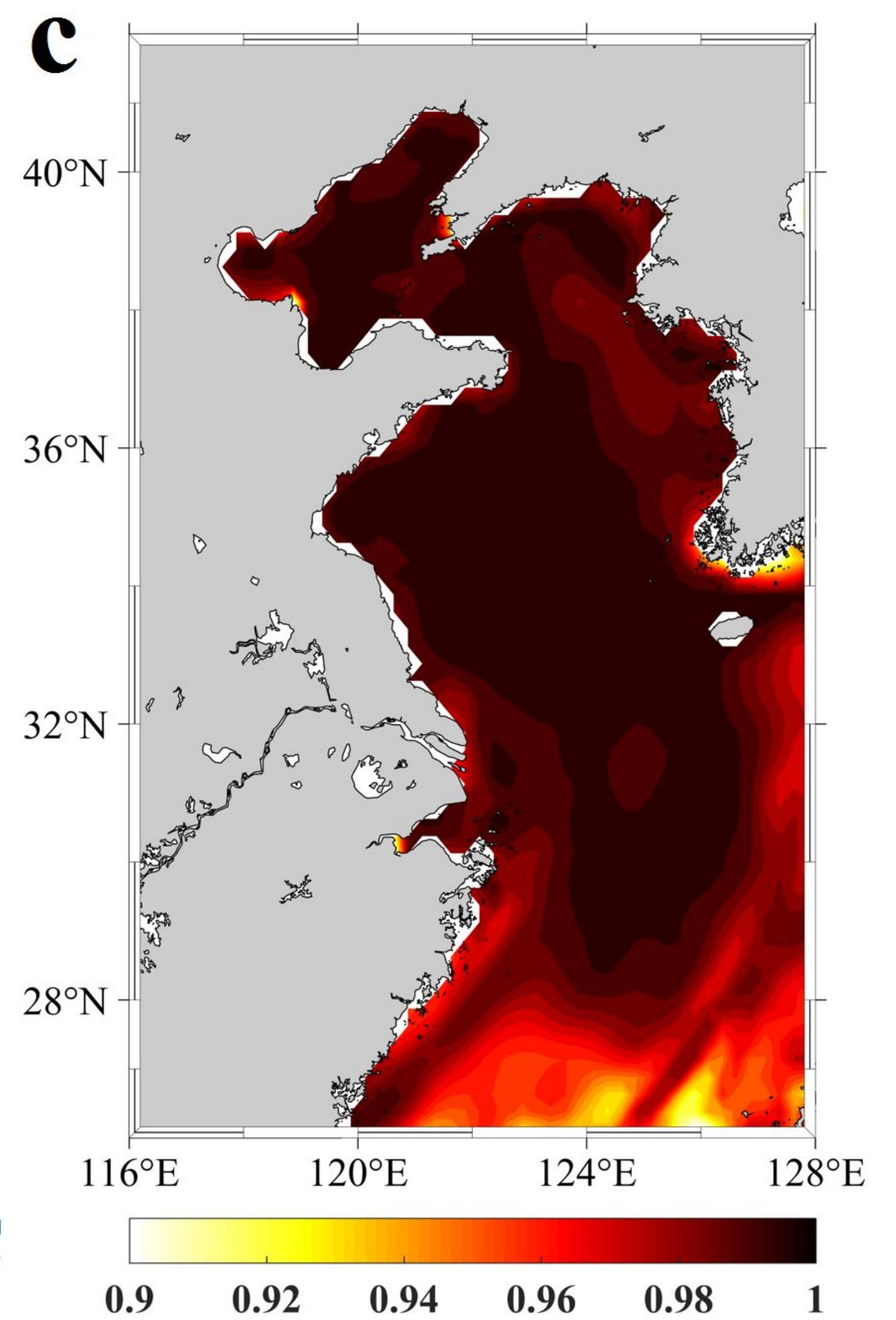
Figure 2.



**Bias**

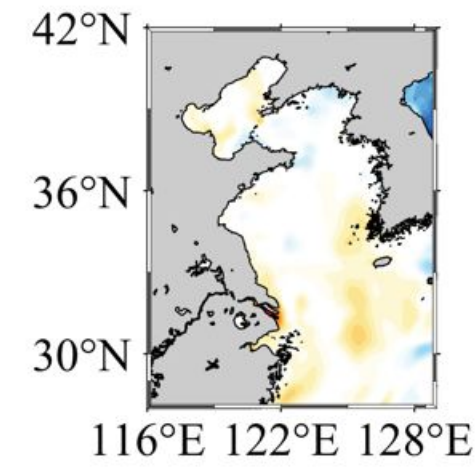
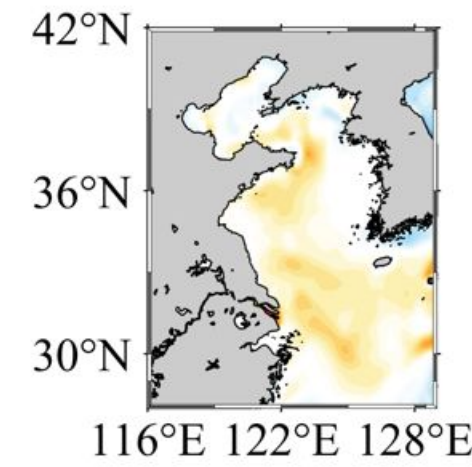
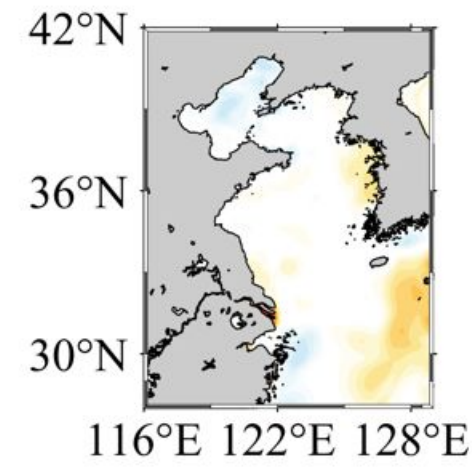
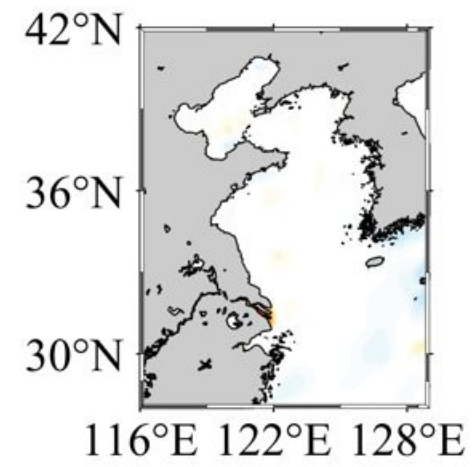
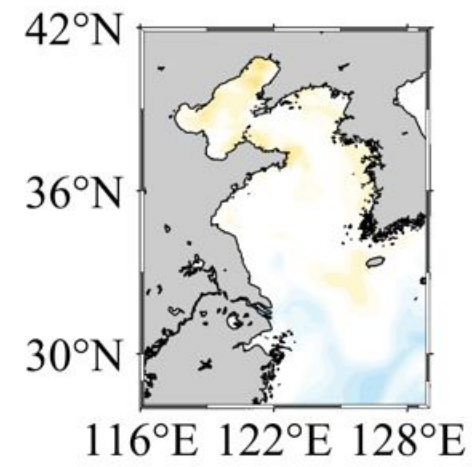
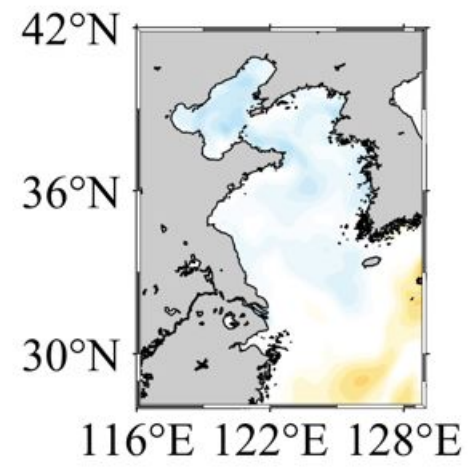
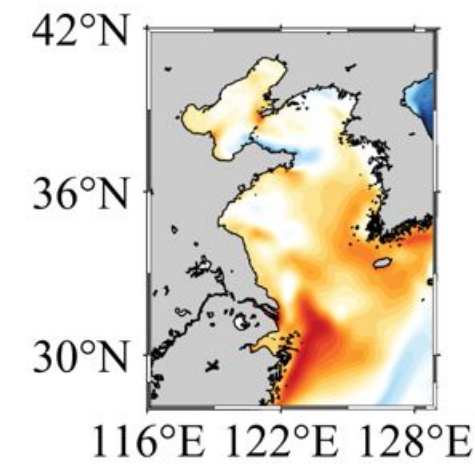
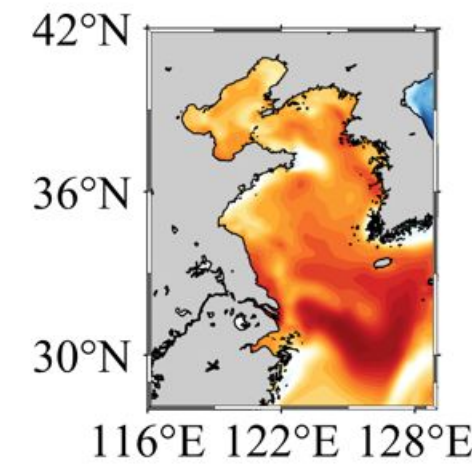
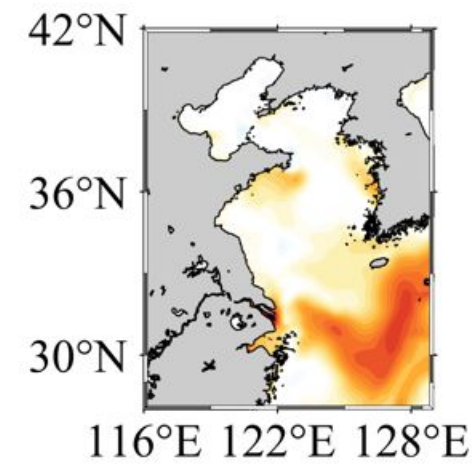
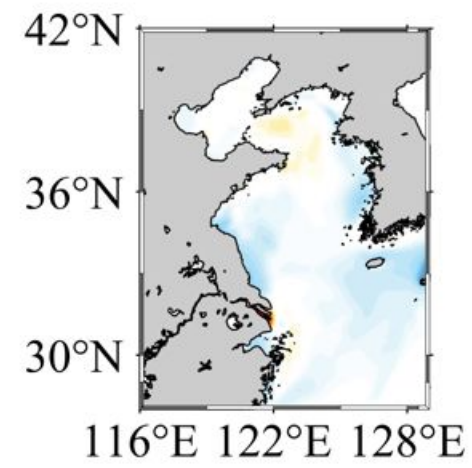
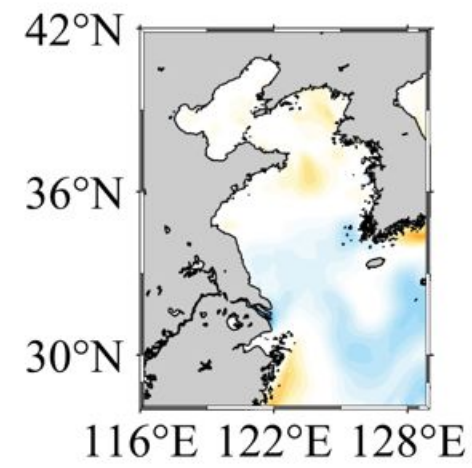
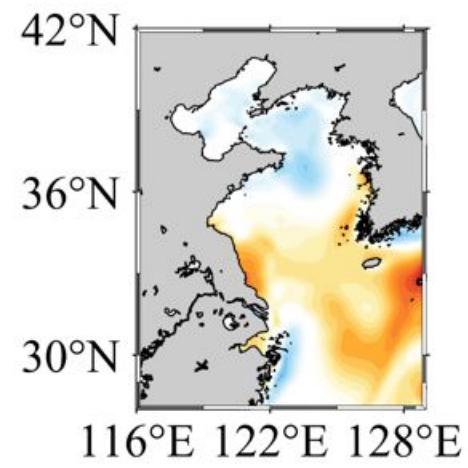
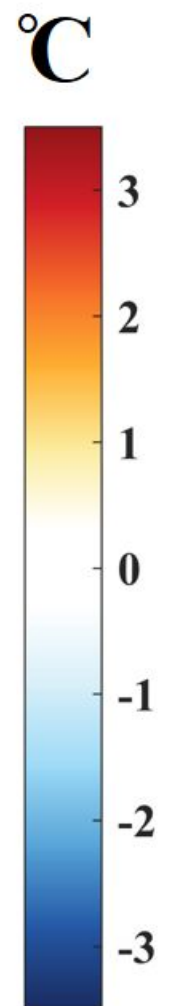
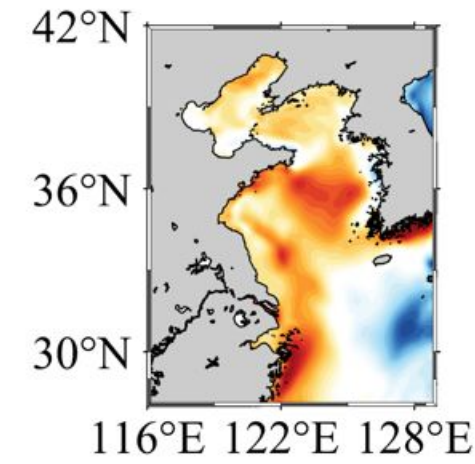
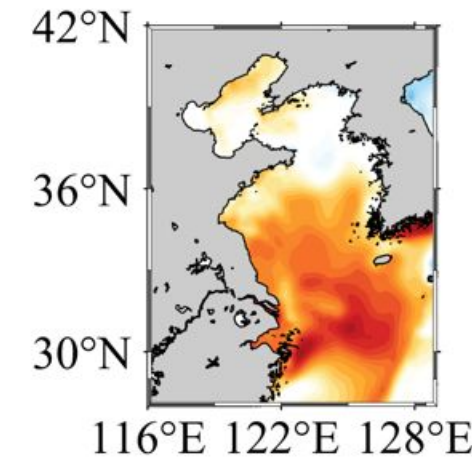
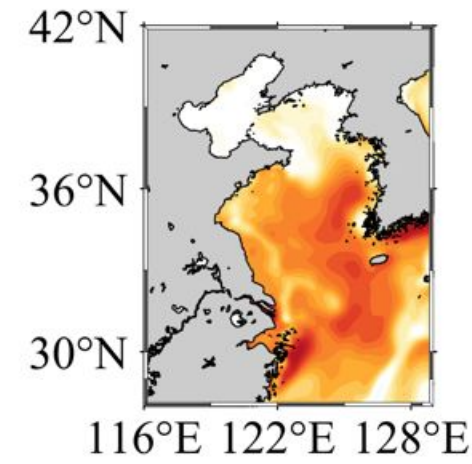
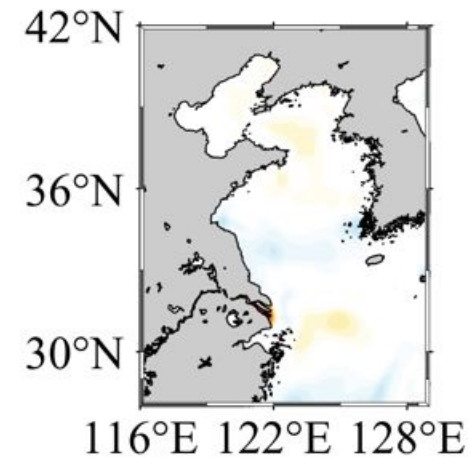
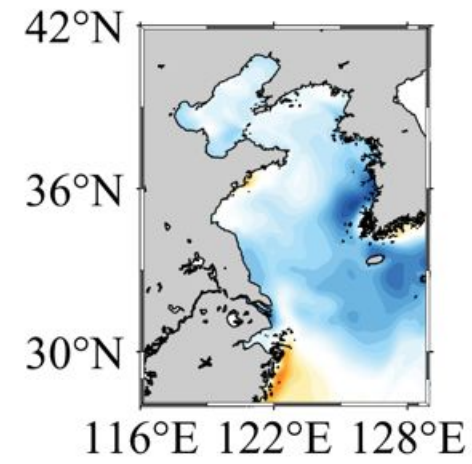
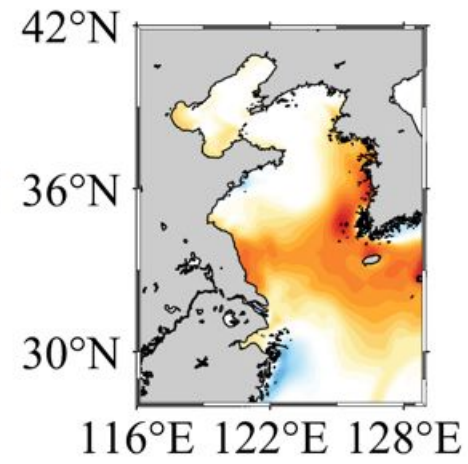
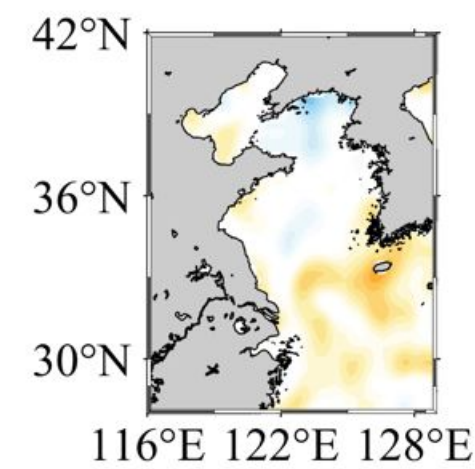
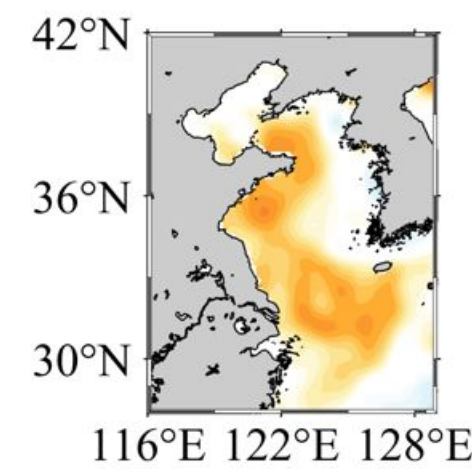
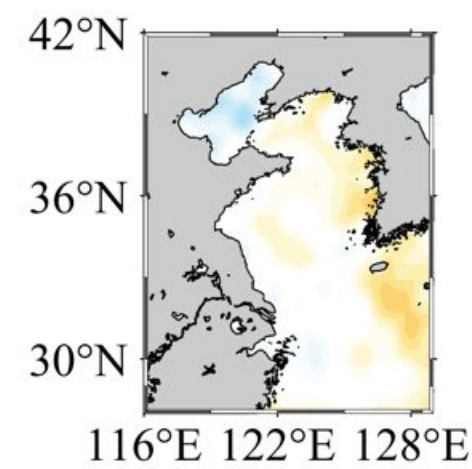
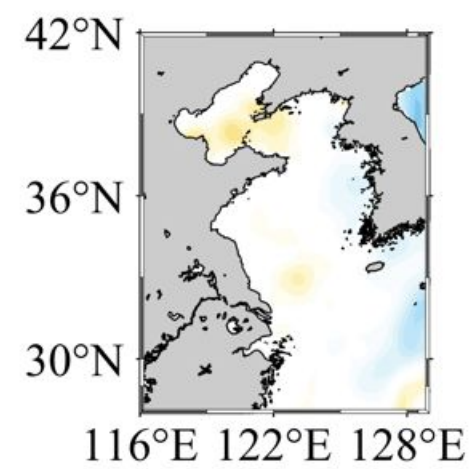
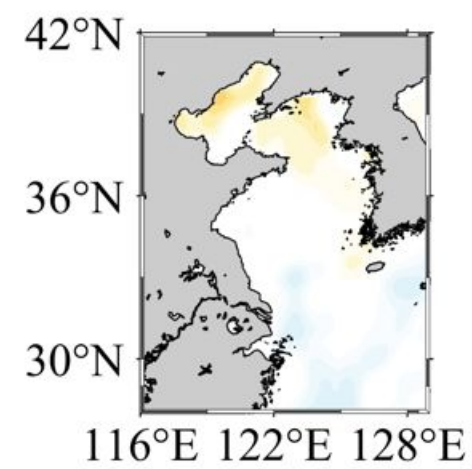
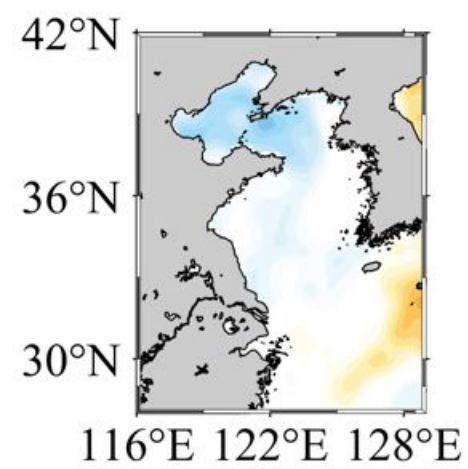
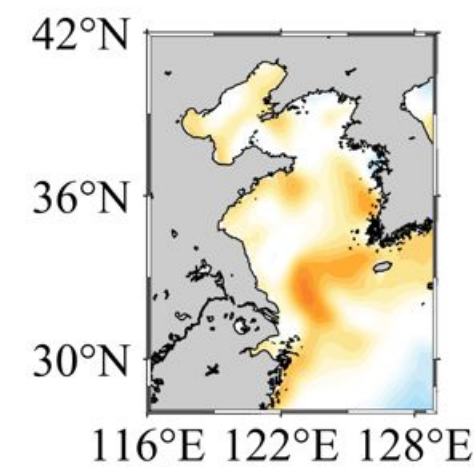
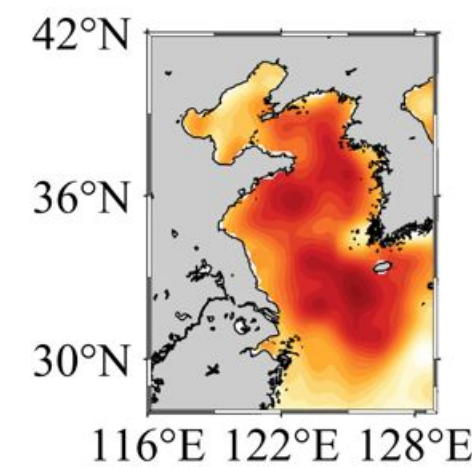
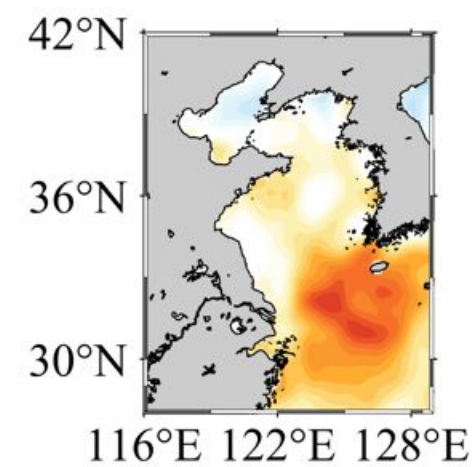
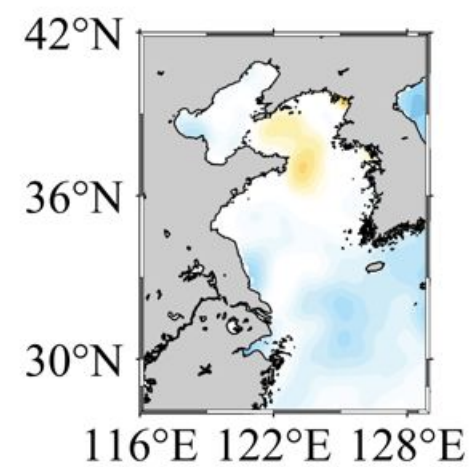
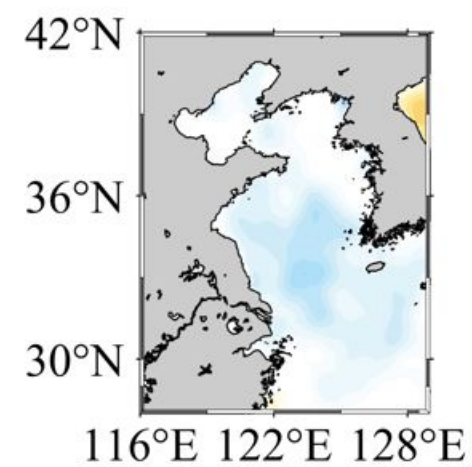
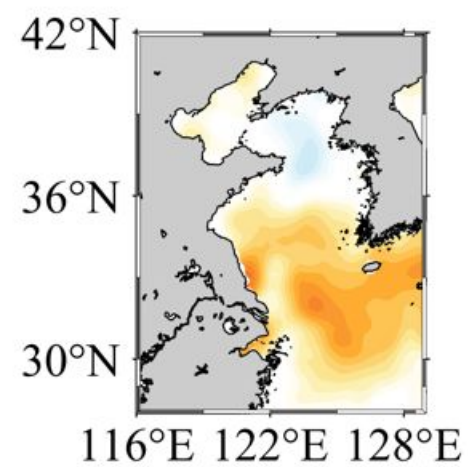
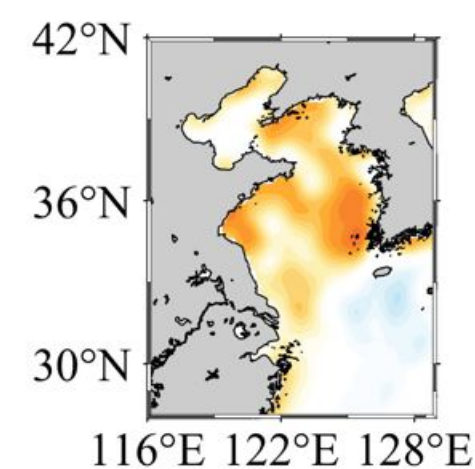
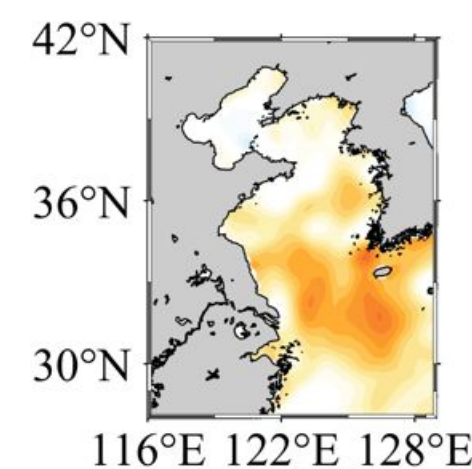
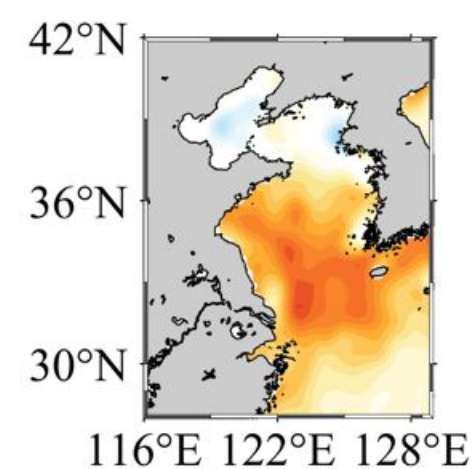
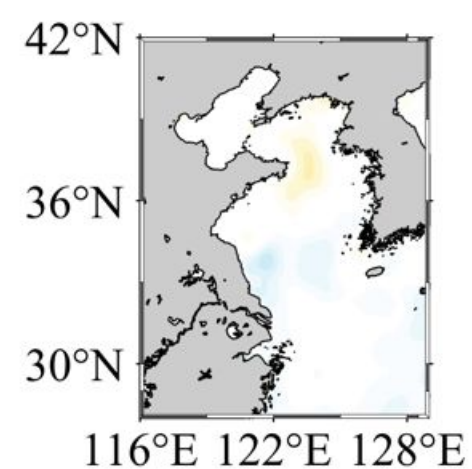
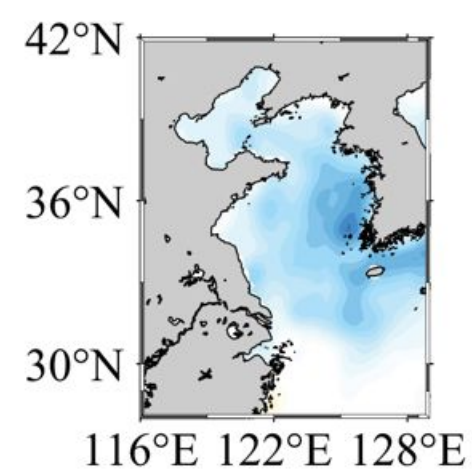
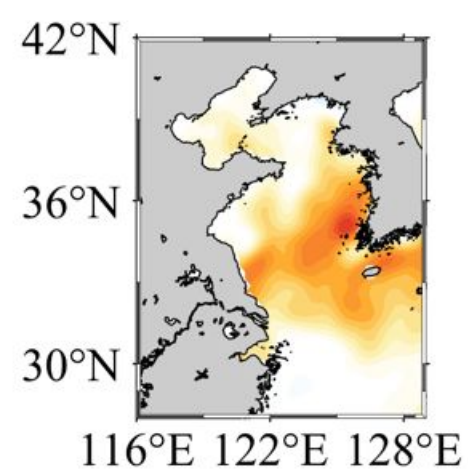


**RMSE**



**CC**

Figure 3.

**2013****2014****2015****2016****2017****2018****a****June****July****August****b****June****July****August**

**Figure 4.**

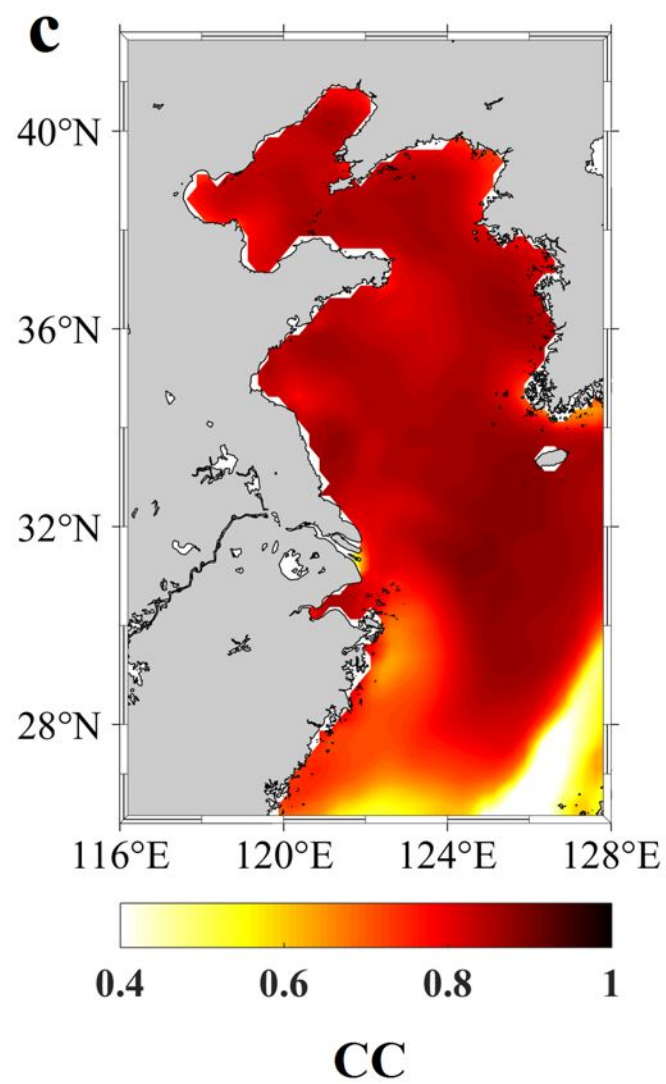
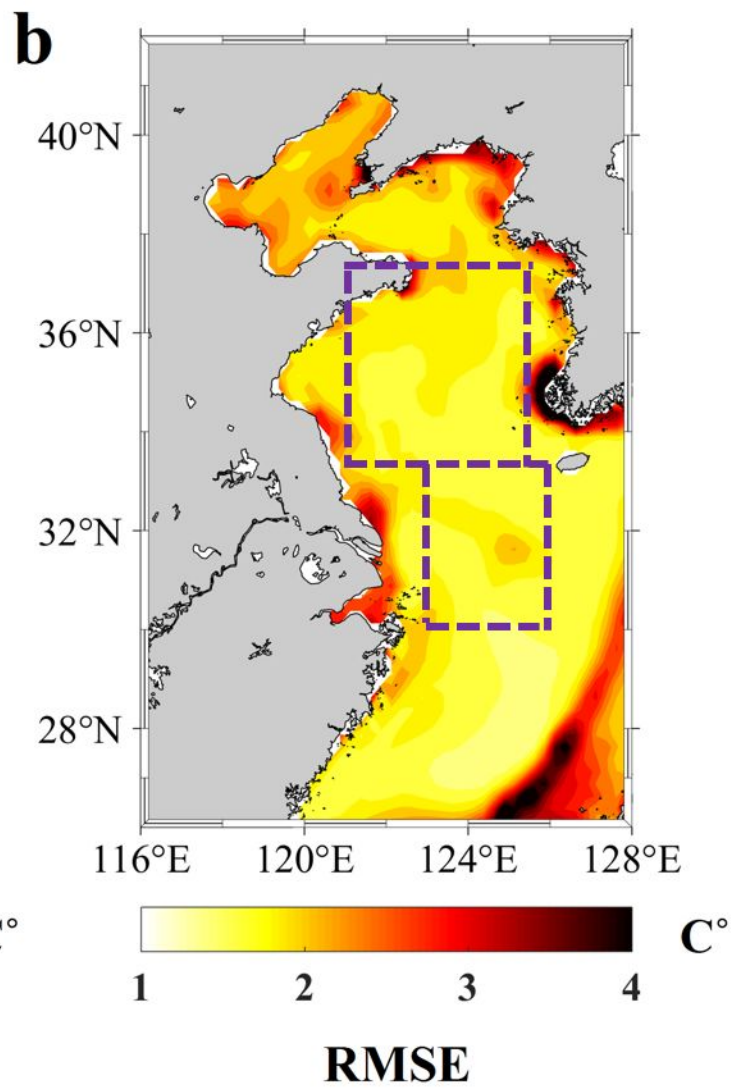
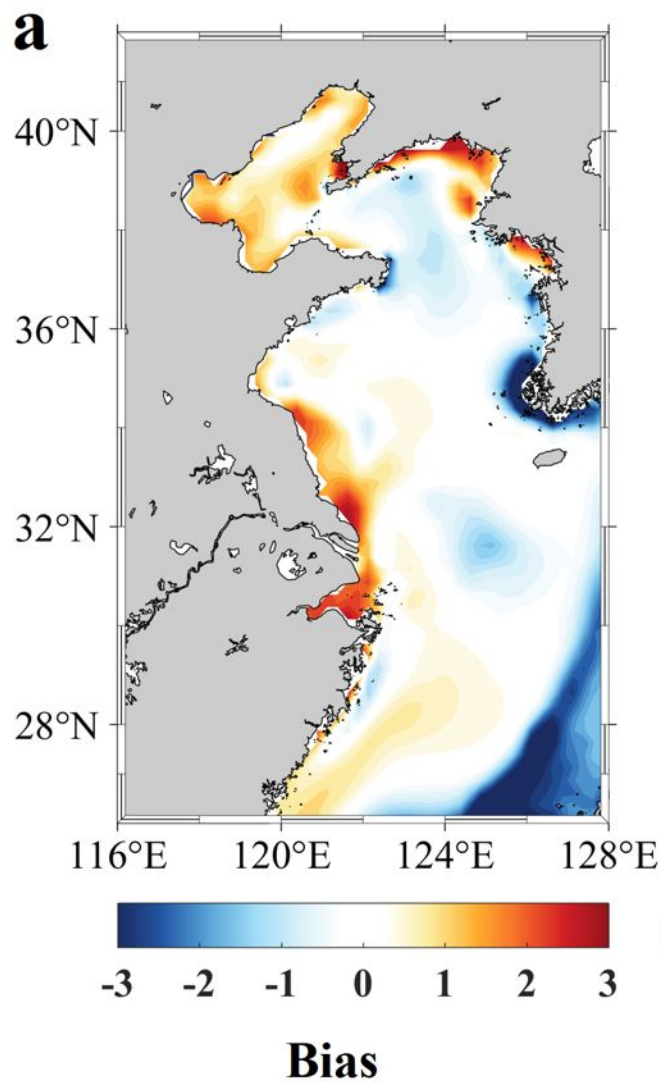
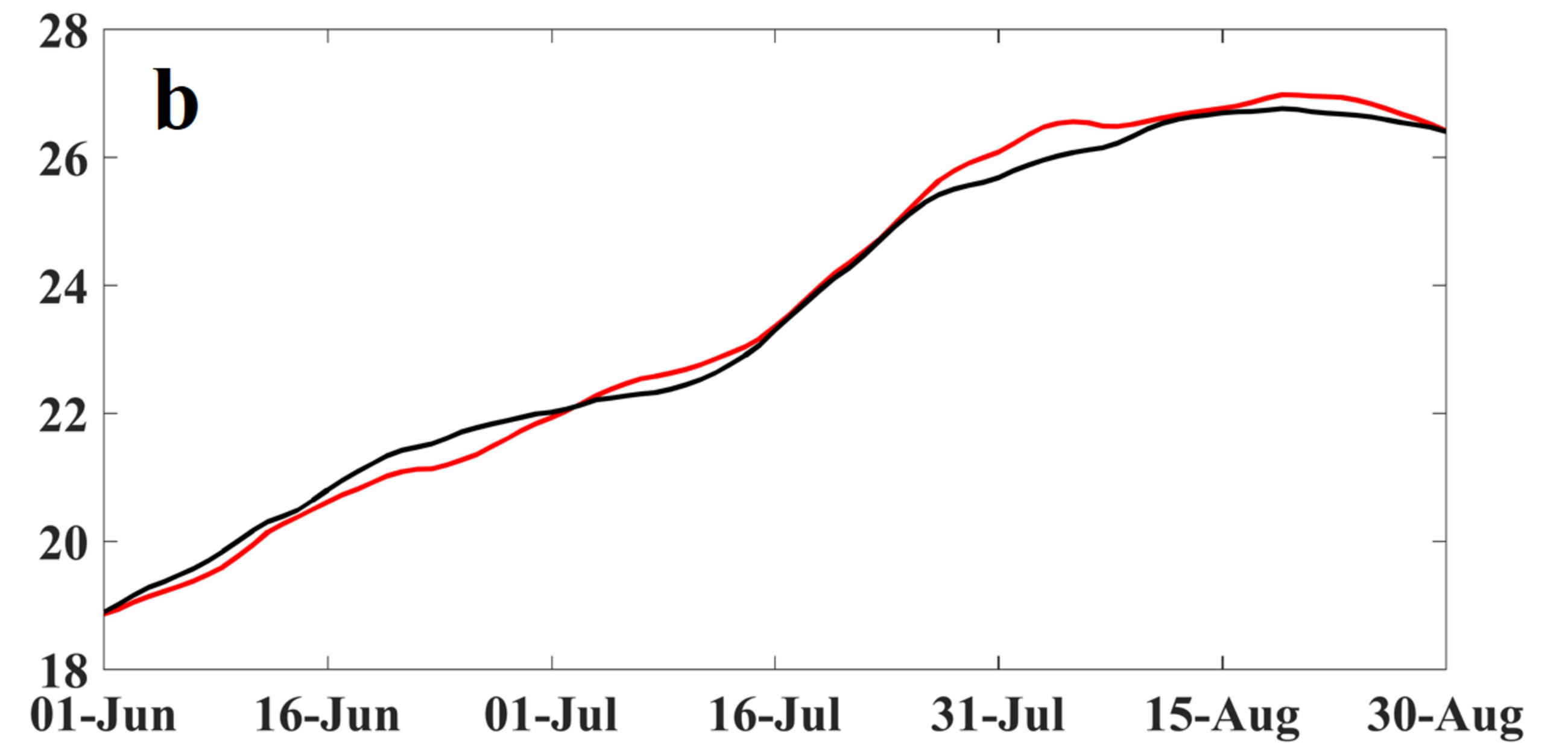
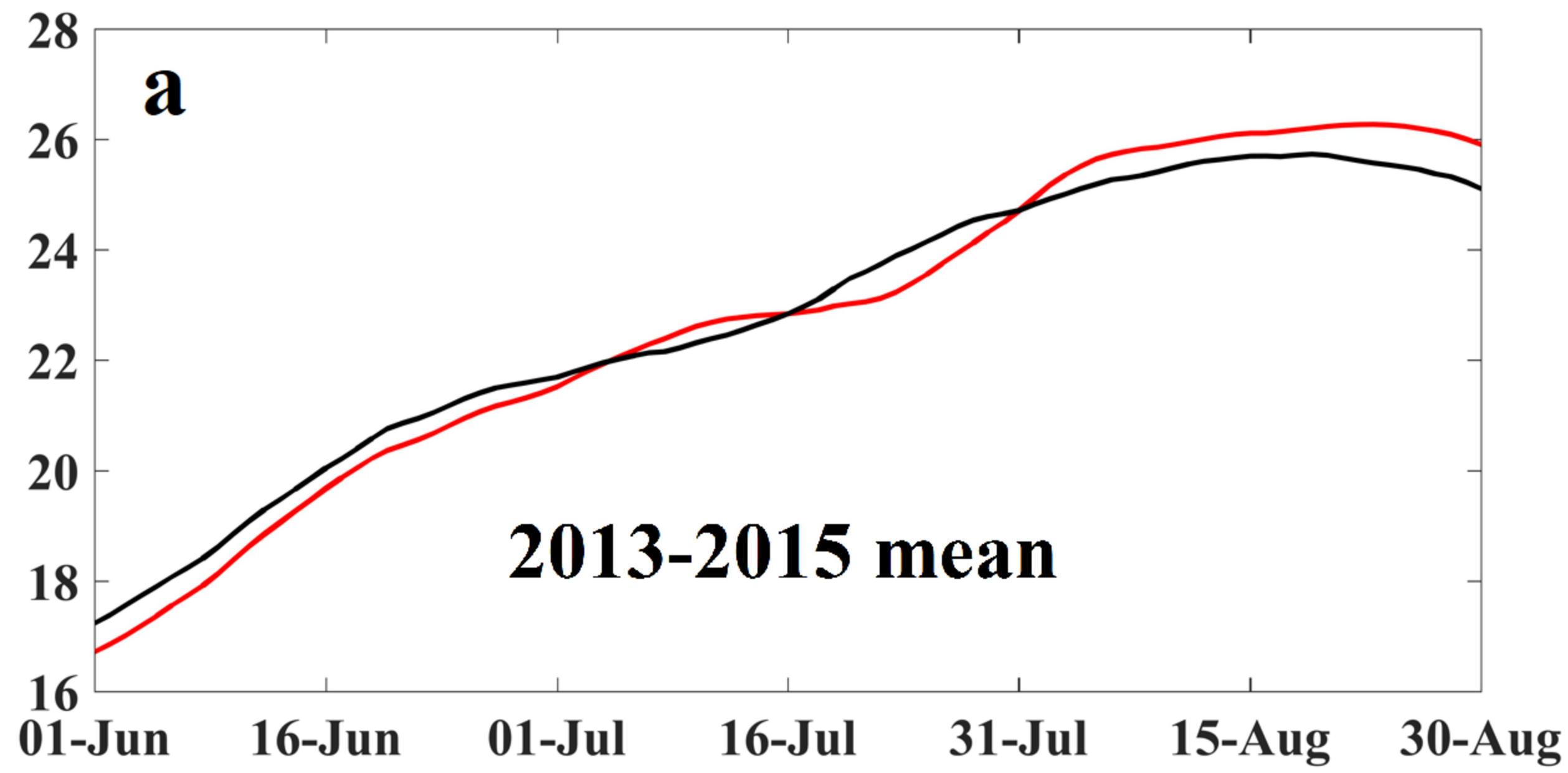


Figure 5.



Temperature (°C)

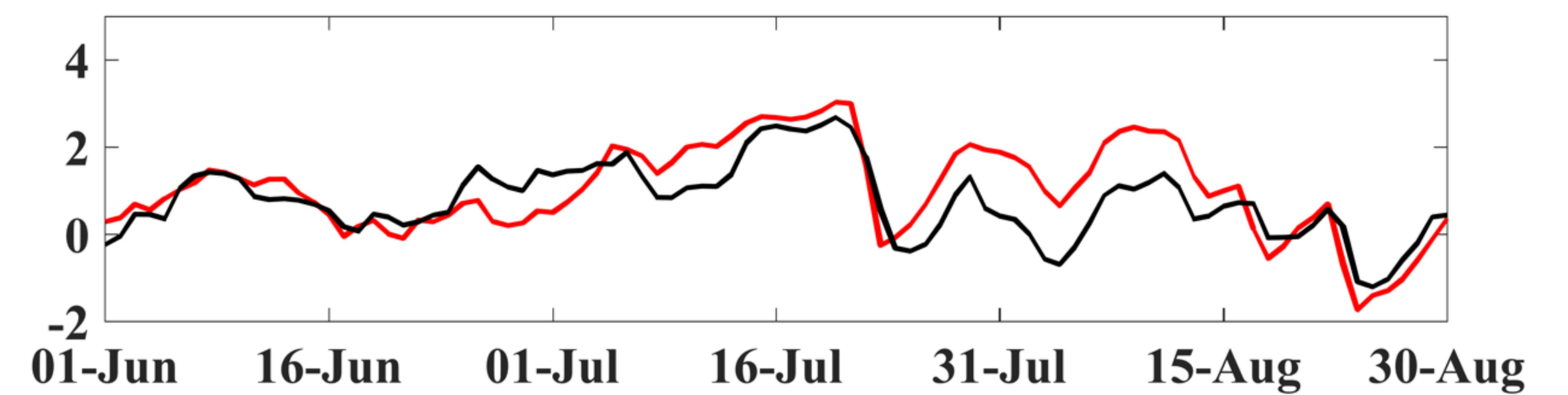
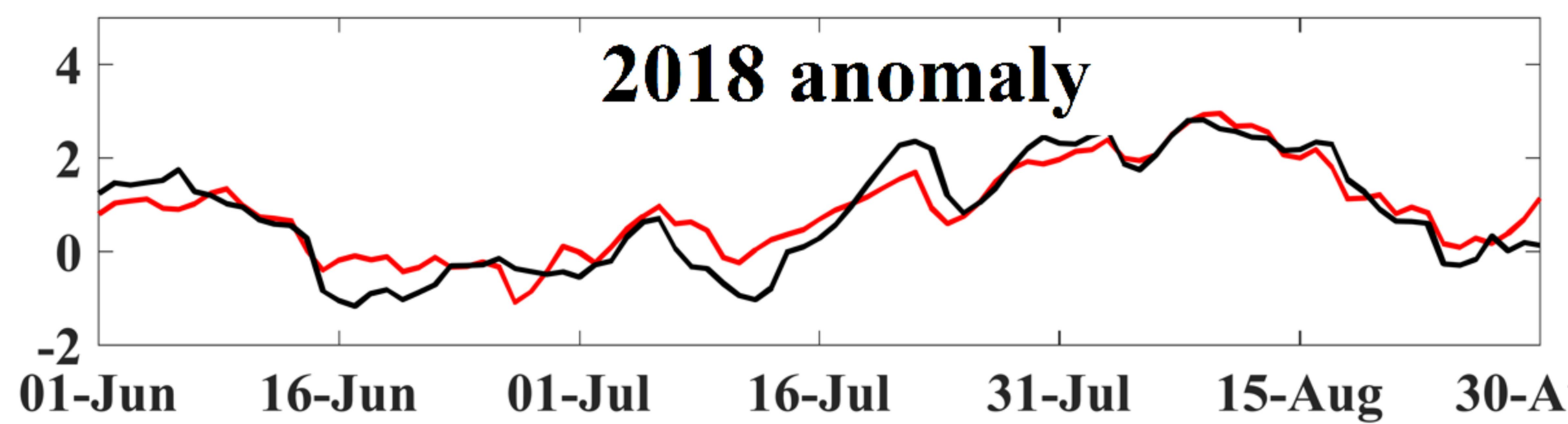
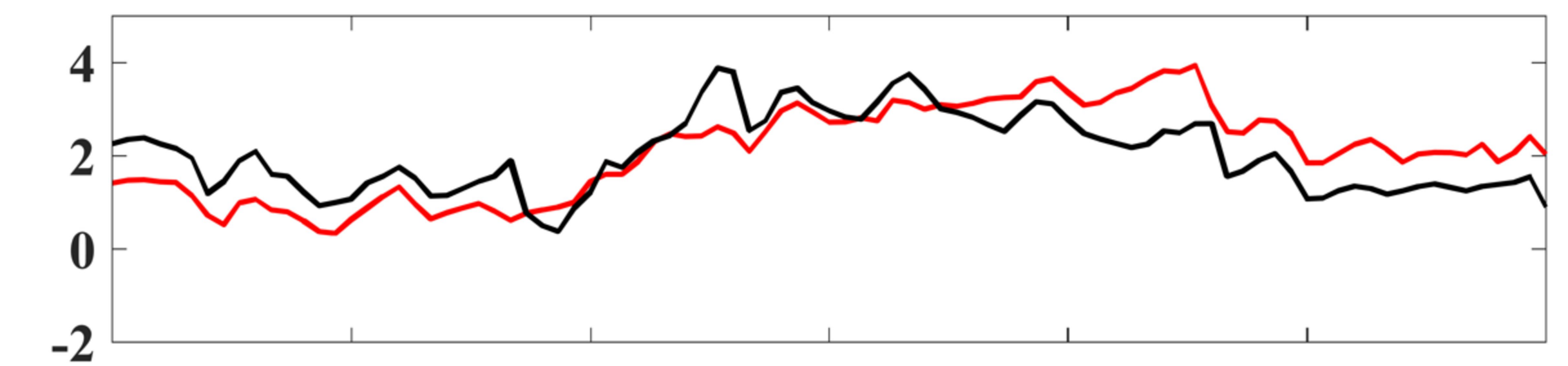
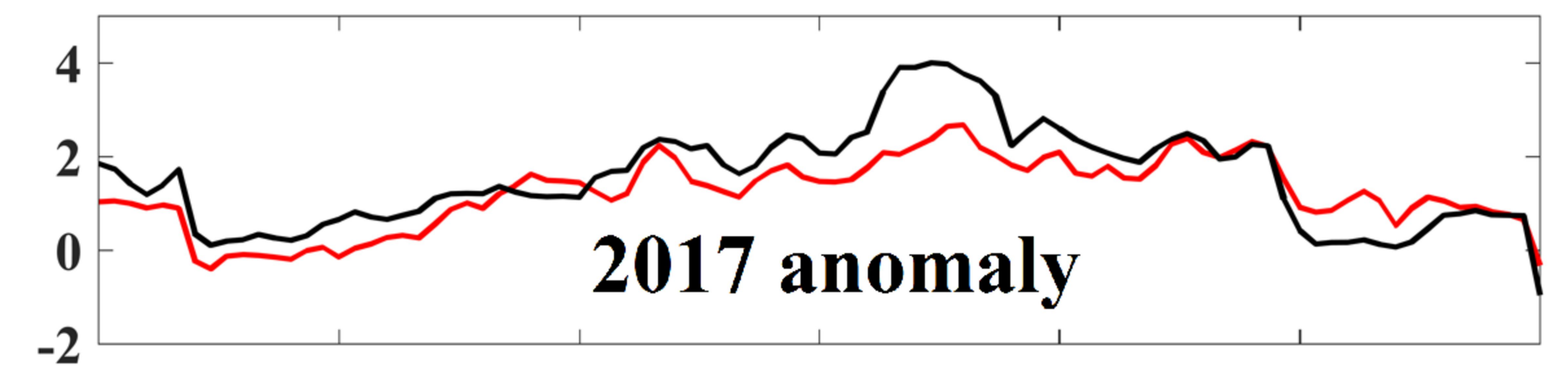
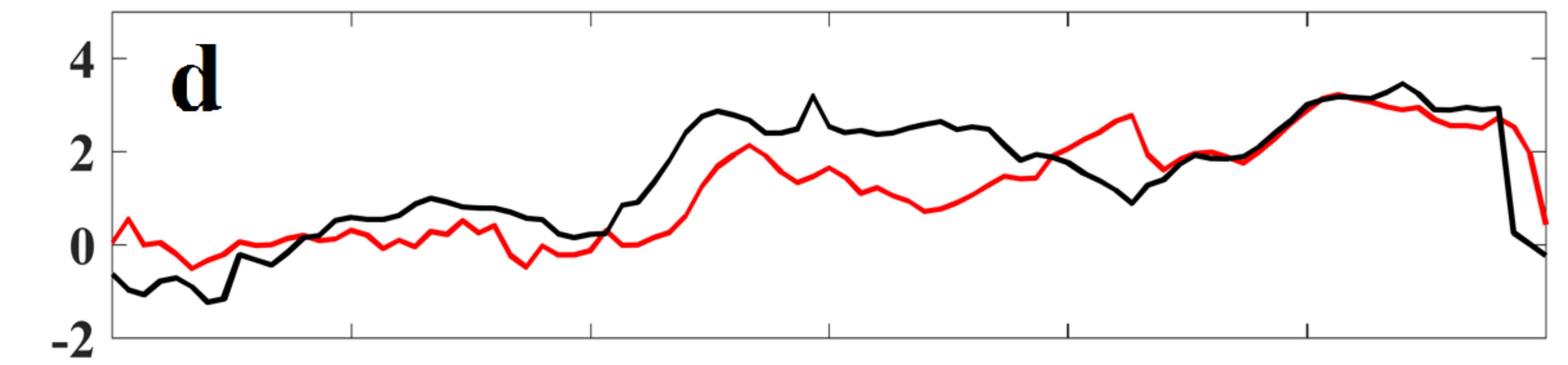
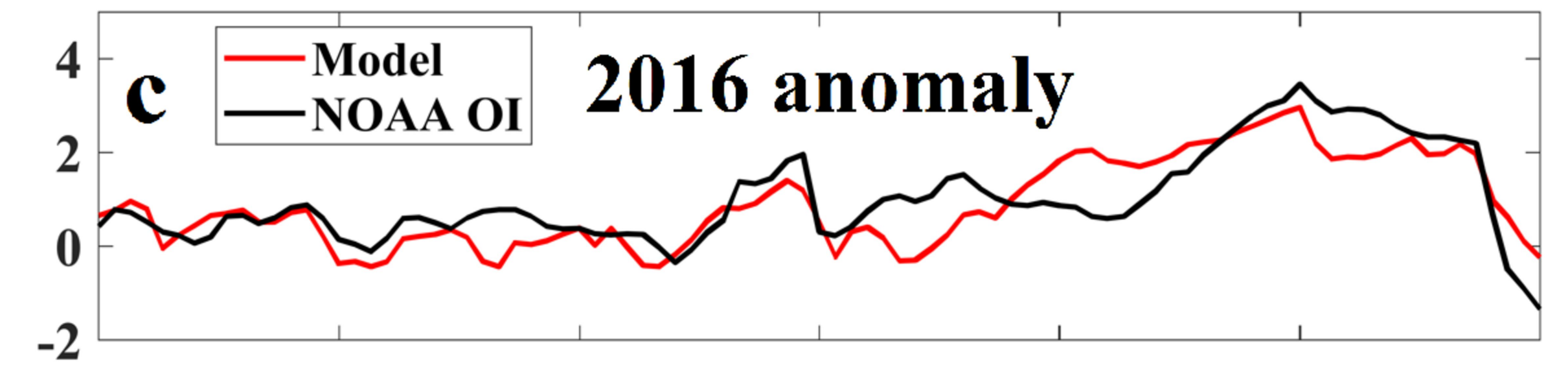
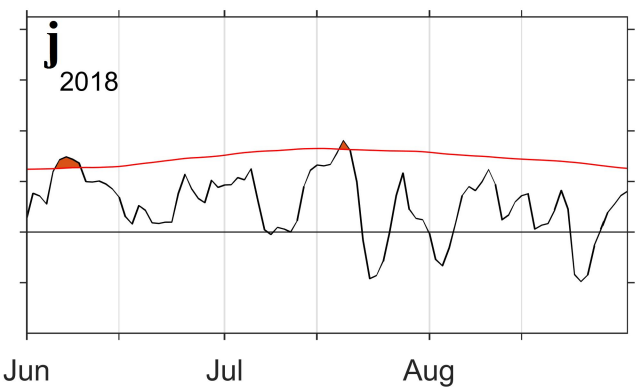
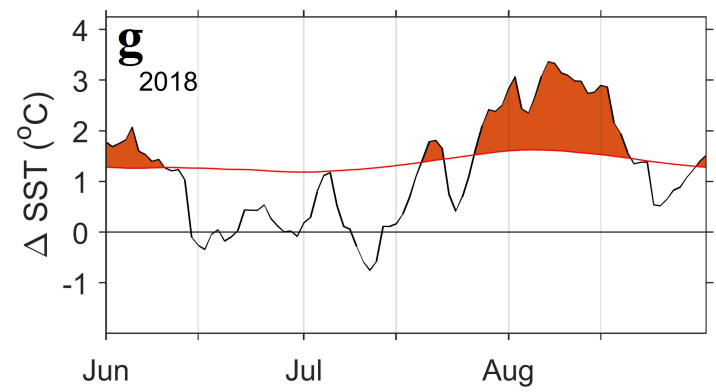
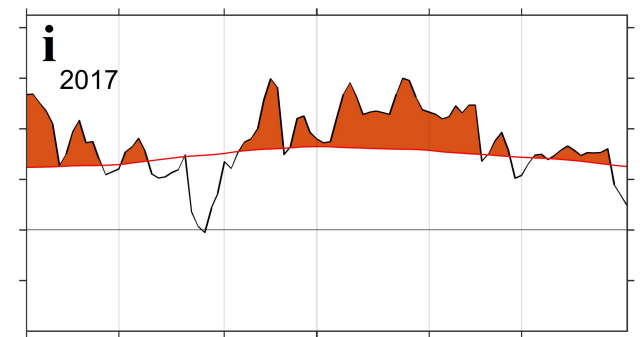
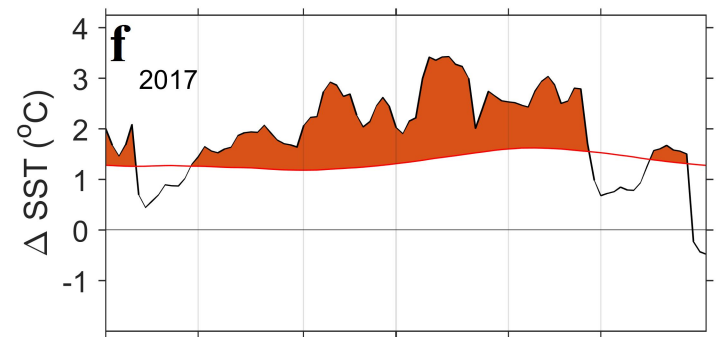
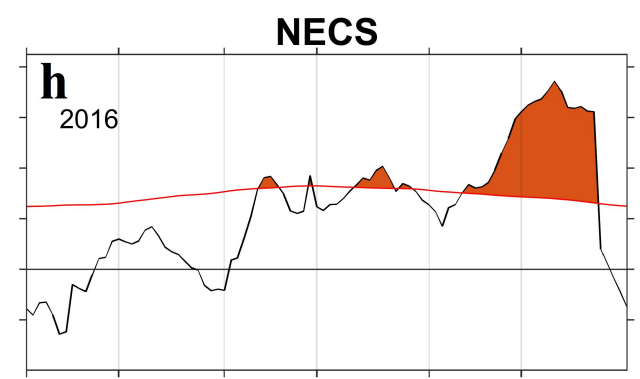
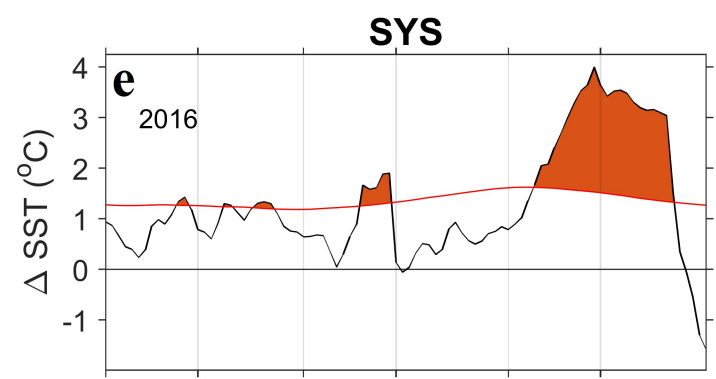
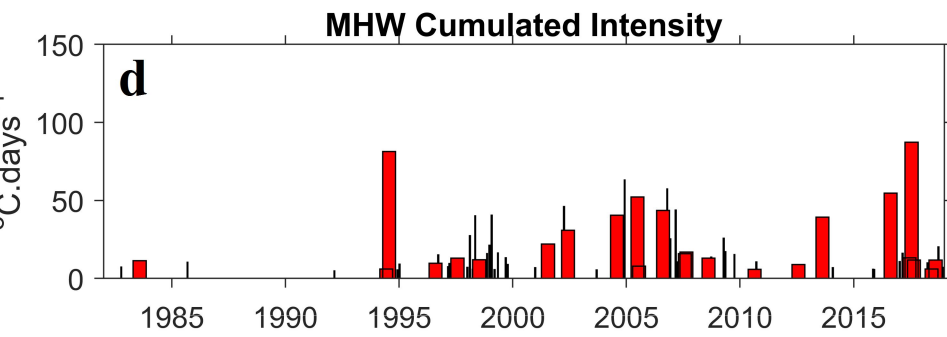
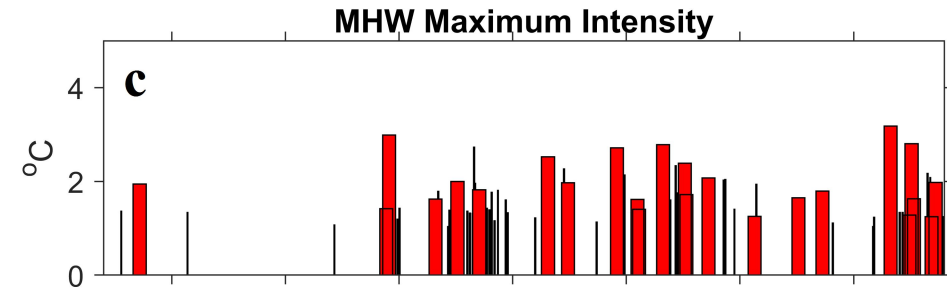
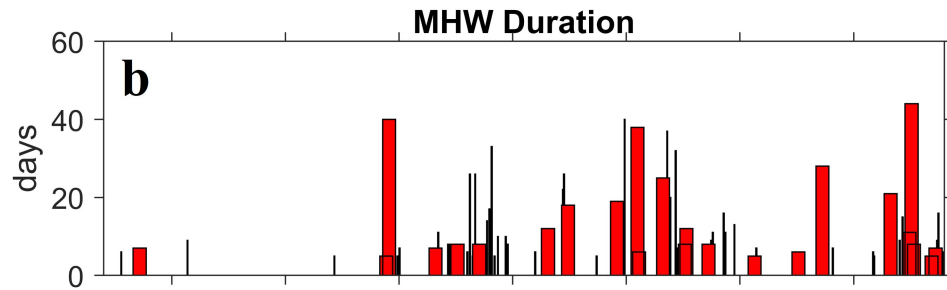
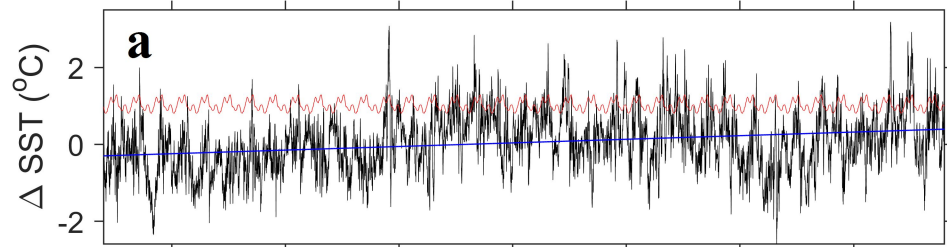


Figure 6.

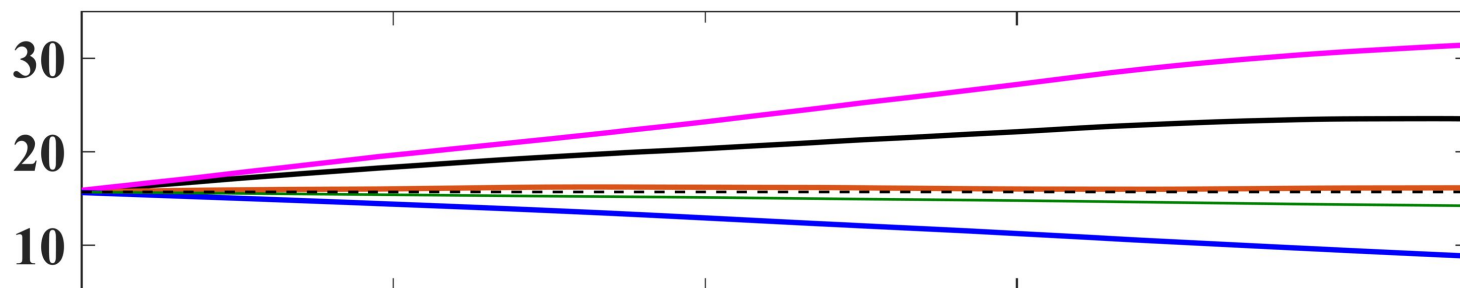


Jun Jul Aug

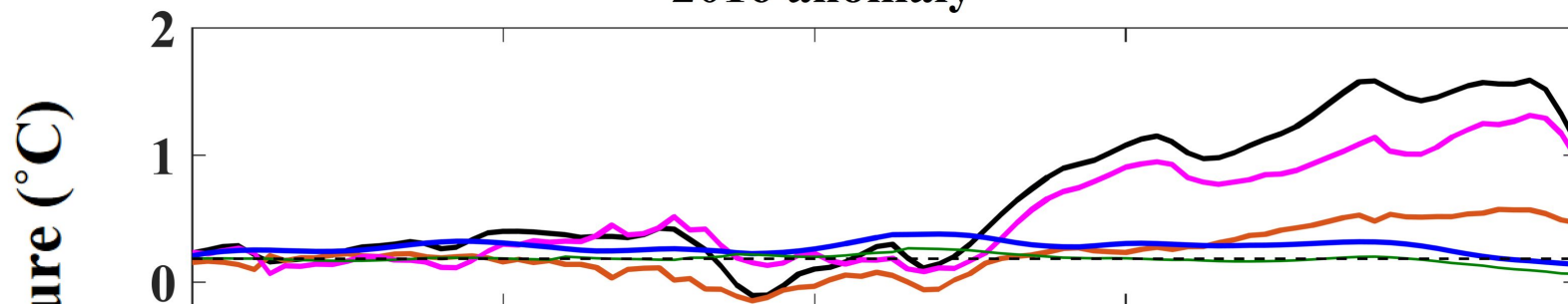
Jun Jul Aug

**Figure 7.**

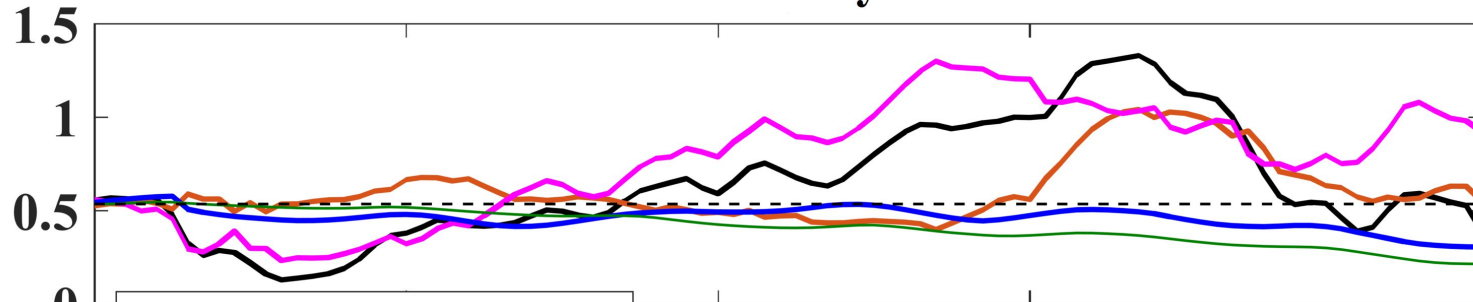
**2013-2015 mean**



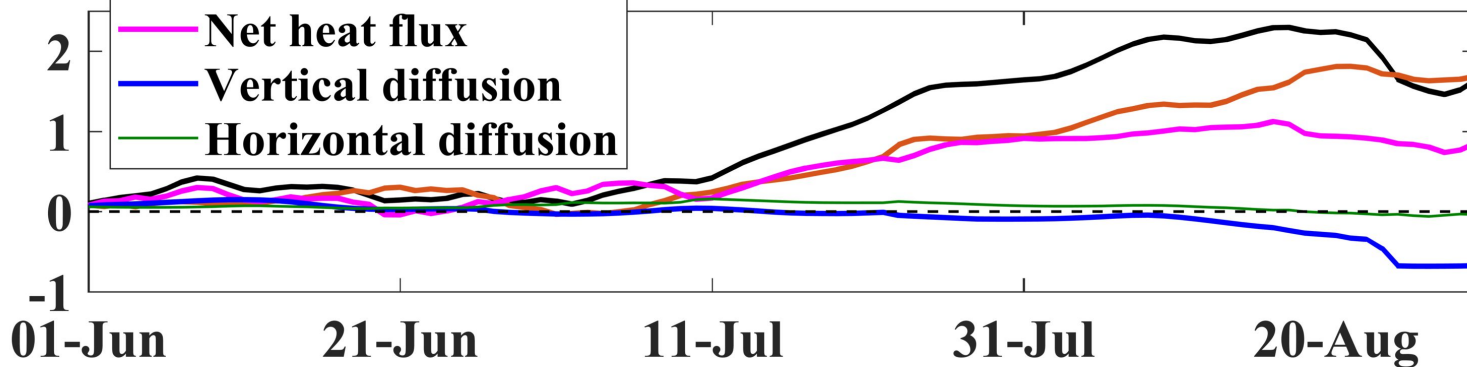
**2016 anomaly**



**2017 anomaly**



**2018 anomaly**



**Temperature (°C)**

- Total change**
- Advection**
- Net heat flux**
- Vertical diffusion**
- Horizontal diffusion**

**01-Jun**

**21-Jun**

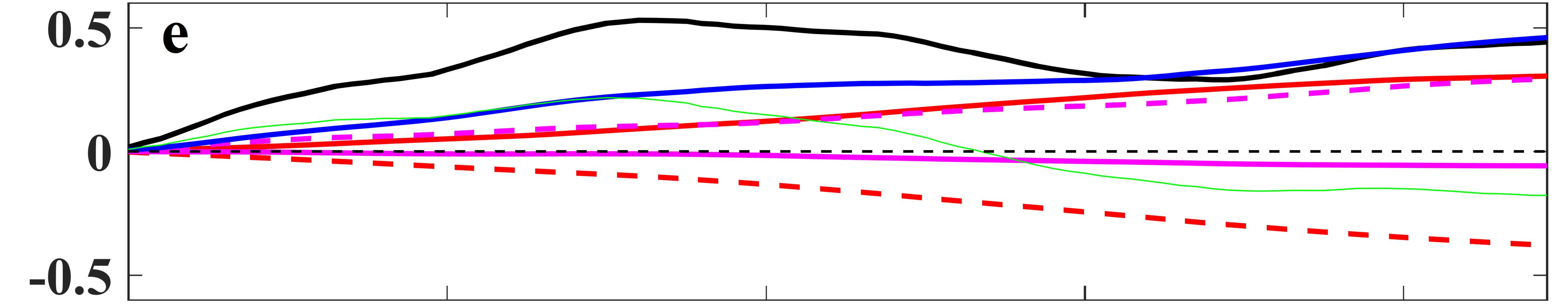
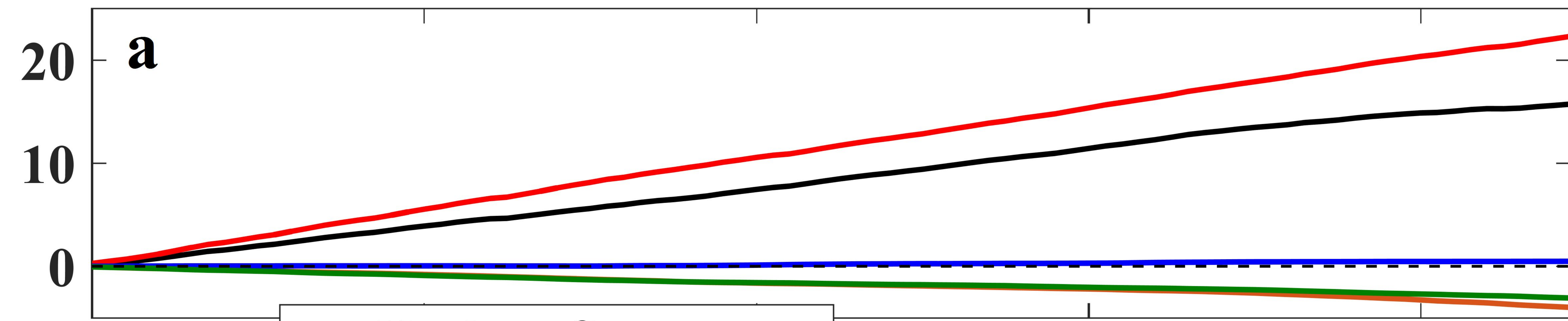
**11-Jul**

**31-Jul**

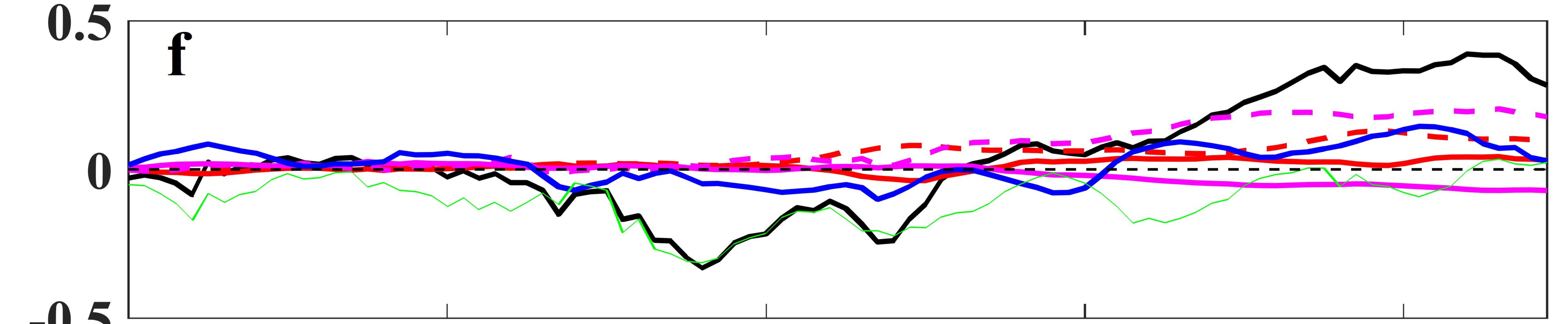
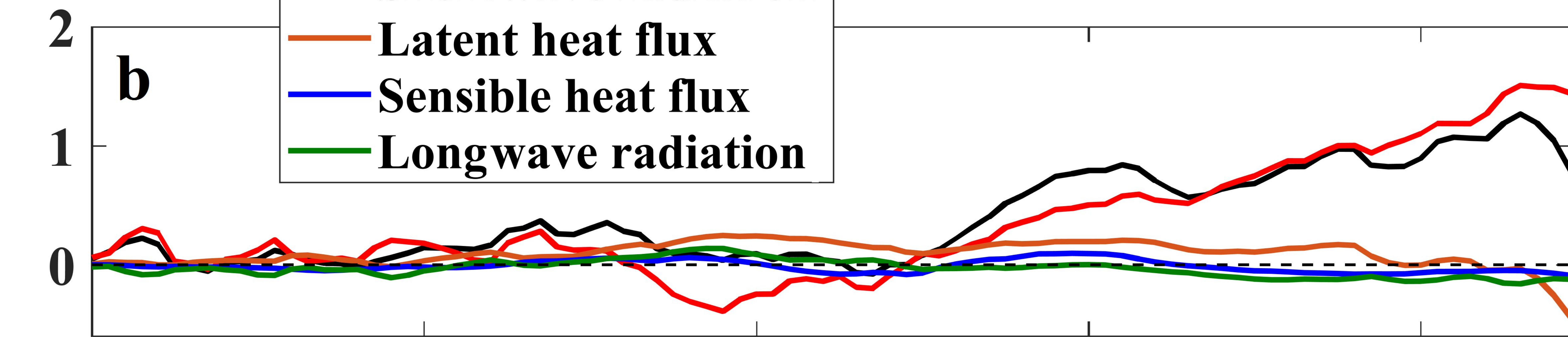
**20-Aug**

Figure 8.

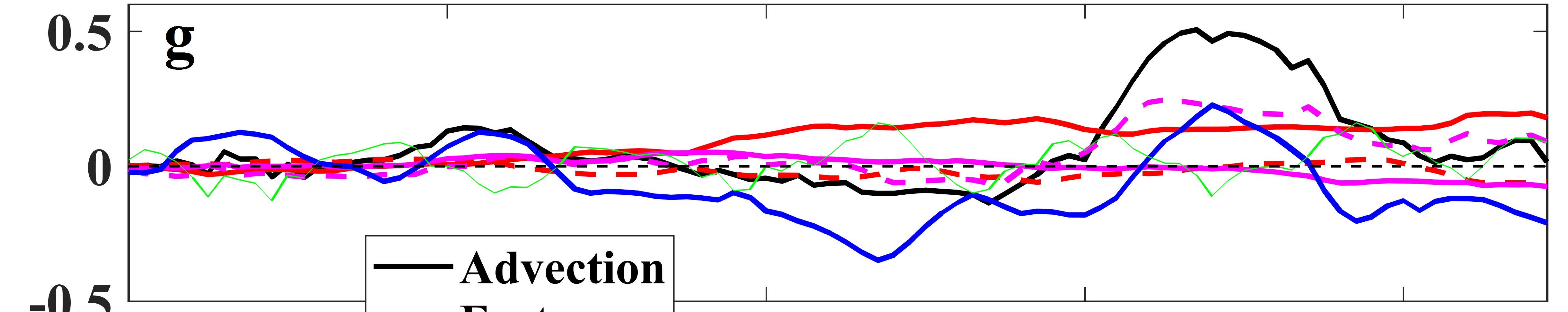
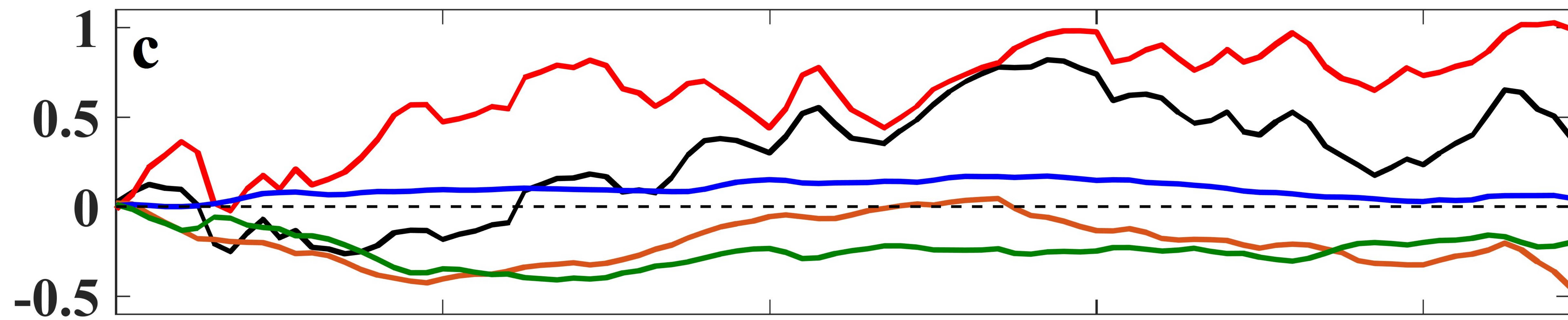
2013-2015 mean



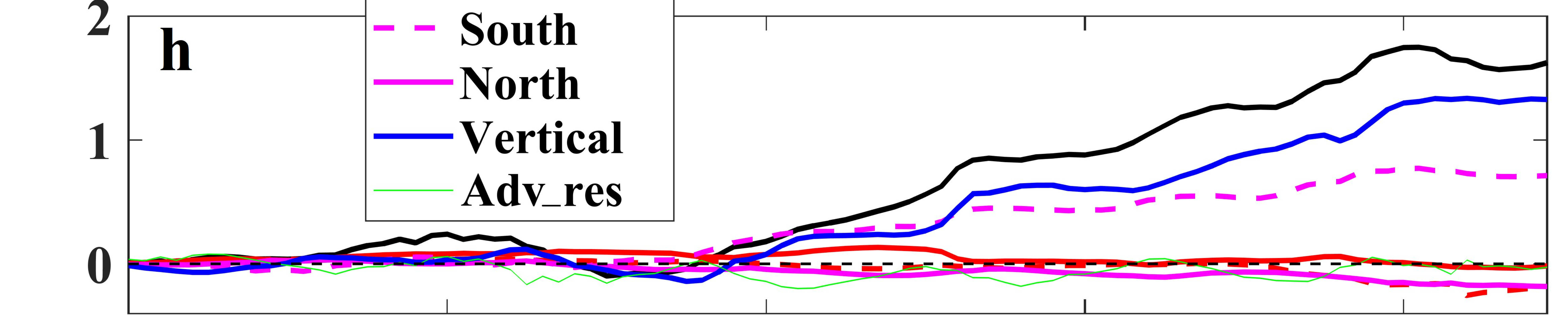
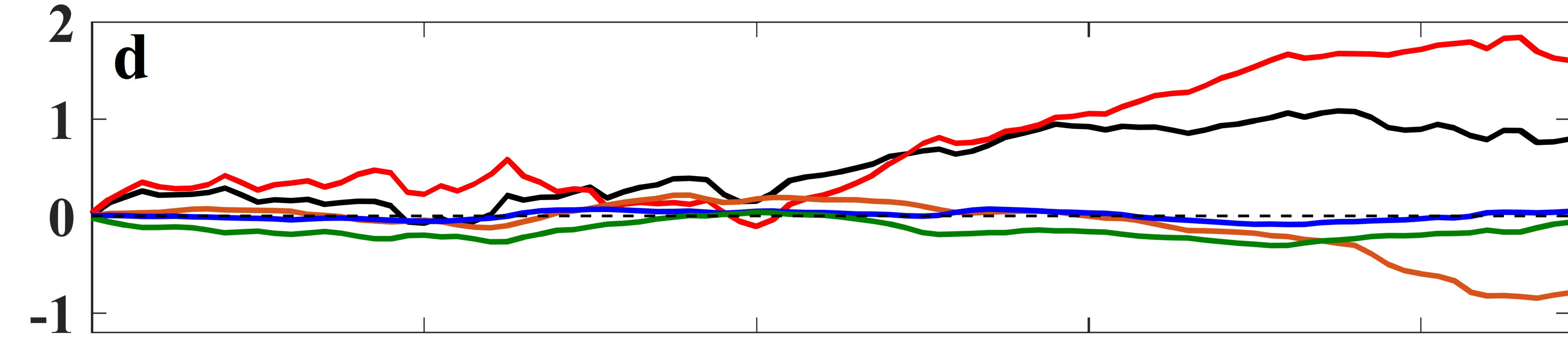
2016 anomaly



2017 anomaly



2018 anomaly



Cumulative temperature changes (°C)

01-Jun 21-Jun 11-Jul 31-Jul 20-Aug

01-Jun 21-Jun 11-Jul 31-Jul 20-Aug

- Advection
- - East
- West
- - South
- - North
- Vertical
- Adv\_res

Figure 9.

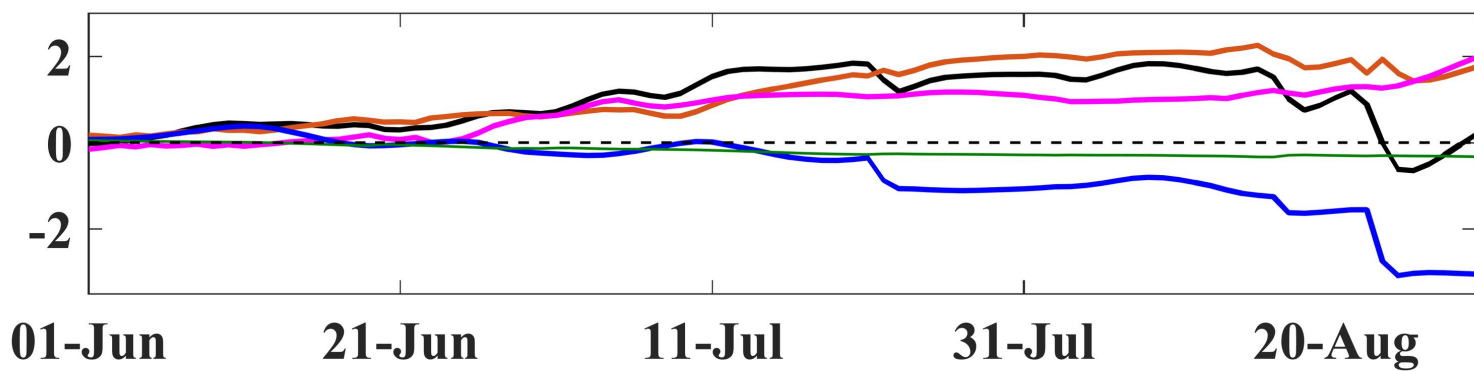
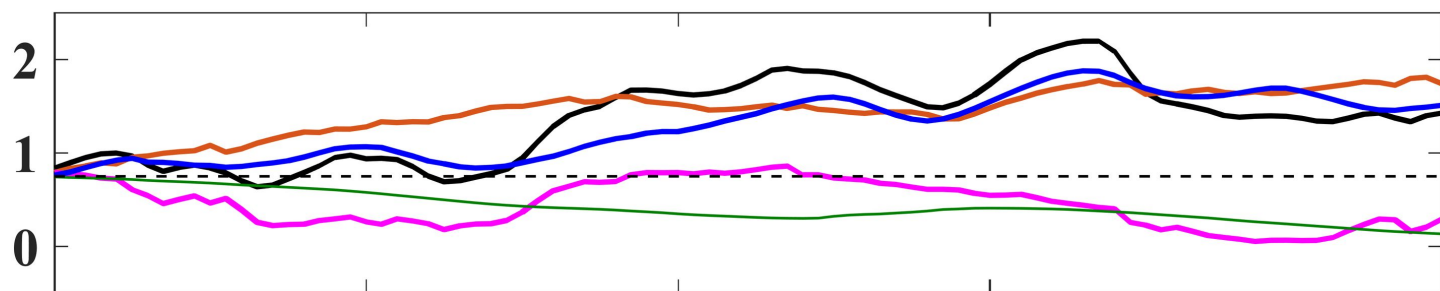
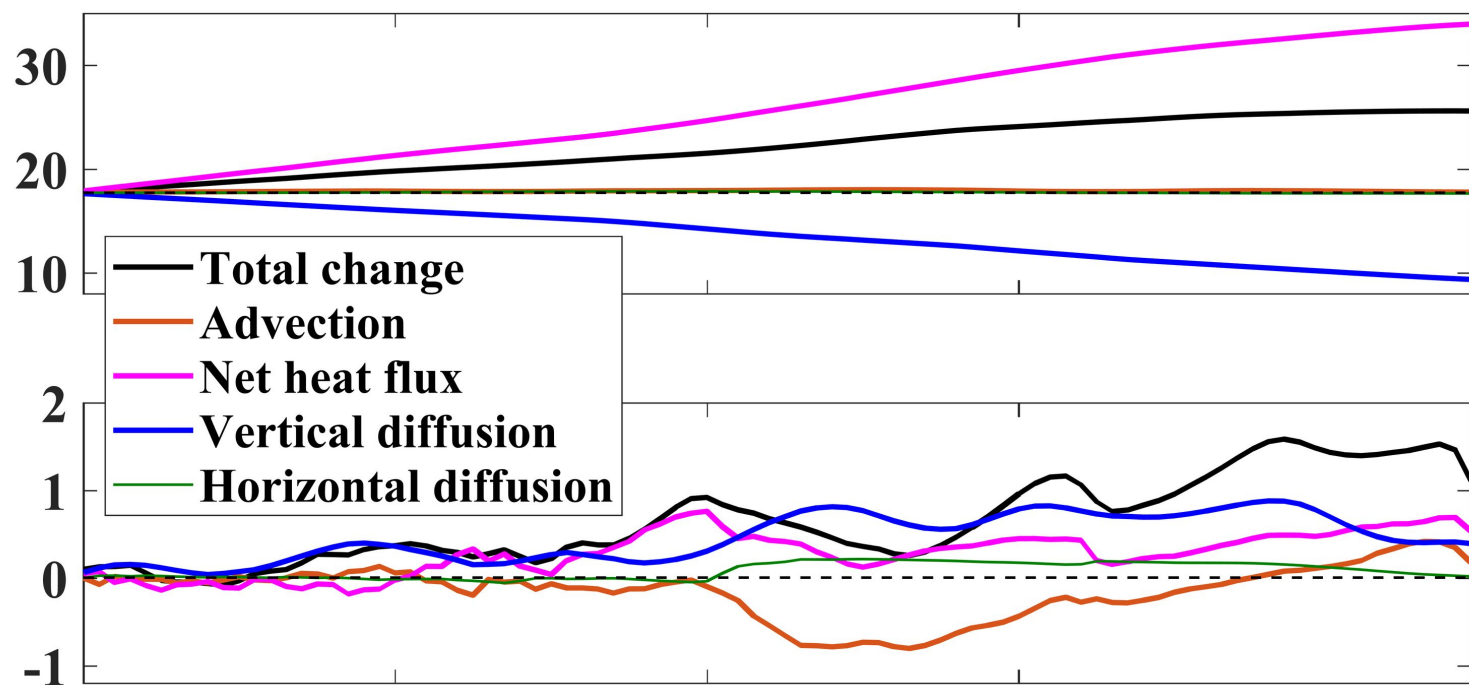
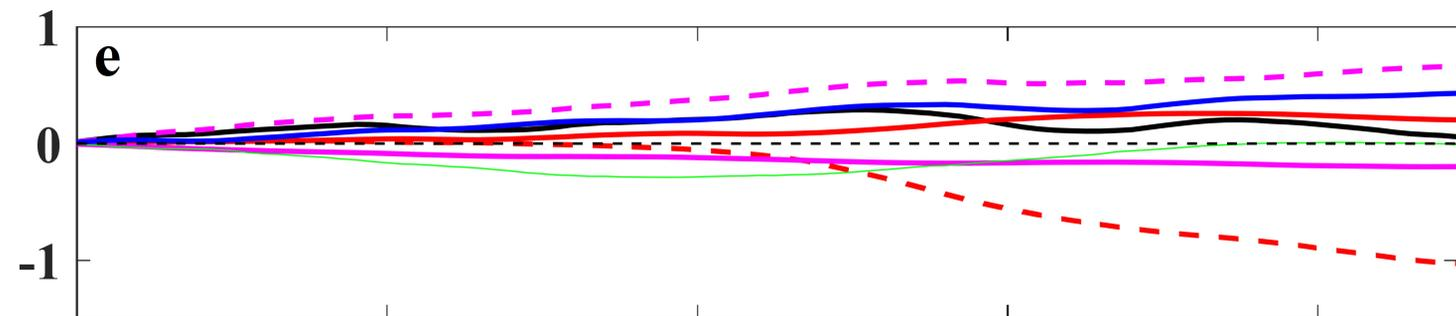
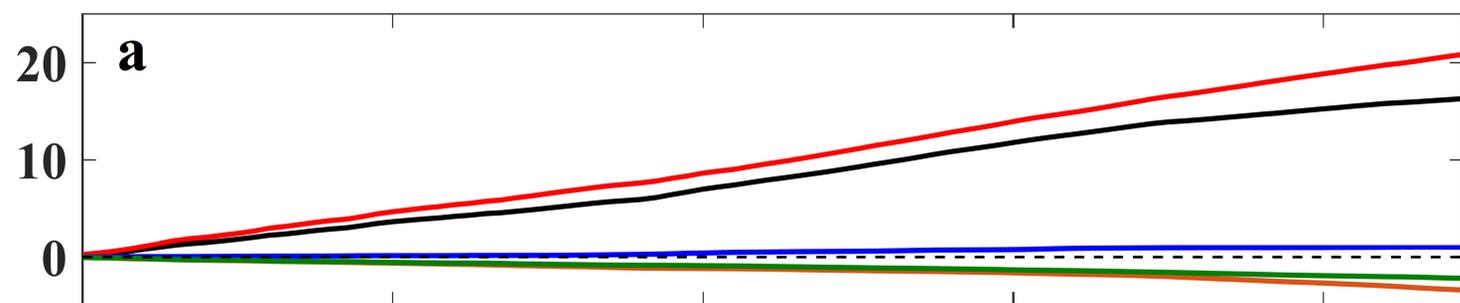
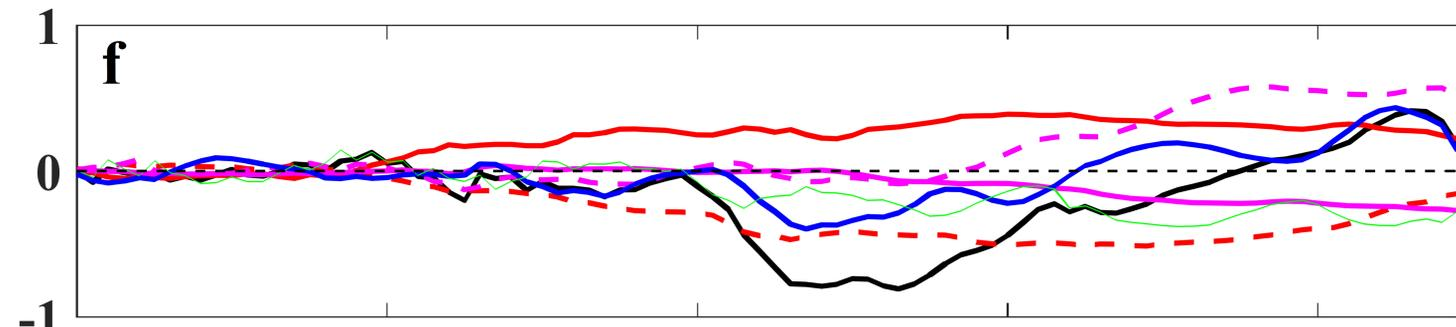
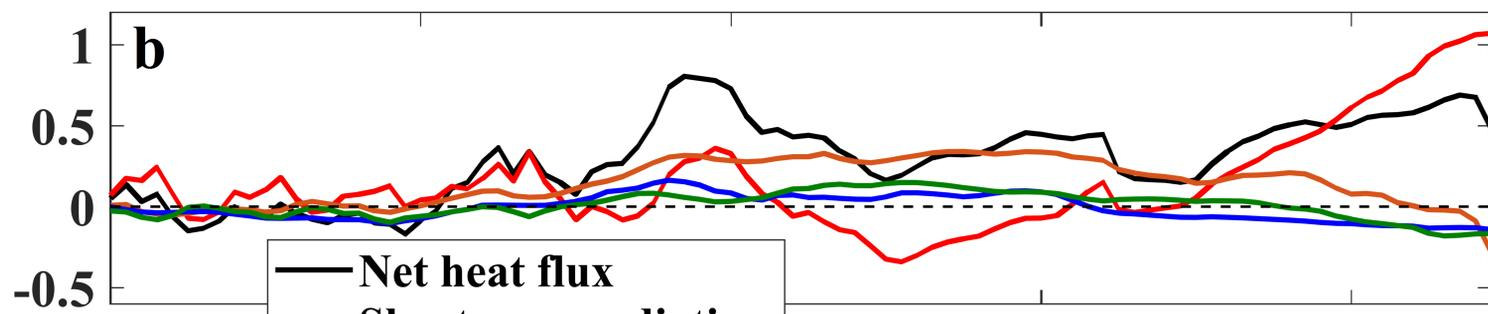


Figure 10.

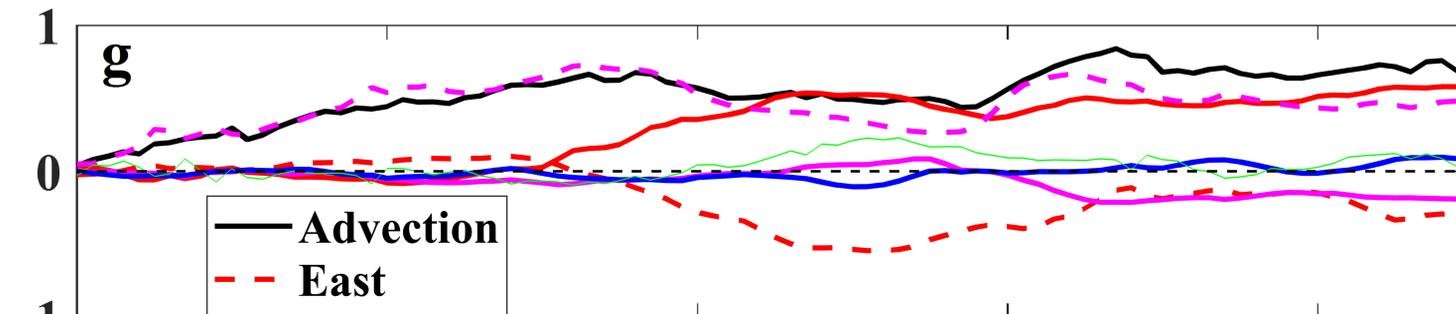
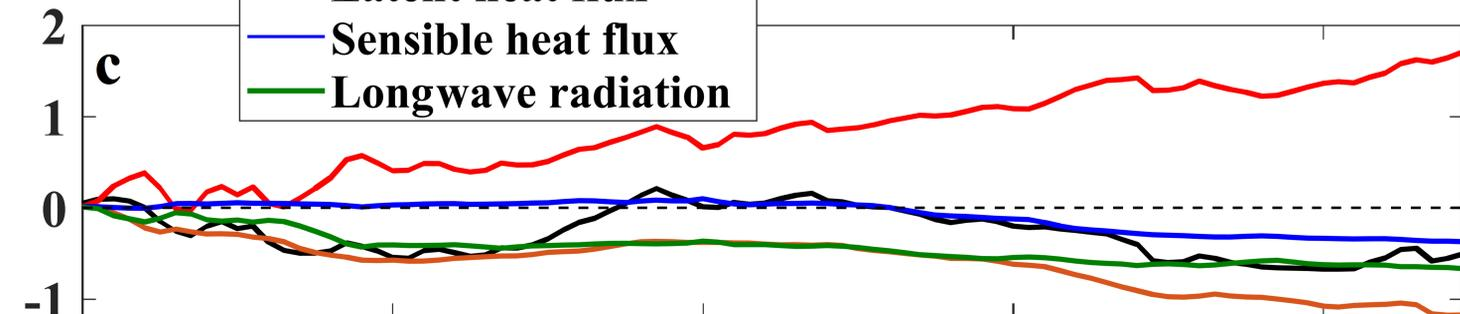
2013-2015 mean



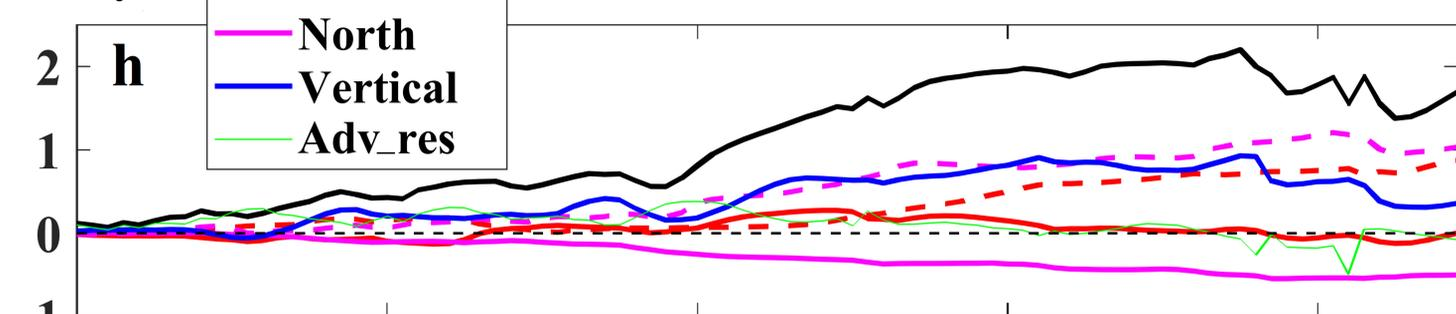
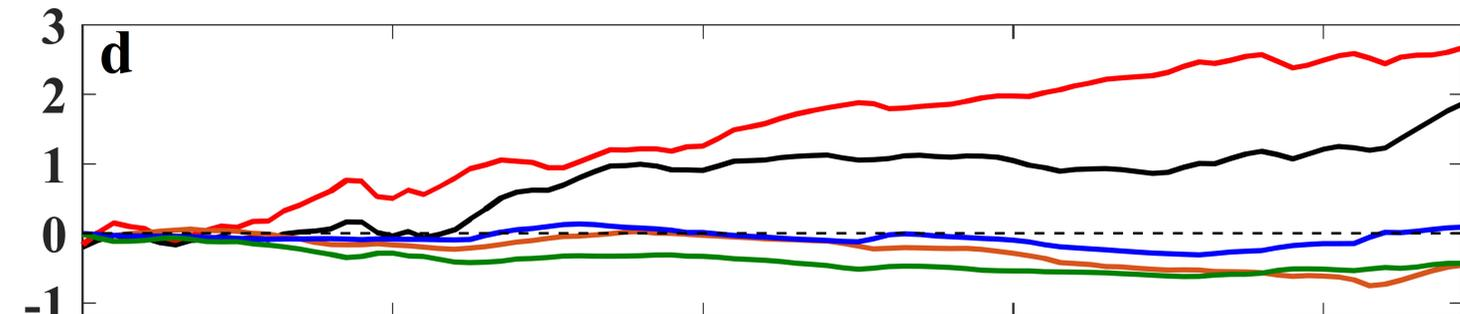
2016 anomaly



2017 anomaly



2018 anomaly



Cumulative temperature changes (°C)

01-Jun 21-Jun 11-Jul 31-Jul 20-Aug

01-Jun 21-Jun 11-Jul 31-Jul 20-Aug

- Net heat flux
- Shortwave radiation
- Latent heat flux
- Sensible heat flux
- Longwave radiation

- Advection
- - East
- West
- - South
- North
- Vertical
- Adv\_res

Figure 11.

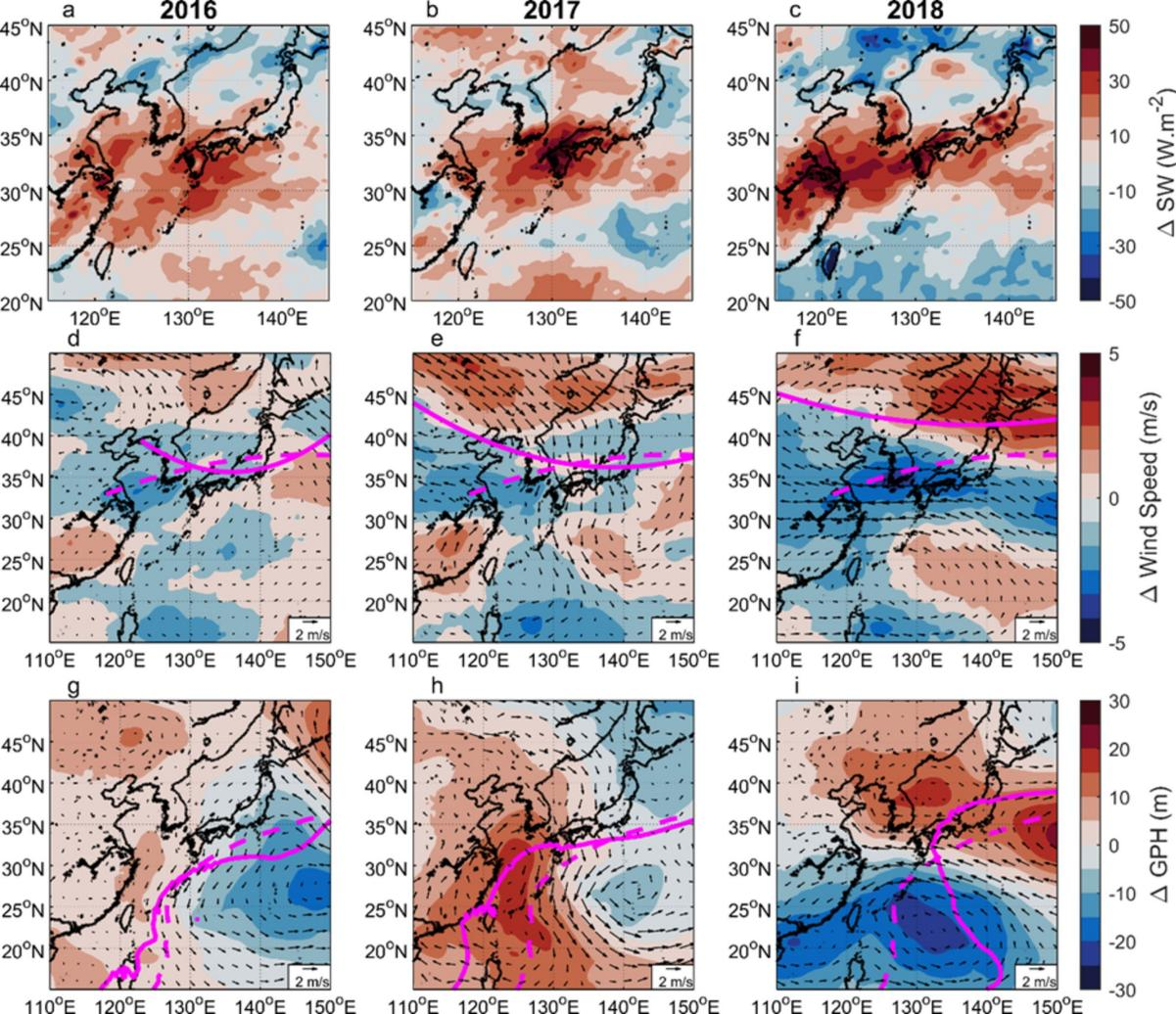


Figure 12.

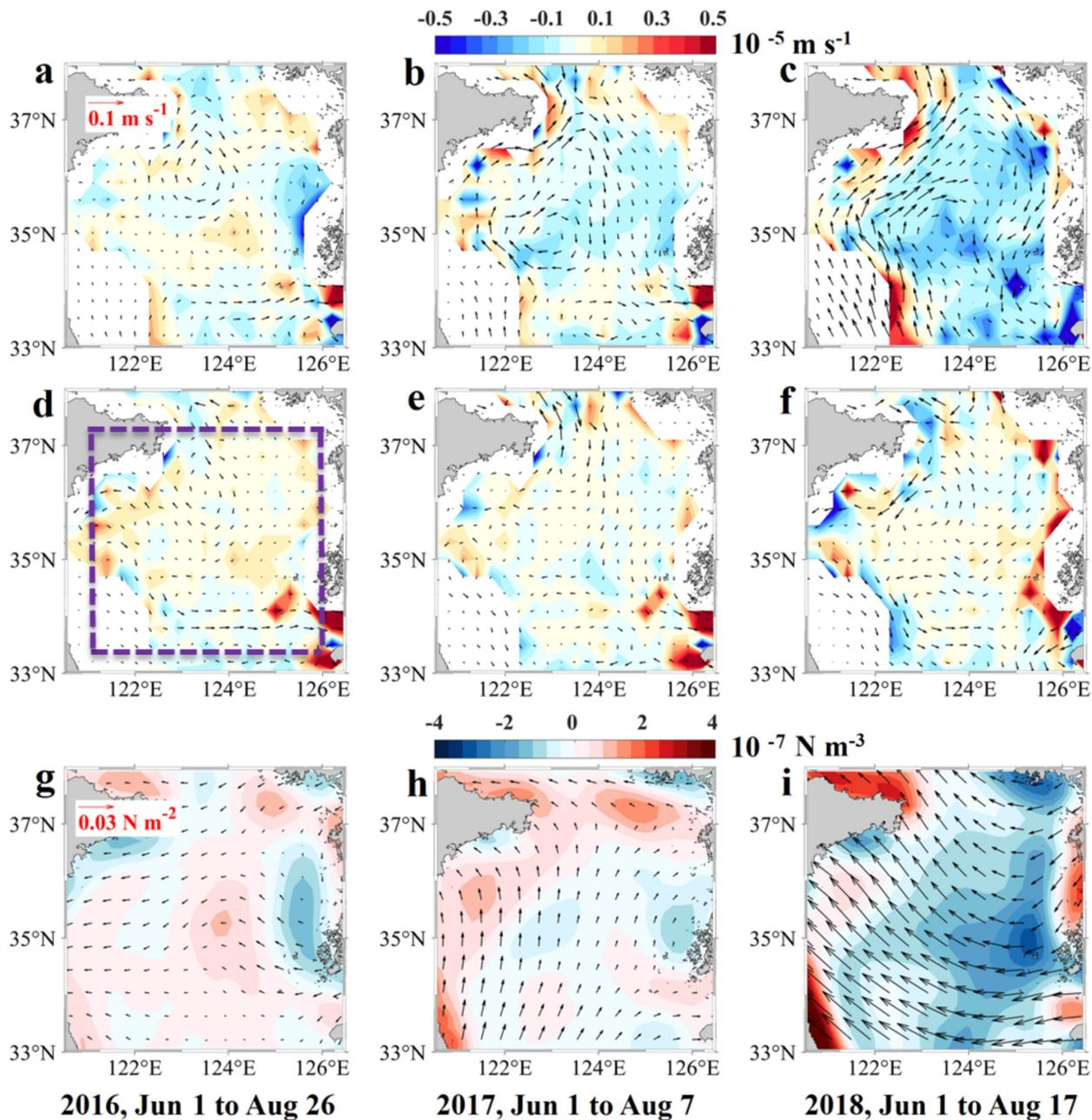
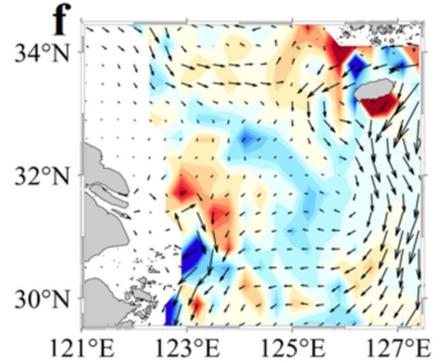
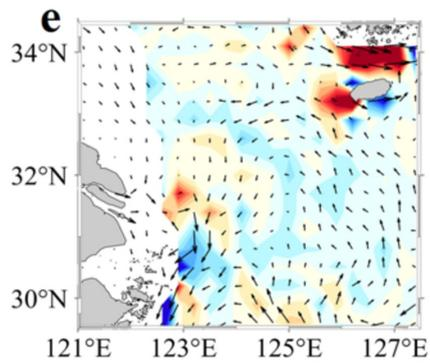
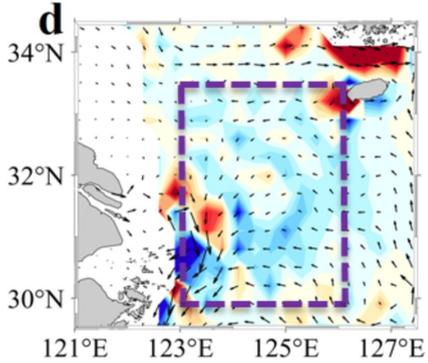
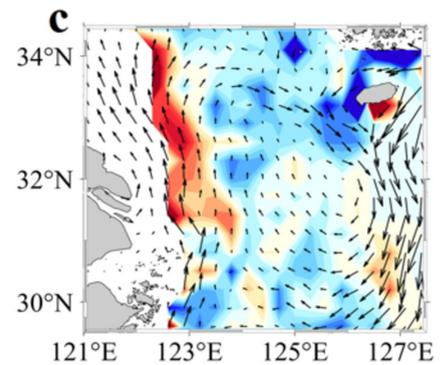
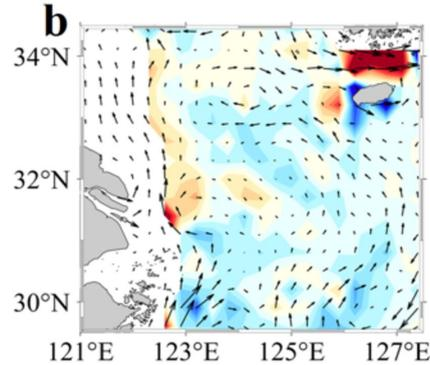
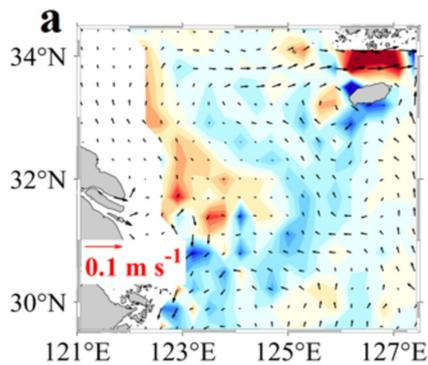


Figure 13.

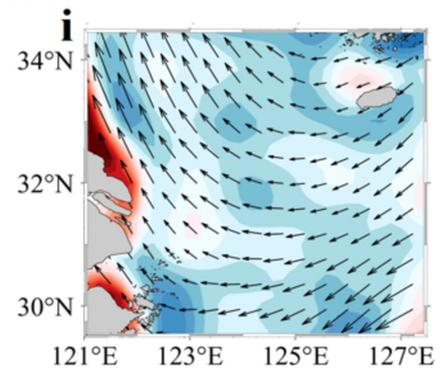
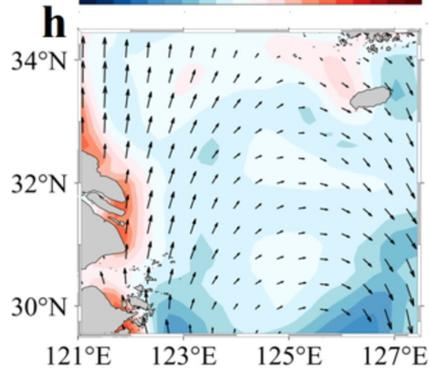
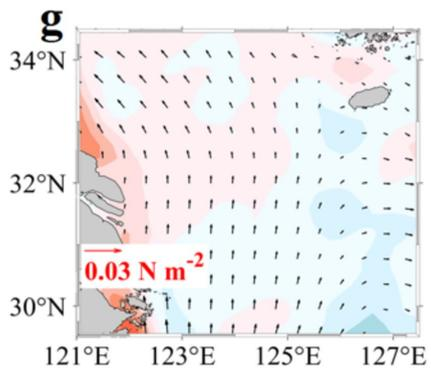
-0.5 -0.3 -0.1 0.1 0.3 0.5

$10^{-5} \text{ m s}^{-1}$



-4 -2 0 2 4

$10^{-7} \text{ N m}^{-3}$



**2016, Jun 1 to Aug 17**

**2017, Jun 1 to Aug 7**

**2018, Jun 1 to Jul 20**

Figure 14.

